UCR/DØ/94-13
E-740

UNIVERSITY OF CALIFORNIA

RIVERSIDE

Search for the Top Quark in Dimuon Events at DØ

A Dissertation submitted in partial satisfaction

of the requirements for the degree of

Doctor of Philosophy

in

Physics

by

Raymond Edward Hall

June, 1994

Dissertation Committee:

Professor Stephen J. Wimpenny, Chairperson

Professor Gordon Van Dalen

Professor Ernest Ma

AAD2302

The Dissertation of Raymond Edward Hall is approved:

Committee Chairperson

University of California, Riverside

Acknowledgments

Foremost, I thank Anne Kernan for giving me the opportunity to work in High Energy Physics and embedding me in the stimulating environment of Fermilab early in my graduate career.

I give warmest thanks to Steve Wimpenny, for sharing with me these past years his knowledge of physics, his know-how in accomplishing the daunting tasks associated with detector building and analysis, and his passion for the science of discovery.

At Riverside I thank Yvonne Ayers for her kind support and help in all matters administrative and business, and Linda O'Neill who was instrumental in recruiting me to UCR and is so supportive of all the physics graduate students.

I give thanks to all my Riverside colleagues. Especially my friends who have been with me from the start: Kamel Bazizi, who brought the DØ muon trigger on-line, Tom Fahland and Steve Jerger who were my faithful troops in the initial hardware venture, Thorsten Huehn, with whom I've shared many of the rites of passage, Brajesh Choudhary for his insights in the philosophy of analysis, and Anne Heinson, for all her warm and helpful advice.

I consider it a privilege and honor to be part of the DØ collaboration, and I thank Paul Grannis for his leadership which makes DØ such a productive and cordial environment. Appreciation goes to all members of the DØ effort, with special mention to fellow students; Joey Thompson, for many helpful discussions of the top analysis, and Jim Cochran for similar insightful deliberations and for the supervision (with help from Dave Schmid) of the processing of the Monte Carlo data files which were crucial

to the completion of this analysis. Further thanks go to the top group and its conveners, Rajendran Raja and Serban Protopopescu, for a stimulating work environment and lively meetings, and for the tremendous team work and camaraderie of all those involved, and especially that of Meena Narain and Jeff Bantly. My understanding of the detector and in particular the muon system is due to enlightening discourse with Dave Hedin, John Butler, Darien Wood and Tom Diehl. I thank them for their time and patience, and for showing me how to fix chambers and pull cables. Thanks also to Adam Para for discussions of analysis, which always lead me to better understanding of the physics involved.

For teaching me the electronics I never learned in school, I thank my very good friends Sten Hansen and Herman Haggerty, and similarly for computer literacy my appreciation goes to Paul Russo, who was instrumental in keeping the computational aspect of the analysis running smoothly.

I could not have succeeded without the loving support of my wife Heather, and my two boys Maxwell and Marshall; thank you for reminding me that physics is only one exciting aspect of my life.

Finally, I thank my parents William and Marcia, for their full support in all my dreams and endeavors, and my brother Gary and sister Sara who are always there for me.

Work supported by the U.S. Department of Energy

Contract No. DE–AM03–76SF00010

This dissertation is dedicated to my Grandfather

E. S. "Bill" Bewley

who imparted to me his sense of wonder of the universe

and zeal for cutting edge science and technology.

ABSTRACT OF THE DISSERTATION

Search for the Top Quark in Dimuon Events at DØ

by

Raymond Edward Hall

Doctor of Philosophy, Graduate Program in Physics

University of California, Riverside, June, 1994

Professor Stephen J. Wimpenny, Chairperson

I report on a search for the top quark through the decay mode $t\bar{t} \rightarrow \mu\mu + X$ in $\bar{p}p$ collisions at a center of mass energy of $\sqrt{s} = 1.8$ TeV, using the DØ detector on the Tevatron collider at the Fermi National Accelerator Laboratory. The analysis is based on 11 pb^{-1} of data collected during the 1992–93 collider run. A search was performed for top–antitop decay into two muon final states. No event candidates were observed with an expected background of 0.37 ±0.02(stat.) ±0.05(sys.) ±0.04(lum.) events.

Table of Contents

Acknowledgments v

Dedication vii

Abstract viii

Table of Contents ix

List of Figures xiii

List of Tables xvii

1 Introduction 1

1.1 Top Quark and the Standard Model 1

1.2 Status of Top Quark Searches 4

2 Theory 7

2.1 Phenomenological Considerations 7

2.2 Hadronic Production of Heavy Quarks 13

2.3 Fragmentation and Decay of Top 17

2.4 Experimental Signatures for Top at the Tevatron 19

3 Experimental Setup 23

3.1 The Tevatron 23

3.2 The DØ Detector: An Overview 24

3.3 Central Tracking and Identification 27

3.3.1 Vertex Tracking Chamber 28

3.3.2 Transition Radiation Detector 30

3.3.3 Central Tracking Chamber 32

3.3.4 Forward Tracking Chambers 35

3.4 Calorimetry 37

3.4.1 Overview: The Liquid Argon-Uranium Calorimeters 37

3.4.2 The Central Calorimeter 40

3.4.3 The End Cap Calorimeters 41

3.4.4 The Intercryostat Detectors 42

3.4.5 Calorimeter Performance 43

3.5 Muon Spectrometer 46

3.5.1 Wide Angle Muon System 48

3.5.2 Small Angle Muon System 52

3.6 Data Acquisition and Trigger 53

3.6.1 Level 0 Trigger 54

3.6.2 Level 1 and 1.5 Triggers 55

3.6.3 Level 2 Filter and Event Builder 57

4 Trigger, Event Reconstruction, and Particle Identification 59

4.1 Criteria and Method 59

4.2 Triggering 60

4.2.1 Level 1 61

4.2.2 Level 2 63

4.3 Event Reconstruction 64

4.3.1 Vertex Reconstruction 65

4.3.2 Jet Reconstruction 66

4.3.3 Muon Reconstruction 68

4.3.4 Missing Transverse Energy Measurement 73

4.4 Event Selection 75

4.4.1 Muon Selection 76

4.4.2 Jet Selection 77

4.4.3 Missing Transverse Energy Considerations 79

5 Event Simulation 81

5.1 Monte Carlo Methods 81

5.1.1 Event Generators 81

5.1.2 Detector Simulation: DØGEANT 84

5.1.3 Further Refinements 86

5.1.4 Trigger Simulator 87

5.2 Simulation of $t\bar{t} \rightarrow \mu\mu$+X Signal Events 87

5.3 Background Simulation 89

6 Final Event Selection 91

6.1 Integrated Luminosity of the Data Sample 91

6.2 Data Selection 92

6.3 Expected Number of Signal Events 107

6.4 Background to $t\bar{t} \rightarrow \mu\mu$+X 108

6.4.1 Backgrounds Involving Z^0 Decays 109

6.4.2 Heavy Quark Decays 112

6.4.3 Rare Processes 115

6.4.4 Instrumental Background 116

6.4.5 Total Background to $t\bar{t} \rightarrow \mu\mu + X$ 117

7 Conclusion 119

7.1 Top Quark Mass Limit 119

Appendix A: Cross Sections and Branching Fractions 123

References 127

List of Figures

1.1 The Standard Model prediction for $\Gamma(W)/\Gamma(W \rightarrow l\nu)$ as a function of M_t. Shown is the preliminary DØ limit [1.7] 5

2.1 A_{FB} vs. center of mass collision energy for various models, compared with seven experimental measurements 8

2.2 Examples of b quark mixing with lighter quarks that could lead to FCNC 9

2.3 Box diagrams for a) $B_d^o \overline{B}_d^o$ and b) $B_s^o \overline{B}_s^o$ mixing 10

2.4 NLO contributing diagrams for $Z^0 \rightarrow b\bar{b}$ containing top in the loops. 11

2.5 One σ error bands on $\sin^2\theta_W$ as a function of M_t assuming $M_H = M_t$. Bands correspond to LEP measurements of Z^0 mass (M_Z) and Z^0 decays(ZD). The error from M_W/M_Z measurements is shown as a vertical error bar. Solid line contains allowed region from all high energy (HE) data 12

2.6 Lowest order diagrams for $t\bar{t}$ production 14

2.7 The $t\bar{t}$ predicted cross section by Altarelli *et. al.*[2.11], based on the next to leading order calculation by Nason *et. al.*[2.10]. Figure taken from [2.15] 16

2.8 Comparison of heavy quark fragmentation functions in the Peterson model, assuming $\varepsilon_Q = 0.40/M_Q^2$ with, $M_c = 1.5$, $M_b = 4.7$, and $M_t = 40$ GeV/c^2. From reference [2.17] 17

2.9 The weak charged current decay of the top quark 18

2.10 Fraction of $t\bar{t}$ cross section into the various decay channels 20

3.1 The accelerator complex at Fermilab 24

3.2 The DØ Detector 25

3.3 Elevation of the DØ Detector 26

3.4 Layout of the central detectors 27

3.5 End view of VTX Detector 29

3.6 Cross section through the Transition Radiation Detector 31

3.7 End view of CDC Detector cells 32

3.8 Discrimination of conversion pairs in the CDC. 34

3.9 Wire orientation of a Forward Drift Chamber. 35

3.10 The DØ LAr-U Calorimeter 38

3.11 Calorimeter unit cell 39

3.12 Quadrant of Calorimeter showing radiative tower geometry 40

3.13 Calorimeter response vs. test beam momentum (top), Residuals from linearity vs. momentum of beam: electrons (bottom left) and pions (bottom right) 44

3.14 Energy deposition by cosmic ray muons in the CCFH Layer 1. Noise contributions (dark shading) deduced from signals observed far from cosmic ray track. Data is ploted with a 3-σ suppression 45

3.15 Expanded view of the DØ muon system 46

3.16 DØ muon system: absorption lengths (λ) vs. angle from the beam (θ) 47

3.17 Cross sections of: (a) WAMUS muon chamber assembly (3 deck shown), and (b) WAMUS cell showing anode wire and cathode pads with assocoated equipotential lines 49

3.18 Cathode pad strip and associated charge ratio vs. distance plot 50

3.19 Exploded view of the DØ Muon system 51

3.20 Muon Level 1 acceptance and efficiency vs. muon p_T for the CF region. Geometrical acceptance (solid line), geometrical acceptance + efficiency (dashed line) 56

4.1 Jet trigger efficiency vs. jet E_T for a 5 GeV trigger tower threshold 61

4.2 Highest E_T jet in ISAJET $t\bar{t} \rightarrow \mu\mu$ for top masses of: **(a)** 140, **(b)** 120 and **(c)** 100 GeV/c^2. Arrows indicate threshold set in Level 2. Note that the

Level 1 trigger is only fully efficient for jets with E_T above 30 GeV (Fig. 4.1) 62

4.3 Highest p_T muon in ISAJET $t\bar{t} \rightarrow \mu\mu$ for top masses of: **(a)** 140, **(b)** 120 and **(c)** 100 GeV/c^2. Arrows indicate threshold set in Level 2. Note that the Level 1 muon trigger has an acceptance of roughly 65% for p_T above 8 GeV/c (see Fig 3.20) 64

4.4 Comparison of tuned Monte Carlo (dashed line) to muon data (points) 71

4.5 Comparison of tuned Monte Carlo (dashed line) to muon data (points) for **(a)** muon transverse momentum and **(b)** pseudorapidity for $W \rightarrow \mu\nu$ 72

4.6 Resolution of $\not{E}_T^{cal}$ as a function of sum scalar E_T 75

4.7 Jet energy correction factor for ΔR=0.7 cone jets at $|\eta|$=0.0 and $|\eta|$=2.5. Dashed curves show the upper and lower response from test beam and Monte Carlo calibrations 78

6.1 ISAJET QCD production of $b\bar{b}$ and $c\bar{c} \rightarrow \mu\mu$. **(a)** lego plot of $p_T^{\mu_1}$ vs. $p_T^{\mu_2}$, **(b)** $p_T^{\mu_1}$, **(c)** $p_T^{\mu_2}$ after cut: $p_T^{\mu_1}$>15 GeV/c, **(d)** scatter plot of $p_T^{\mu_1}$ vs. $p_T^{\mu_2}$. Hatched lines show regions excluded by the muon p_T cuts 96

6.2 ISAJET $t\bar{t} \rightarrow \mu\mu$ (M_t=140 GeV/c^2). **(a)** lego plot of $p_T^{\mu_1}$ vs. $p_T^{\mu_2}$, **(b)** $p_T^{\mu_1}$, **(c)** $p_T^{\mu_2}$ after cut: $p_T^{\mu_1}$>15 GeV/c, **(d)** scatter plot of $p_T^{\mu_1}$ vs. $p_T^{\mu_2}$. Arrows indicate placement of muon p_T cuts 97

6.3 Invariant mass of dimuon pair. Data events remaining after initial cuts 98

6.4 p_T^{rel} for single muon plus jet sample (circles with error bars) as compared to full detector Monte Carlo (solid line) which is the sum of the contributions from b quark decays (dotted line) and c quark decays (dashed line) [6.5] 99

6.5 p_T^{rel} for single muon (p_T^{μ} > 10 GeV/c) plus jet sample, arrow indicates cut made in the analysis 100

6.6 $\Delta\phi$ vs. $\Delta\eta$ between muon pair tracks for **(a)** Cosmic ray events and **(b)** $t\bar{t} \rightarrow \mu\mu$ Monte Carlo (M_t=160 GeV/c^2). Solid line indicates excluded region 101

6.7 Opening angle between leading muon p_T and muon corrected $\not{E}_T$ for: **(a)** two layer tracks and **(b)** three layer tracks, on Monte Carlo samples of: **(1)** $Z^0 \rightarrow \mu\mu$, where hatched lines mark regions excluded and **(2-4)** $t\bar{t} \rightarrow \mu\mu$ (M_t=160, 140, and 120 GeV/c^2), with arrows indicating placement of cut 102

6.8 Opening angle ($\Delta\phi$) cut on the dimuon p_T vector and the $\not{E}_T^{cal}$ vector for: **(a)** $Z^0 \rightarrow \mu\mu$ Monte Carlo and **(b-d)** $t\bar{t}$ Monte Carlo (M_t=160,140, and 120 GeV/c^2). The cut is placed at 30°, shown by the hatched line for the background and arrows for the signal 104

6.9 Opening angle in ϕ between the p_T vectors of the muon pair vs. the muon corrected missing transverse energy for: **(a)** $Z^0 \rightarrow \mu\mu$ Monte Carlo and **(b-d)** $t\bar{t}$ Monte Carlo (M_t=160, 140, and 120 GeV/c^2) 106

6.10 Definition of p_T^{rel} 114

7.1 The 95% CL limit on $t\bar{t}$ production cross section obtained by DØ using the combined analyses of $e\mu$, ee, e + jets, and μ + jets decay channels.The theory curve (dashed line) is the lower bound from Laenen *et.al.*[7.4] 121

List of Tables

1.1 Fundamental constituents of the Standard Model 2

1.2 The three quark and lepton generations 3

2.1 Decay modes of W^+W^-. Decays to quark states give $(u\bar{d}, c\bar{s}) \times 3$ colors = 6 final states for each W 19

3.1 Vertex Chamber Parameters 29

3.2 Central Drift Chamber Parameters 34

3.3 Forward Drift Chamber Parameters 36

3.4 Central Calorimeter Parameters 41

3.5 End Calorimeter Parameters 42

3.6 Muon system parameters 52

4.1 Level 1 and Level 2 triggers for $t\bar{t} \rightarrow \mu\mu + X$ 60

5.1 Principal signal Monte Carlo event samples 88

5.2 Principle background Monte Carlo event samples 89

6.1 Final analysis cuts and cumulative effect on data 93

6.2 $t\bar{t} \rightarrow \mu\mu$ efficiency (errors: stat,sys) and expected event yield (errors: stat,sys,lum) 107

6.3 Comparison of the cumulative effect of the final analysis cuts on data versus $Z^0 \rightarrow \mu\mu$ full detector simulation Monte Carlo events 110

6.4 Backgrounds to $t\bar{t} \rightarrow \mu\mu$+X; event yields for 11.0 pb^{-1} 117

A.1 Branching Fractions 123

A.2 Total Cross Sections 124

A.3 Relevant Cross Sections 125

CHAPTER 1
INTRODUCTION

1.1 Top Quark and the Standard Model

The *Standard Model* is the modern theory of particle physics which describes the fundamental constituents of matter and their interactions. This theory attempts to explain all the phenomena of particle physics in terms of the properties and interactions of a small number of particles of three distinct types (Table 1.1). The first two types are *leptons* and *quarks*, which are spin $\frac{1}{2}$ fermions. The third is a set of spin 1 *gauge bosons* which act as the force carriers in the theory. In the Standard Model these particles are assumed to be elementary (*i.e.,* treated as point particles, without internal structure or excited states), and are classified in terms of the fundamental forces through which they couple. Quarks couple to the fundamental forces of the strong interaction, the weak interaction, and electromagnetism (the gravitational interaction of elementary particles is negligible in comparison with the other three and is not included in the theory). Leptons, on the other hand, behave differently in that they do not couple to the strong interaction.

The fermions are grouped into three generations of quarks and leptons (Table 1.2). The existence of a fourth generation is in principle also possible. However, experiments at e^+e^- colliders (LEP and SLC) have ruled out the existence of a fourth light neutrino, implying that a fourth generation is only allowed if its neutrino has a mass in excess of 30 GeV/c^2 [1.1].

		Charge (e)	Mass (MeV/c^2)	Discovery
Quarks (spin $\frac{1}{2}$)	d	$-\frac{1}{3}$	~ 350	~ 1932
	u	$+\frac{2}{3}$	~ 350	~ 1932
	s	$-\frac{1}{3}$	~ 550	1948–50
	c	$+\frac{2}{3}$	~ 1800	1974
	b	$-\frac{1}{3}$	~ 4500	1977
	t	$+\frac{2}{3}$	> 131,000	?
Leptons (spin $\frac{1}{2}$)	e	-1	0.511	~ 1900
	ν_e	0	$< 7.3\times10^{-6}$	~ 1957
	μ	-1	105.7	1938–40
	ν_μ	0	< 0.27	~ 1962
	τ	-1	1784	1975
	ν_τ	0	< 35	1975–78
Gauge Bosons (spin 1)	gluons	0	0	1970's
	γ	0	0	~ 1905
	$W^\pm$	±1	80,220	1983
	Z^0	0	91,173	1983
Higgs Boson (spin 0)	H^0	0	> 58,000	?

Table 1.1 Fundamental constituents of the Standard Model, from Ref. [1.2], [1.3] , and [1.5].

There is good experimental evidence for the existence of five quark flavors (u, d, c, s and b), but to date there is no direct experimental evidence for the postulated sixth quark, t (top). However, there are strong theoretical reasons for expecting it to exist. One such argument is based on the chiral nature of the theory, which states that intractable divergences occur when the left and right fermion couplings are unequal at one (or three) of the vertices, unless the contribution from each fermion exactly cancels to make the theory anomaly free. Cancellation of this chiral anomaly requires that the fermion charges allow contributions from each generation to cancel among themselves;

	GENERATION I	II	III
QUARKS	u up	c charm	t top
	d down	s strange	b bottom
LEPTONS	e electron	μ muon	τ tau
	ν_e electron neutrino	ν_μ muon neutrino	ν_τ tau neutrino

Table 1.2 The three quark and lepton generations

which in turn calls for three colors of quark and demands the existence of top to complete the cancellation in the third generation.

The existence of top is supported by both indirect experimental evidence and tests of theory through precision measurements of Standard Model parameters. The Standard Model is based on the symmetry SU(3)⊗SU(2)⊗U(1); and the leptons and quarks are paired into the weak SU(2) doublets, each representing a two component field. The conserved quantum number is *weak isospin*, T_L, and the fermions in the doublet will have values for the third component of $T_{3L} = (+\frac{1}{2}, -\frac{1}{2})$. There is much evidence (see Sec. 2.1) that the b quark has $T_{3L}^b = -\frac{1}{2}$, consistent with being in an SU(2) doublet, and thus in need of a partner.

The top quark has been the subject of intense searches since the discovery of the bottom quark in 1977 [1.4]. The next section outlines current limits on the top quark mass from the most recent of these searches.

1.2 Status of Top Quark Searches

The highest published experimental limit on the top quark mass is

$$M_t > 131 \text{GeV/c}^2 \text{ at } 95\ \%\ \text{CL}$$

from the 16.7 pb^{-1} of data taken by the DØ Collaboration during the 1992–1993 Tevatron collider run [1.5]. This limit comes from the combined results of searches for $t\bar{t}$ decaying through the dilepton channels of $e\mu$ and ee, and searches for decays in the lepton + jets modes of μ + jets and e + jets.

Model independent lower limits on M_t come from LEP and SLC, where the non-observation of the decay mode $Z^0 \to t\bar{t}$ gives a lower limit of 45.8 GeV/c^2 [1.6]. Direct searches at e^+e^- colliders are limited in their reach by their collision energy (*i.e.*, to see top, M_t would need to be $\leq \sqrt{s}/2$, where the present maximum $\sqrt{s}$ is ~ 94 GeV).

An additional indirect constraint comes from measurements of the ratio

$$R = \frac{\sigma_W \cdot \text{BR}(W \to l\nu)}{\sigma_{Z^0} \cdot \text{BR}(Z^0 \to ll)}$$

where

$$\frac{\text{BR}(W \to l\nu)}{\text{BR}(Z^0 \to ll)} = \left(\frac{\Gamma(W \to l\nu)}{\Gamma_W^{tot}}\right) \Big/ \left(\frac{\Gamma(Z^0 \to ll)}{\Gamma_{Z^0}^{tot}}\right).$$

By taking the ratio, some theoretical uncertainties (structure functions, mass scale) and experimental uncertainties (luminosity, resolution effects) will cancel. By measuring this ratio, and using the Standard Model to calculate the branching fractions for Z^0's to lepton pairs and W's to lepton plus neutrino states, one can solve for the ratio of the total widths of the W and Z^0. These total widths in turn depend on whether the top quark is light enough to open the $t\bar{t}$ decay channel of the Z^0, or the $t\bar{b}$ decay channel of the W.

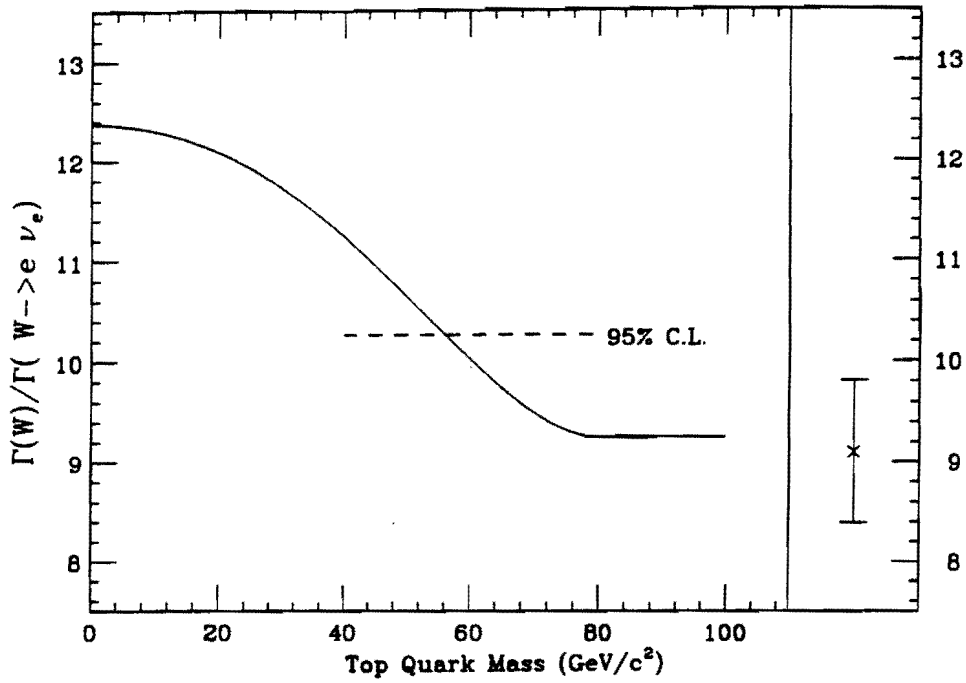

Figure 1.1 The Standard Model prediction for $\Gamma(W)/\Gamma(W \rightarrow l\nu)$ as a function of M_t. Shown is the preliminary DØ limit [1.7].

For example, by using the total width for the Z^0 measured at LEP and preliminary measurements of Γ_W by DØ, one can obtain a lower limit of 56 GeV/c^2 at 95% CL on M_t(Figure 1.1)[1.7]. Lower limits on M_t using this technique are constrained by the value of the W mass, and are only sensitive to a top quark mass in the range $M_t \leq M_W$.

CHAPTER 2
THEORY

2.1 Phenomenological Considerations

The Standard Model (SM) displays SU(3)⊗SU(2)⊗U(1) symmetry and its primary objects can be categorized by their grouping into the weak SU(2) states. Gluons and right handed fermions are in SU(2) singlets, and left handed fermions are in SU(2) doublets. The W^+, W^-, and W^0 are grouped in an SU(2) triplet and B^0 is in a singlet state, where the W^0 and B^0 mix to give the familiar γ and Z^0.

Since its discovery in 1977, various experimental measurements have been made which show that the properties of the b quark are consistent with it being in an SU(2) doublet state. The partner to the b quark is by definition the top quark, which so far has eluded experimental discovery. The structure of the Standard Model imposes several constraints on top quark properties (such as charge, spin, etc.), and precise experimental measurements of SM parameters can be used to place limits on the range of possible mass values.

The following sections give an overview of the evidence for the existence of the top quark and what can currently be said about its mass assuming the structure of the SM.

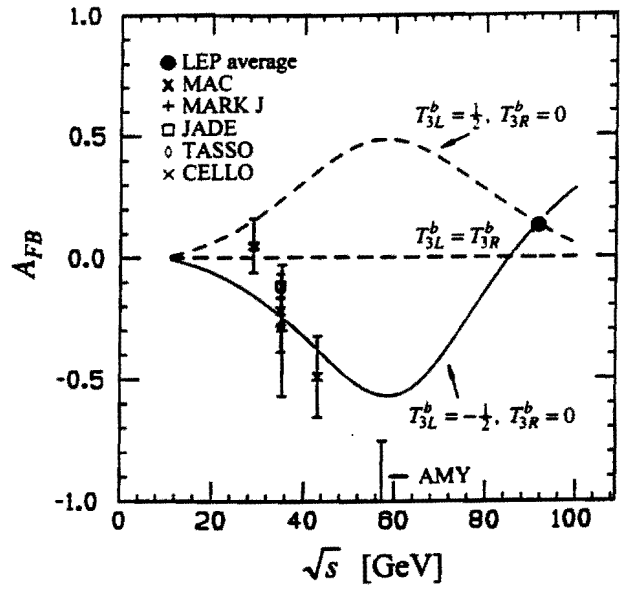

Figure 2.1 A_{FB} vs. center of mass collision energy for various models, compared with seven experimental measurements.

Forward-Backward Asymmetry in $e^+e^- \to b\bar{b}$

Due to the interference between the γ and Z^0 contributions to the process $e^+e^- \to b\bar{b}$, there is a non-zero energy dependent forward-backward asymmetry A_{FB} in the $b\bar{b}$ production cross section. Experimentally this is defined as $A_{FB} = (N_b^F - N_b^B)/(N_b^F + N_b^B)$ where $N_b^F(N_b^B)$ is the number of b quark jets in the forward(backward) direction. The interference arises because of an asymmetry in the b quark coupling to the Z^0 and γ; the b quark has vector coupling to photons, whereas, it has both vector and axial-vector coupling to the Z^0. A_{FB} is thus related to the weak isospin eigenvalues (T_{3R}^b and T_{3L}^b) through a complicated expression [2.1] which is dependent on collision energy. Figure 2.1 shows a compilation of measurements of A_{FB}

at various collision energies, compared to theory for different values of T_{3R}^b and T_{3L}^b. Note that only the SM choices of $T_{3R}^b = 0$ and $T_{3L}^b = -\frac{1}{2}$ are consistent with the data.

A more precise determination of T_{3R}^b and T_{3L}^b can be made using the measured partial decay width of the Z^0 into $b\bar{b}$ pairs, $\Gamma(Z^0 \to b\bar{b})$, which is proportional to

$$\left(T_{3L}^b + \tfrac{1}{3}\sin^2\theta_W\right)^2 + \left(T_{3R}^b + \tfrac{1}{3}\sin^2\theta_W\right)^2$$

apart from some small corrections. Using measurements of A_{FB} corrected for $B^0 - \bar{B}^0$ mixing, the equations for A_{FB} and $\Gamma(Z^0 \to b\bar{b})$ are solved for the weak isospin eigenvalues yielding [2.1]

$$T_{3L}^b = -0.491^{+0.044}_{-0.022}$$
$$T_{3R}^b = -0.003^{+0.104}_{-0.060}\ .$$

This reveals how well these values are measured and how close they are to the expected SM values of $T_{3R}^b = 0$ and $T_{3L}^b = -\frac{1}{2}$, implying that the bottom quark is indeed in an SU(2) doublet.

Absence of Flavor Changing Neutral Currents in b Quark Decays

Using an argument similar to that of the GIM mechanism [2.2], third generation quark models with a b quark and no t quark should lead to Flavor Changing Neutral Currents (FCNC) in b decays. In simple terms, if the b quark were in an SU(2) singlet it would not have charged current interactions and thus could not decay by W emission. Since it does decay in this manner, some kind of mixing with the lighter quarks must be

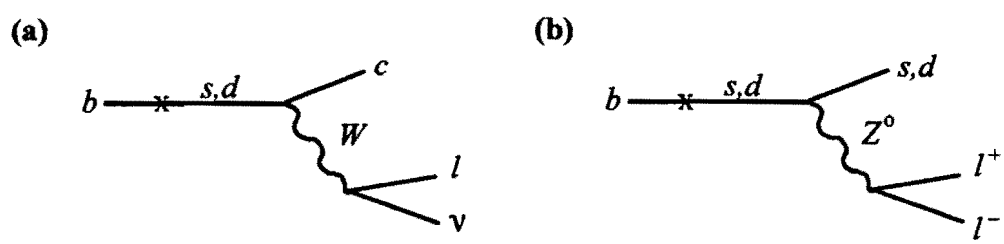

Figure 2.2 Examples of b quark mixing with lighter quarks that could lead to FCNC.

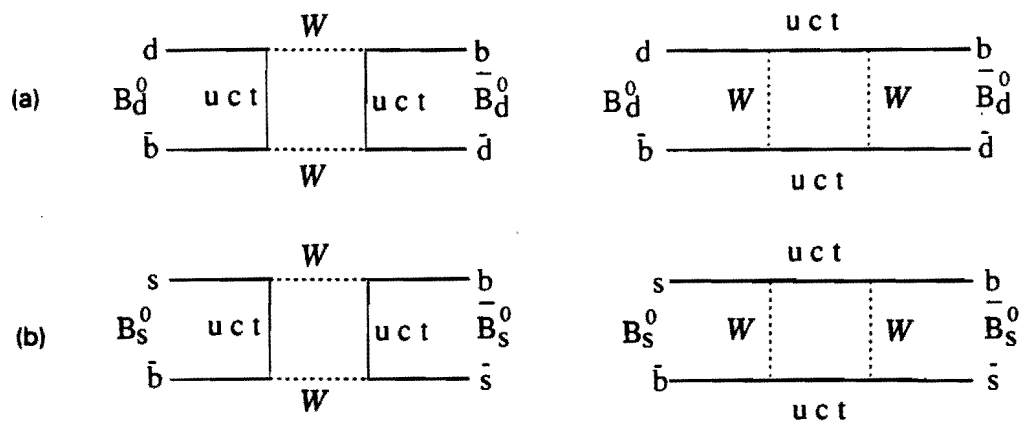

Figure 2.3 Box diagrams for a) $B_d^o\overline{B}_d^o$ and b) $B_s^o\overline{B}_s^o$ mixing.

involved (*e.g.*, Fig. 2.2a). If the process in Fig. 2.2a is valid, so must processes like that in Fig. 2.2b. Kane and Peskin [2.3] have shown that if the b quark is indeed in an SU(2) singlet, then the ratio of diagrams like Fig. 2.2a to those like Fig. 2.2b gives a quantitative prediction of

$$\mathrm{BF}(b \to l^+l^-X) > 0.013 .$$

Currently, experimental limits set this branching ratio at less than 0.0005 [2.4], which establishes that b is not in an SU(2) singlet state, and thus needs a partner.

$B^0 - \overline{B}^0$ *Mixing*

Through mixing, a B^0 meson can transform into its antiparticle, the $\overline{B}^0$, before decaying. The second quark in the neutral B meson can be a d quark ($B_d^0 = \bar{b}d$) or an s quark ($B_s^0 = \bar{b}s$). $B_d^0 - \overline{B}_d^0$ and $B_s^0 - \overline{B}_s^0$ mixing proceeds through box diagrams like those in Fig. 2.3, with mixing given by

$$x = \frac{\Delta M_{B_d^0(B_s^0)}}{\Gamma} \sim \left|V_{td(s)}V_{tb}^*\right|^2 \frac{M_t^2}{M_W^2}$$

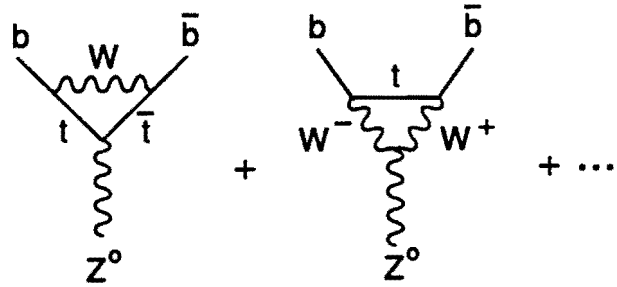

Figure 2.4 NLO contributing diagrams for $Z^0 \to b\bar{b}$ containing top in the loops.

and thus goes as a function of the CKM elements $|V_{td}|^2$ or $|V_{ts}|^2$ and M_t^2. $B^0\overline{B}^0$ pairs can be produced in e^+e^- and $\bar{p}p$ collisions, and the signature for mixing is an excess of same sign dilepton events, from the semileptonic decays of both B mesons of a B^0B^0 or $\overline{B}^0\overline{B}^0$ final state. The amount of mixing seen (*e.g.*, UA1[2.5] and ARGUS[2.6]) is more than can be explained in the minimal SM without including a heavy top quark. However, this constraint on the top mass is model dependent; other non-SM states could be responsible for the observed $B^0 - \overline{B}^0$ mixing.

Top Mass Limits from Radiative Corrections

The mass of the top quark has measurable effects, through radiative corrections, on many SM processes. For example, the ratio of Z^0 partial decay width into $b\bar{b}$ to that of all hadronic decays ($\Gamma_{bb}/\Gamma_{had} \equiv \mathrm{R}_b$) is especially sensitive to the top mass through diagrams like those shown in Fig. 2.4. Here the vertices are unsuppressed by CKM factors and R_b is reduced as compared to R_d by the contribution of $W^{\pm}$ as given by the expression [2.1]:

$$\mathrm{R}_b \cong \mathrm{R}_d\left[1-\frac{20\alpha}{13\pi}\left(\frac{M_t^2}{M_Z^2}+\frac{13}{6}\ln\frac{M_t^2}{M_Z^2}\right)\right].$$

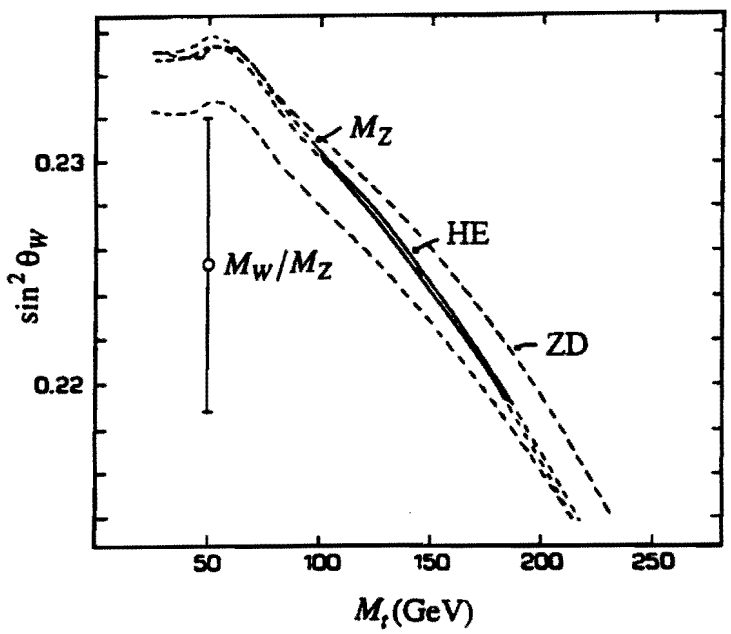

Figure 2.5 One σ error bands on $\sin^2\theta_W$ as a function of M_t assuming $M_H = M_t$. Bands correspond to LEP measurements of Z^0 mass (M_Z) and Z^0 decays(ZD). The uncertainty from M_W/M_Z measurements is shown as a vertical error bar. Solid line contains the allowed region from all high energy (HE) data.

The current world average value for R_b is 0.2203 ± 0.0027 (*i.e.*, errors of ±1.2%), which includes measurements from the four LEP experiments and SLD [2.7]. This sets an upper limit, $M_t < 210$ GeV/c^2 at 95% CL, from the χ^2 for the SM fit to R_b alone.

Many parameters in the SM have some dependence on the top mass, such as the mass of the W and Z^0 bosons, the Wienberg angle ($\sin^2\theta_W$), and as cited above, the partial decay widths of the Z^0. The effects on W mass and $\sin^2\theta_W$ can be measured through the radiative corrections to the vector boson masses. In the SM, these can be expressed as [2.8]

$$M_W^2 = \frac{\pi\alpha}{\sqrt{2}G_\mu}\frac{1}{(1-\Delta r)\sin^2\theta_W}$$

where the weak mixing angle θ_W is defined by

$$\sin^2\theta_W \equiv 1-\left(M_W/M_Z\right)^2$$

and α and G_μ are the fine structure constant and muon decay constant, respectively. The radiative corrections denoted by Δr vary with top mass, and to a lesser extent with Higgs mass M_H. Using these relationships together with current measurements, Fig. 2.5 illustrates the constraints placed on the $\sin^2\theta_W$ as a function of top mass.

By performing global fits to the experimental data on each of these parameters, it is possible to extract predictions for the allowable range and most likely value of the top quark mass, M_t. For example a recent analysis [2.9] of data from LEP combined with measurements of M_W and M_W/M_Z from CDF and UA2 and $\sin^2\theta_W$ from the neutrino experiments CDHS, CHARM, and CCFR yields a predicted top mass of

$$M_t = 164\,^{+16}_{-17}\,^{+18}_{-21}\ \mathrm{GeV/c^2}$$

for an assumed Higgs mass of 300 GeV/c^2. The first error quoted is due to experimental and theoretical uncertainties for a fixed Higgs mass of 300 GeV/c^2; the second uncertainty arises from a variation of the Higgs mass in the range $60 < M_H < 1000$ GeV/c^2.

2.2 Hadronic Production of Heavy Quarks

In principle there are two ways of producing top quarks at a high energy $\bar{p}p$ collider: $p\bar{p} \rightarrow W \rightarrow t\bar{b}$ and $p\bar{p} \rightarrow t\bar{t}$. The first process has significant production cross section only if $M_t < M_W - M_b$; for top masses above this critical value the process must proceed through a virtual W and the cross section falls rapidly. The second process, that of top pair production, is the dominant production mechanism for all

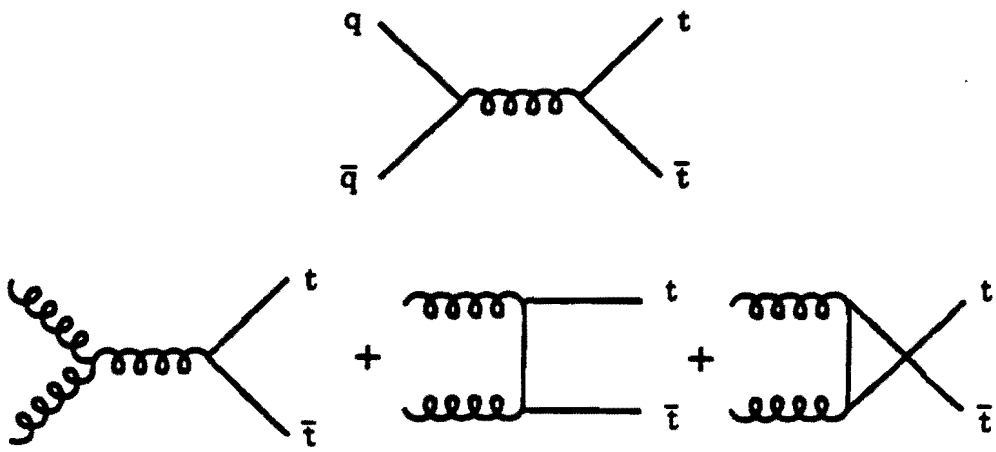

Figure 2.6 Lowest order diagrams for $t\bar{t}$ production.

values of M_t at the Tevatron's 1.8 TeV center of mass collision energy and is the focus of the analysis presented in this thesis.

In the QCD parton model, the scattering cross section of two hadrons into a pair of heavy quarks ($A+B \rightarrow Q+\overline{Q}+X$) is given by

$$\sigma(s) = \sum_{ij} \int dx_1 dx_2 \sigma_{ij}(x_1 x_2 s, m^2, \mu^2) F_i^A(x_1, \mu) F_i^B(x_2, \mu),$$

where the structure functions F_i^A are the probabilities of finding a parton i in a hadron A with momentum fraction between x_1 and $x_1 + dx_1$, m is the heavy quark mass and $\sqrt{s}$ is the center of mass energy of the $A + B$ system. μ is a scale factor related to the energy scale of the interaction. The partonic cross sections σ_{ij} for the process $ij \rightarrow Q\overline{Q}X$ are calculable as an expansion of the strong coupling constant α_s [2.10]. The lowest order diagrams (α_s^2) shown in Fig. 2.6 are the processes of gluon-gluon fusion and quark-antiquark annihilation:

$$g+g \rightarrow Q+\overline{Q}$$
$$q+\overline{q} \rightarrow Q+\overline{Q}$$

Higher order processes make significant contributions to the top production cross section via $g \rightarrow Q\overline{Q}$ in the process $gg \rightarrow gg$. Even though gluon splitting occurs a small fraction of the time ($\sim \alpha_s(M^2)$), the large cross section of $gg \rightarrow gg$ makes these processes important in calculating top production. Nason, Dawson, and Ellis [2.5] have estimated heavy quark cross sections based on exact calculation of the first order QCD (α_s^2) processes and higher order perturbative QCD (α_s^3) processes. The parton subprocesses included are summarized as follows:

$q+\overline{q} \rightarrow Q+\overline{Q}$	α_s^2, α_s^3
$g+g \rightarrow Q+\overline{Q}$	α_s^2, α_s^3
$q+\overline{q} \rightarrow Q+\overline{Q}+g$	α_s^3
$g+g \rightarrow Q+\overline{Q}+g$	α_s^3
$g+q \rightarrow Q+\overline{Q}+q$	α_s^3
$g+\overline{q} \rightarrow Q+\overline{Q}+\overline{q}$	α_s^3

Theoretical heavy flavor cross sections are dependent on many input quantities: parton structure functions, choice of renormalization and factorization scale μ, the choice of running coupling constant α_s (or equivalently, the choice of the QCD scale parameter Λ), and the mass of the heavy quark. Altarelli *et. al.*, [2.11] have studied the total cross sections of top, bottom and charm production using the results of Nason *et. al.* together with the set of structure functions by DFLM [2.12] (also obtained with next to leading order accuracy). Their result of top cross section for $\overline{p}p$ collisions at $\sqrt{s}$ = 1.8 TeV is shown vs. top mass in Fig 2.7.

A further refinement to the theoretical cross section of top production has recently been calculated by Laenen, Smith and van Neerven. Typically the mass scale

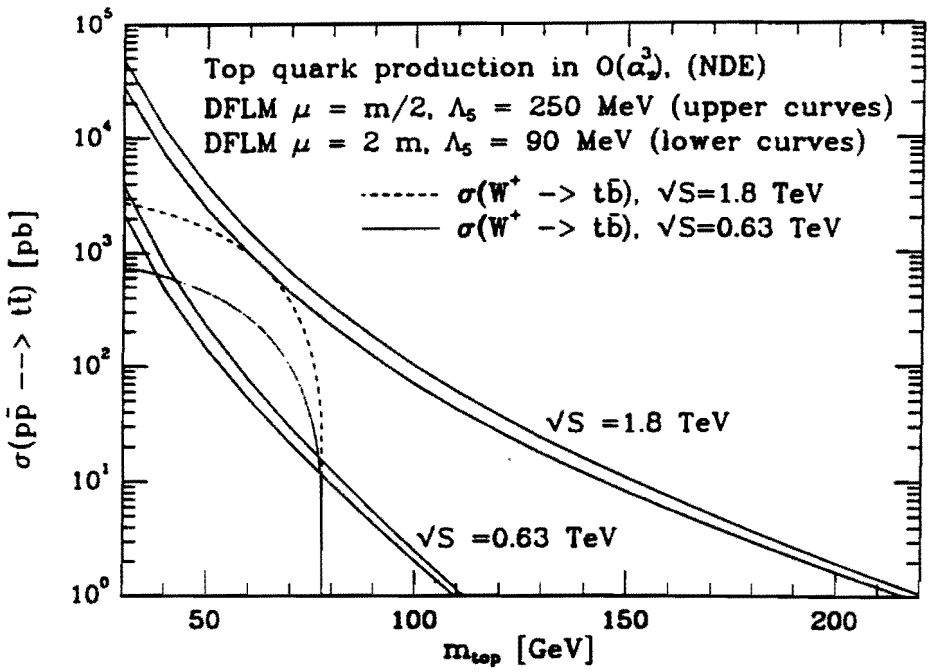

Figure 2.7 The $t\bar{t}$ predicted cross section by Altarelli *et. al.*[2.11], based on the next to leading order calculation by Nason *et. al.*[2.10]. Figure taken from [2.15].

parameter Λ is determined by varying the renormalization scale μ for the α_s^2 plus α_s^3 cross sections. Laenen *et. al.* developed a technique whereby this scale factor is determined from a resummation of the leading soft gluon corrections to all orders of perturbation theory [2.13]. Their most recent calculations, building on the NLO results of Nason *et. al.*, use the MRS D–′ set of structure functions [2.14] and the two-loop running coupling constant with five active flavors. Their results, together with those of Nason *et. al.* are tabulated in Appendix A.

2.3 Fragmentation and Decay of Top

After a heavy quark is produced, it undergoes fragmentation as it combines or *hadronizes* into a hadron containing its flavor, and into some softer hadrons of lighter quarks. The process of fragmentation of heavy quarks can be modeled by the Peterson *et. al.* parametrization [2.16], which defines a fragmentation function $D_Q^H(z)$ to describe the probability that the fraction of the quark (Q) momentum carried away by the resulting hadron (H) lies between z and $z + dz$:

$$D_Q^H(z) = \frac{C}{z\left[1-(1/z)-\varepsilon_Q/(1-z)\right]^2}$$

where $z = P_H/P_Q$, C is a normalization constant, and the *Peterson parameter* ε_Q is proportional to $1/M_Q^2$. This parametrization adequately describes existing c and b quark fragmentation data [2.17]. Note that for higher quark masses, significantly more of the initial quark momentum is transferred to the hadron (see Fig. 2.8).

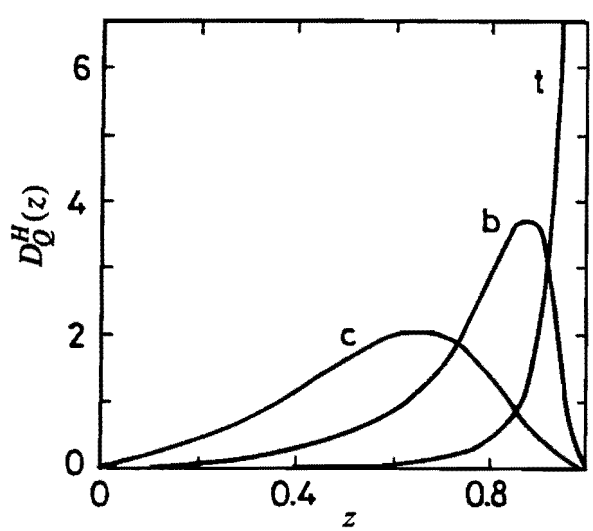

Figure 2.8 Comparison of heavy quark fragmentation functions in the Peterson model, assuming $\varepsilon_Q = 0.40/M_Q^2$ with, $M_c = 1.5$, $M_b = 4.7$, and $M_t = 40$ GeV/c^2. From reference [2.17].

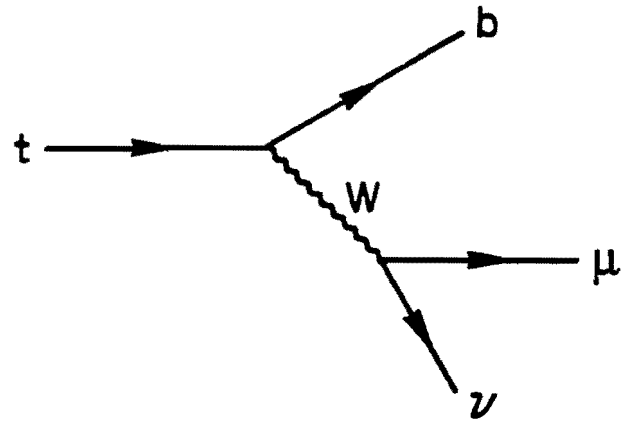

Figure 2.9 The weak charged current decay of the top quark.

The width of the top quark scales with mass as $\Gamma \sim 0.17\ \mathrm{GeV}(M_t/M_W)^3$ [2.18], where the lifetime $\tau = 1/\Gamma$. Thus if the top quark mass becomes very heavy, the width becomes large, resulting in a lifetime too short for the top quark to hadronize before it decays. Furthermore, above a certain mass threshold, there is insufficient time for formation of any top quark bound states. Thus, since the top quark is so heavy ($> 91\ \mathrm{GeV}/c^2$), the portion of the initial quark momentum carried off by fragmentation products other than that containing the top quark is very small if any.

The only Standard Model top decay mechanisms are [2.1]:

$$t \rightarrow W + d \qquad \Gamma_d \sim |V_{td}|^2 \sim 10^{-4}$$
$$t \rightarrow W + s \qquad \Gamma_s \sim |V_{ts}|^2 \sim |V_{bu}|^2 \sim 0.0025$$
$$t \rightarrow W + b \qquad \Gamma_b \sim |V_{tb}|^2 \sim 1$$

where the branching fractions are listed for comparison. Consequently the dominant decay of the top is to a b quark and a real W via the diagram in Fig. 2.9. This forms the basis of all current search strategies used at DØ.

2.4 Experimental Signatures for Top at the Tevatron

At the Tevatron's center of mass collision energy of $\sqrt{s}$=1.8 TeV the dominant production mechanism of top quarks is that of $t\bar{t}$ pairs. Each top will then decay via a real W and a b quark, so the final state includes the decay products of two W's and two b quarks. The topology of a $t\bar{t}$ event is largely determined by how the pair of W's decay. W bosons decay to the three lepton generations and two families of quarks of three colors, with roughly equal probability for a total of 9 final states. Neglecting mass effects, which make small corrections to the rates of c quarks and τ leptons, the branching fraction for each mode is thus $\frac{1}{9}$. The branching fractions for the possible decay products of a W^+ and a W^- pair are given in Table 2.1.

The largest branching fractions of top is to all jets (44.4 %) and to decays involving a τ lepton (21.0 %). In spite of the large branching fractions, these channels

W^+ / W^-	$(\frac{1}{9})$ $e^+\nu_e$	$(\frac{1}{9})$ $\mu^+\nu_\mu$	$(\frac{1}{9})$ $\tau^+\nu_\tau$	$(\frac{6}{9})$ jets
$(\frac{1}{9})$ $e^-\bar{\nu}_e$	$\frac{1}{81}$	$\frac{1}{81}$	$\frac{1}{81}$	$\frac{6}{81}$
$(\frac{1}{9})$ $\mu^-\bar{\nu}_\mu$	$\frac{1}{81}$	$\frac{1}{81}$	$\frac{1}{81}$	$\frac{6}{81}$
$(\frac{1}{9})$ $\tau^-\bar{\nu}_\tau$	$\frac{1}{81}$	$\frac{1}{81}$	$\frac{1}{81}$	$\frac{6}{81}$
$(\frac{6}{9})$ jets	$\frac{6}{81}$	$\frac{6}{81}$	$\frac{6}{81}$	$\frac{36}{81}$

Table 2.1 Decay modes of W^+W^-.
Decays to quark states give $(u\bar{d}, c\bar{s})$ ×3 colors
= 6 final states for each W.

are experimentally very difficult to study because of large background processes (QCD multijet events) and the difficulty of reconstructing τ decays. Next are the lepton + jets modes (lepton = $\mu^{\pm}$ or $e^{\pm}$), with branching fractions of 14.8 % for both μ and e modes. The background for these channels is large but not intractable, with the principal background coming from W + multijet production. Searches in these decay modes can be enhanced by looking for a second lepton from one of the accompanying b quark decays. This method of 'tagging' the b quarks does have the cost of significantly reducing the 14.8 % branching fraction by an amount dependent on the efficiency of the tagging method.

The dilepton search modes are those in which both W's decay leptonically ($W \rightarrow \mu\nu$ and/or $W \rightarrow e\nu$). As shown in Fig. 2.10, the branching fractions for these

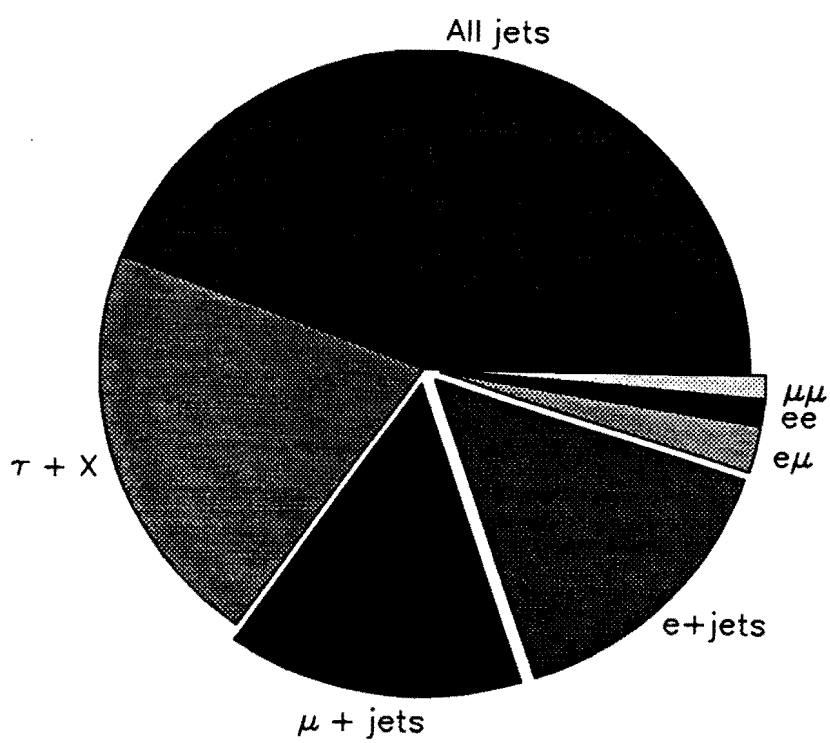

Figure 2.10 Fraction of $t\bar{t}$ cross section into the various decay channels.

channels are small (2.5 % for $e\mu$ and 1.2 % for each ee and $\mu\mu$), yet they have the smallest background from non-top processes and present the best opportunity for discovery of the top. The $e\mu$ is the cleanest decay mode with very few competing background processes, whereas the ee and $\mu\mu$ channels require more sophisticated analyses to separate the signal from competing Z^0 decays.

This thesis focuses on the search for top in the dimuon ($\mu\mu$) channel. The experimental search signature is thus:

- Two high p_T muons emitted centrally, approximately transverse to the colliding beams.
- Significant missing transverse energy $\not{E}_T$ from the two neutrinos emitted in the W decays.
- Two jets from the b quark hadronization.

CHAPTER 3
EXPERIMENTAL SETUP

3.1 The Tevatron

The Tevatron [3.1] [3.2] is the world's highest energy proton-antiproton accelerator system and the first large scale superconducting synchrotron. The ring, measuring two kilometers in diameter, is located at the Fermi National Accelerator Laboratory in the Illinois prairie west of Chicago. For the analysis described here, the Tevatron was operated at a beam energy of 900 GeV, providing a center of mass collision energy of 1.8 TeV. During the 1992-1993 collider run, the Tevatron delivered an integrated luminosity of 31.1 pb^{-1}, of which the DØ detector recorded 16.7 pb^{-1}.

The Fermilab accelerator complex is shown in Fig. 3.1. The process of colliding beams starts when protons from a bottle of hydrogen gas are accelerated in steps to 0.75 MeV, then to 200 MeV, and further to 8 GeV, starting with the Cockcroft-Walton generator, continuing through the Linac, and then into the Booster for injection into the Main Ring. Antiproton production begins when 120 GeV protons extracted from the Main Ring strike a nickel target. The resulting antiprotons are collected into the Antiproton source rings using an intense magnetic field. There they are stored and forced to similar orbits and energies through the process of stochastic cooling in the Debuncher and Accumulator rings of the Antiproton source [3.3] . When $\approx 10^{11}$ antiprotons have been accumulated, collision mode can ensue. Six bunches of 150 GeV protons are injected from the Main Ring into the Tevatron. Similarly, six bunches of antiprotons are extracted from the Accumulator, accelerated to 150 GeV in the Main

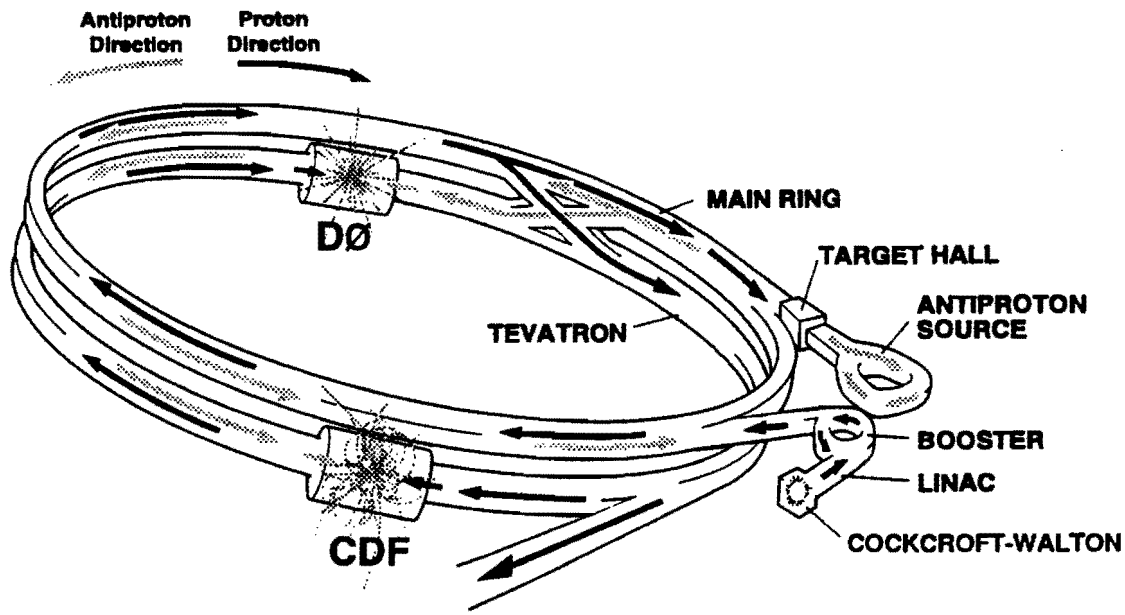

Figure 3.1 The accelerator complex at Fermilab.

Ring and injected into the Tevatron. The counter-rotating bunches of protons and antiprotons are then accelerated to 900 GeV and forced to collide at the centers of the DØ and CDF detectors.

3.2 The DØ Detector: An Overview

The DØ detector was designed to study high mass states and large p_T phenomena in proton-antiproton collisions at $\sqrt{s} = 2$ TeV. The design was optimized with the following emphases: efficient identification and measurement of electrons and muons, precise measurement of parton jets at large p_T and a well-controlled measure of missing energy ($\not{E}_T$) as a means to signal the presence of neutrinos and other non-interacting particles.

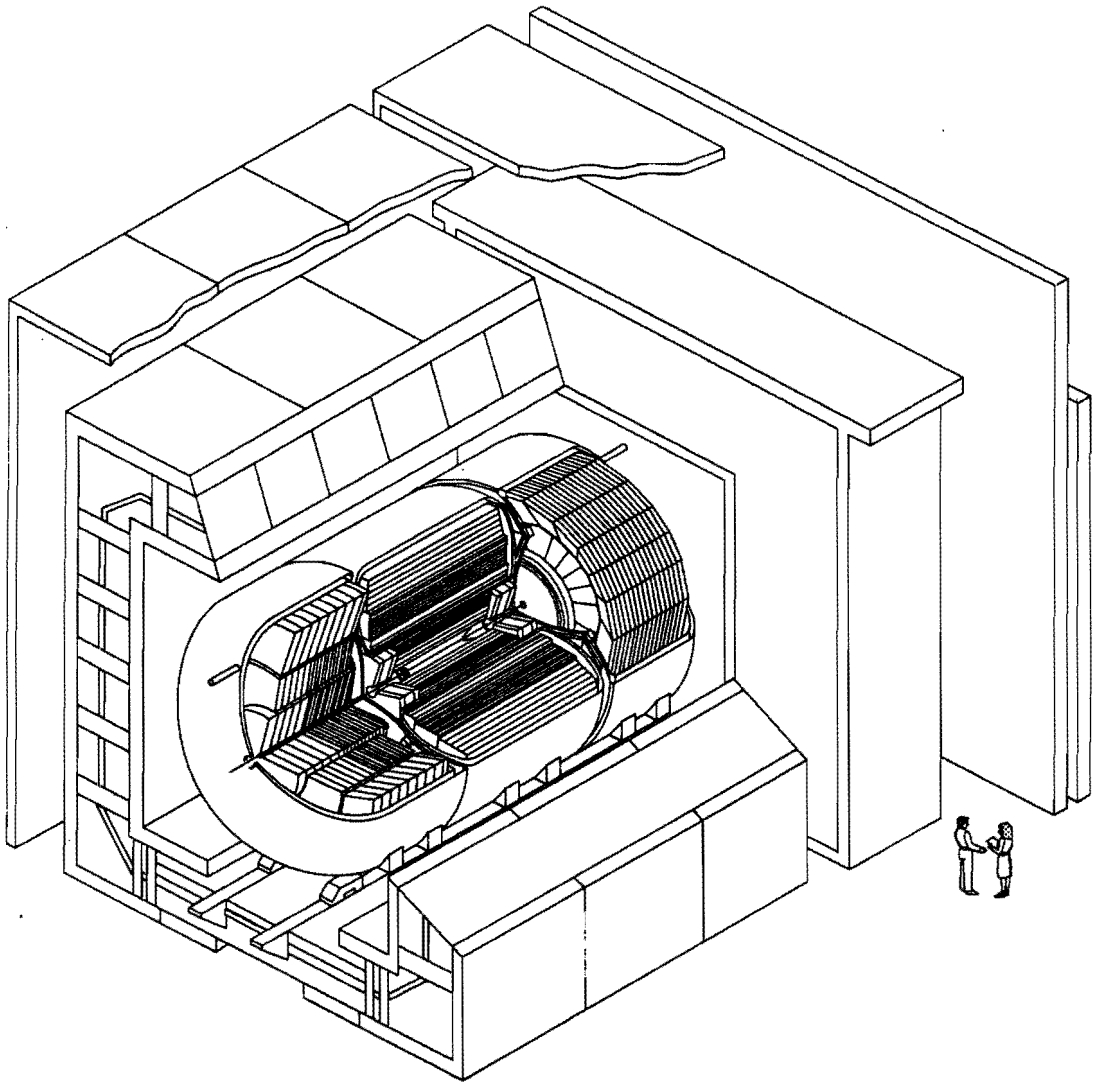

Figure 3.2 The DØ Detector

A cutaway view of the detector is shown in Fig. 3.2. The nested layers of the detector are described, from the collision point at the center of the detector working radially outward, as follows. The central detector is comprised of four subunits including: the vertex tracking chamber, the transition radiation detector, the central tracking chambers, and the pair of forward tracking chambers, one at each end. Next is

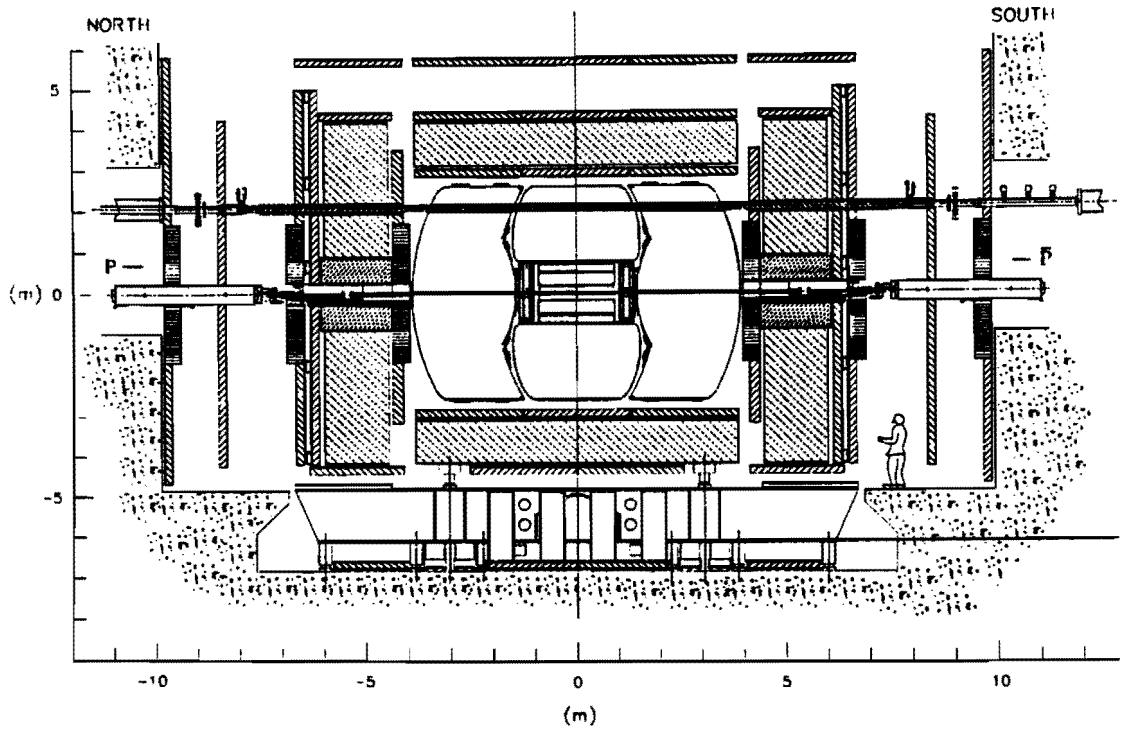

Figure 3.3 Elevation of the DØ Detector

the liquid argon-uranium calorimeter in three separate cryostats in a side by side arrangement. Finally there is the muon system, which is composed of three concentric shells of proportional drift tubes and incorporates a volume of iron to supply a toroidal magnetic field between the first and second shells. The following sections describe these components in more detail, with an emphasis on the parts of the detector relevant to this analysis. A more complete description of the DØ detector and its components, including electronics, triggering, data acquisition, mechanical support, high voltage and online monitoring and control systems can be found elsewhere [3.4]. The overall dimensions of the detector measure approximately 13 m wide × 13 m high × 20 m long (Fig. 3.3). It weighs over 25,000 metric tonnes, and has more than 100k readout channels.

DØ has adopted a right-handed coordinate system, in which the z-axis is along the proton direction (north to south), the y-axis upward and the x-axis to the east. The angles ϕ and θ are respectively the azimuthal and polar angles ($\theta = 0$ along the proton beam direction). The radial coordinate r denotes the perpendicular distance from the beam axis. Pseudorapidity, $\eta \equiv \ln(\tan(\frac{\theta}{2}))$, approximates the true rapidity $y = \frac{1}{2}\ln((E+p_z)/(E-p_z))$, for finite angles in the limit $(m/E) \rightarrow 0$.

3.3 Central Tracking and Identification

The Central Detector (CD) [3.5] consists of four distinct elements: The Vertex Drift Chamber (VTX), the Transition Radiation Detector (TRD), the Central Drift Chamber (CDC), and the pair of Forward Drift Chambers (FDC's). The VTX, TRD, and

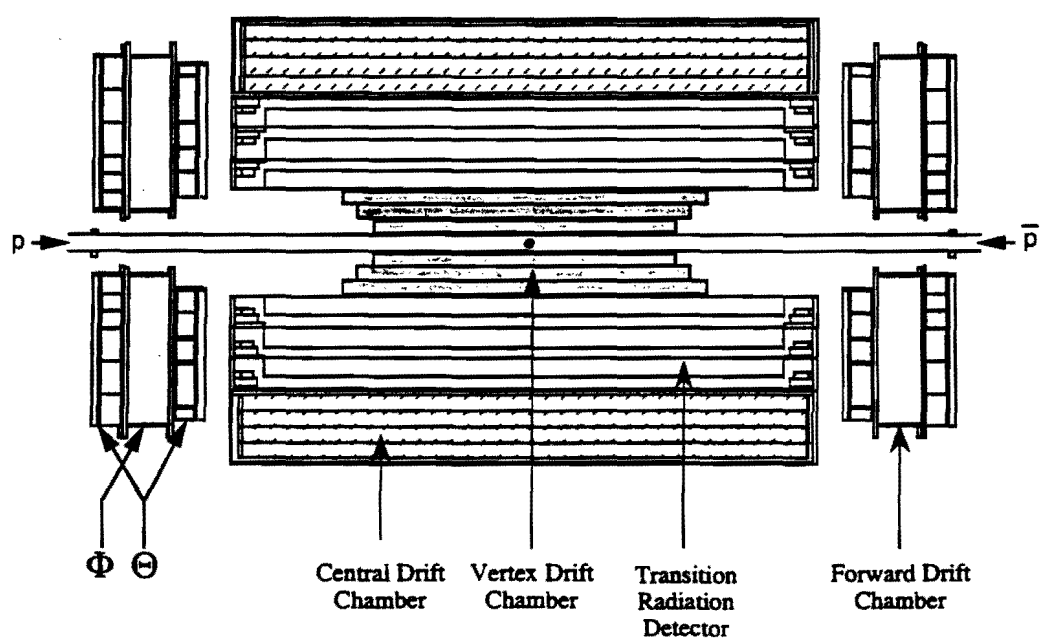

Figure 3.4 Layout of the central detectors

CDC cover the large angle region and are configured in three concentric cylinders around the beam pipe. The FDC's are oriented perpendicular to the beam pipe. Fig. 3.4 shows the layout of these detectors in side view. The full CD occupies the inner cylindrical aperture of the calorimeter cryostats, a volume given by $r = 78$ cm and $z = \pm 135$ cm.

The design of the tracking detectors was influenced by the absence of a central magnetic field. Without the need to measure momenta of charged particles, the central tracking detectors were optimized for two track resolving power, high efficiency, and good ionization energy (dE/dx) measurement to distinguish single electrons from the unopened e^+e^- pairs of photon conversions. The TRD was incorporated to give an additional factor of about 50 for rejection of pions above that given by the calorimeter alone. The transition between large angle tracking with wires parallel to the beam and the small angle tracking with wires perpendicular to the beam was matched to the corresponding transition in the calorimeters.

3.3.1 Vertex Tracking Chamber

The VTX [3.6] has an inner radius of 3.7 cm (just outside the beryllium beam pipe) and outer active radius of 16.2 cm and is made of three mechanically independent concentric layers of cells. The cell geometry (Fig. 3.5) consists of 16 cells in azimuth in the inner layer and 32 cells in each of the outer two layers. The cells have a jet chamber geometry with 9 guard wires on each side of the row of 8 sense wires, incorporating additional cathode and field cage wires for fine field shaping and aluminum traces on the carbon fiber support tubes for coarse field shaping. Adjacent sense wires are offset

Length of active volume:	Layer 1	96.6 cm
	Layer 2	106.6 cm
	Layer 3	116.8 cm
Radial interval (active)		3.7–16.2 cm
Radial wire interval		4.57 mm
Number of sense wires/cell		8
Number of sense wires		640
Type of gas		$CO_2(95\%)-C_2H_6(5\%)-H_2O(0.5\%)$
Pressure of gas		1 atm
Drift field		1.0–1.6 kV/cm
Average drift velocity		7.6–12.8 μm/ns
Gas gain at sense wires		4×10^4
Sense wire potential		+2.5 kV
Sense wire construction		25 μm NiCoTin
Guard wire construction		152 μm Au–plated Al

Table 3.1 Vertex Chamber Parameters

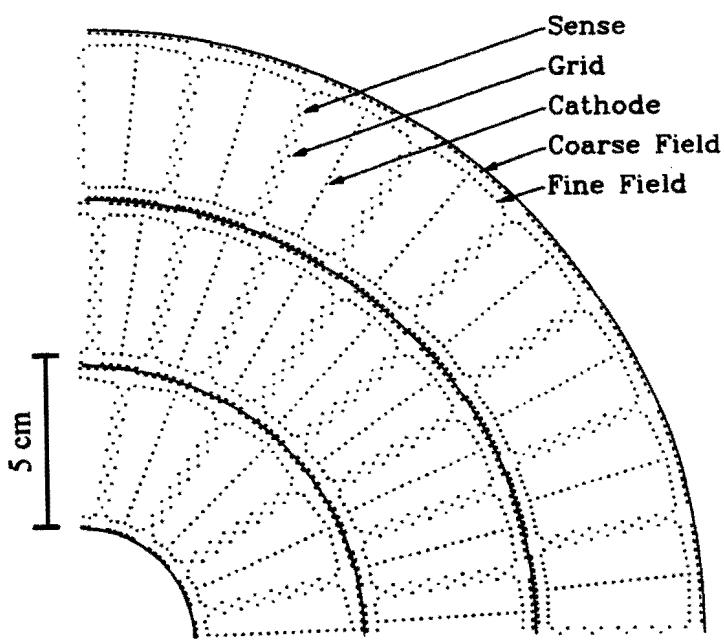

Figure 3.5 End view of VTX Detector

by 100 μm in ϕ to resolve left-right ambiguities, and the cells of the three layers are also offset in ϕ to further aid pattern recognition and facilitate calibration.

The gas chosen for operation of the VTX is CO_2(95%)-C_2H_6(5%) at one atmosphere pressure with a small admixture of H_2O(0.5%) to help stabilize the chamber in the high radiation environment. Under normal operating conditions of $\langle \vec{E} \rangle \approx 1\text{kV/cm}$, this gas provides spatial resolution of ~50 μm and good track pair resolving power with an average drift velocity of 7.3 μm/ns over a maximum distance of 13 mm, and gas gains near the sense wires of 4×10^4. Some characteristics of the VTX are listed in Table 3.1.

3.3.2 Transition Radiation Detector

The TRD [3.7] utilizes the phenomenon of transition radiation to provide electron identification to supplement that of the calorimeters. Transition radiation X-rays are produced when highly relativistic particles ($\gamma > 10^3$) traverse boundaries between media with different dielectric constants. The DØ TRD consists of three separate, concentric units, each containing a radiator stack and an X-ray detection chamber (Fig. 3.6). Each radiator stack consists of 393 foils of 18 μm thick polypropylene, separated by 150 μm, immersed in a volume of nitrogen gas. The energy spectrum of the X-rays is determined by the thickness of the radiator foils and the gaps between them. For the DØ TRD, the energy distribution peaks at 8 keV and is mainly contained below 30 keV [3.8].

X-ray detection is accomplished using a time-expansion radial-drift proportional wire chamber mounted just after the radiator. The X-rays convert in the xenon mixture, $Xe(91\%)-CH_4(7\%)-C_2H_6(2\%)$, usually in the first few millimeters of the conversion gap. The X-ray conversions and ionization delta-rays produce clusters of charge which arrive at the sense wire over the full 0.6 μs drift time interval. The combination of time of arrival (position of X-ray conversion), total charge collected, and the cluster structure of the charge collected are used to discriminate between electrons and hadrons with p_T below 200 GeV/c.

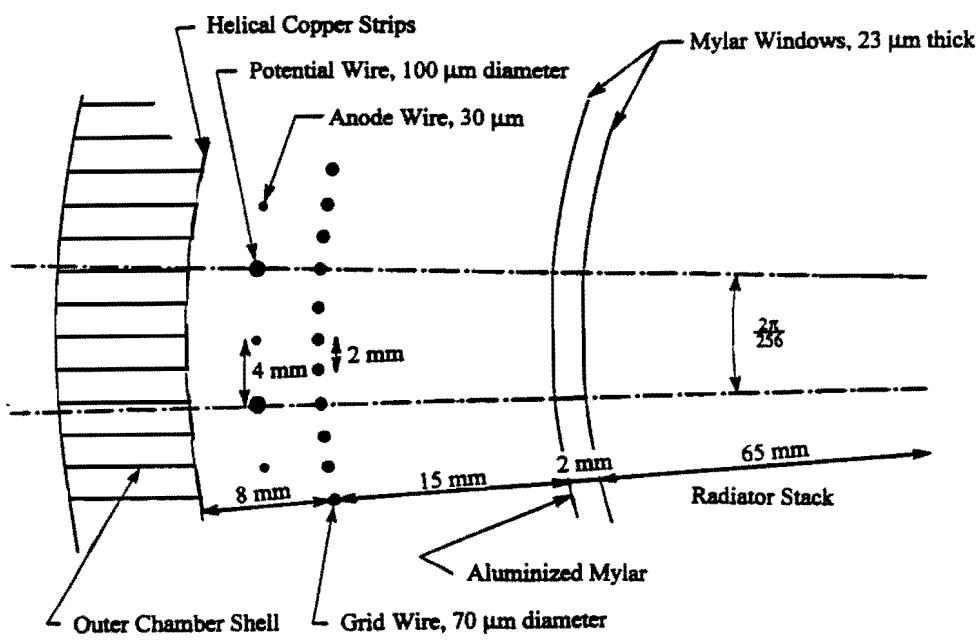

Figure 3.6 Cross section through the Transition Radiation Detector.

3.3.3 Central Tracking Chamber

The CDC [3.9] provides additional large angle tracking just prior to the Central Calorimeter. The tracking volume geometry is that of a cylindrical shell (184 cm in length, spanning radially from $r = 49.5$ cm to $r = 74.5$ cm), composed of four separate layers, each divided into 32 cells in the (r,ϕ) plane. Each CDC cell contains 7 sense wires (staggered in ϕ by $\pm$ 200 μm) and 2 delay lines running parallel to the beam pipe. Thus each particle passes near 28 sense wires and 8 delay lines. Fig. 3.7 shows the end view of the CDC. Outlined are the sense wires, guard wires and delay lines, which are embedded in the inner and outer shelves of each cell. Signals induced on the delay lines

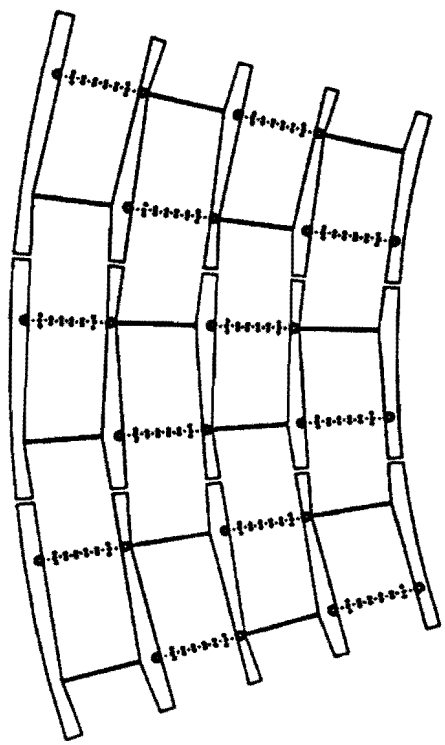

Figure 3.7 End view of CDC Detector cells

from the nearest neighboring anode wire are timed at both ends to give an axial coordinate with an accuracy of about 3 mm, thus allowing space point read out.

With a drift field of 620 V/cm, the drift velocity is 34 μm/ns for a gas mixture of $Ar(93\%)-CH_4(4\%)-CO_2(3\%)$; and gains near the sense wires are of the order of 10^4 with the normal operating potential of 1.5 kV. This produces a drift resolution of about 200 μm. Pulse pair resolutions are important in the non magnetic environment of DØ. Using offline superposition of single track test beam data on a full section of CDC chambers, 90% efficiency is obtained for finding 2 mm separations. It is equally important for the tracking chambers to distinguish an unresolved overlay of two tracks (e.g., γ-conversions) from a single track. Fig. 3.8 shows the ionization distributions for one and two track traversals of a single cell. In this plot the ionization signal is taken to be the sum of the deposited energy associated with the 70 % of the hits participating in the track which have the smallest associated energy deposition: this greatly reduces the effects of δ-ray production. Studies show the CDC can supply rejection factors in the range of 75-100 with 98% efficiency for retaining single tracks. Characteristics of the CDC are listed in Table 3.2.

Length of active volume	179.4 cm
Radial Interval (active)	51.8–71.9 cm
Number of layers	4
Radial wire interval	6.0 mm
Number of sense wires/cell	7
Number of sense wires	896
Number of delay lines	256
Type of gas	$Ar(93\%)-CH_4(4\%)-CO_2(3\%)$
Pressure of gas	1 atm
Drift field	620 V/cm
Average drift velocity	34 μm/ns
Gas gain at sense wire	2.6×10^4
Sense wire potential	+1.5 kV
Sense wire construction	30 μm Au–plated W
Guard wire construction	125 μm Au–plated CuBe

Table 3.2 Central Drift Chamber Parameters

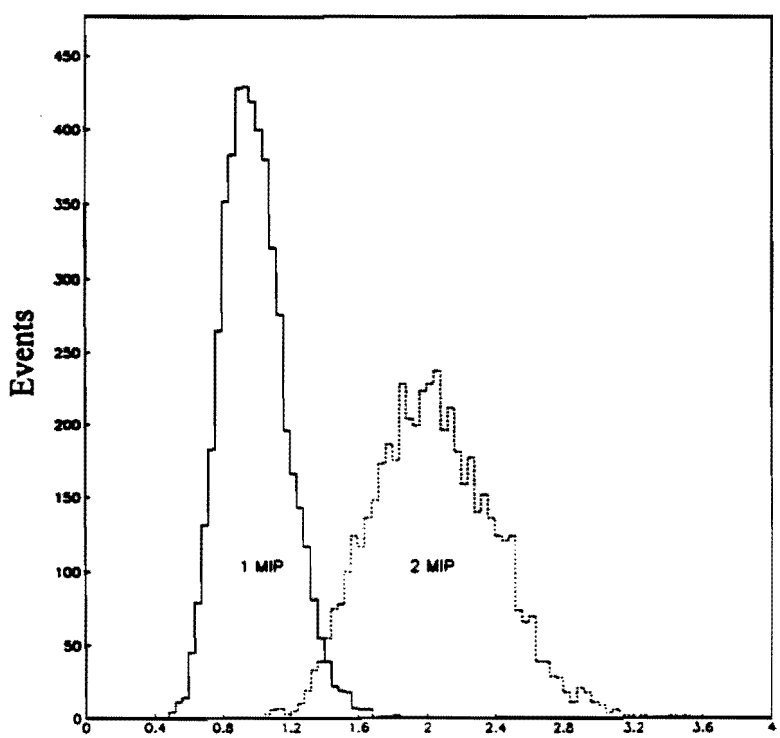

Figure 3.8 Discrimination of conversion pairs in the CDC.

3.3.4 Forward Tracking Chambers

The FDC's extend the coverage for charged particle tracking down to $\theta \approx 5°$ with respect to the beam pipe. The FDC packages are positioned at each end of the CD volume. Each package consists of three separate chambers: the Φ module with radial sense wires to measure the ϕ coordinate, sandwiched between a pair of Θ modules with sense wires which measure (approximately) the θ coordinate. Fig. 3.9 indicates the sense wire orientations for the modules in one end package. The Φ module is a single chamber of 32 sectors, covering full 2π azimuth, with each sector incorporating 16 sense wires along the z-coordinate. The Θ module consists of four separate quadrants, each containing six rectangular cells, each with eight anode wires in z, and one delay

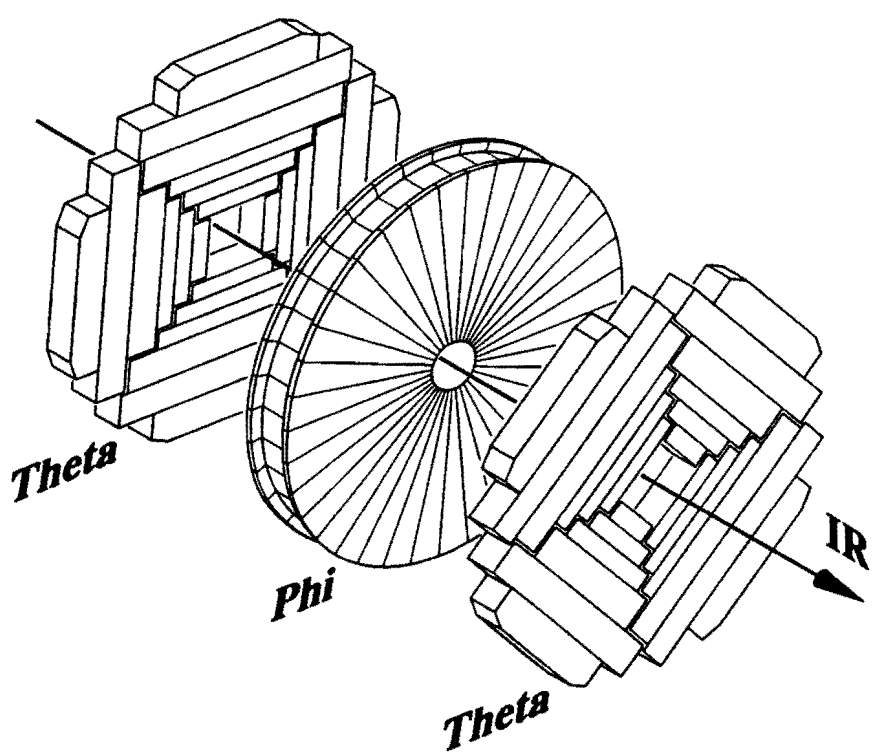

Figure 3.9 Wire orientation of a Forward Drift Chamber.

	Θ modules	Φ modules
z interval	104.8–111.2 cm	113.0–127.0 cm
	128.8–135.2 cm	–
Radial interval	11–62 cm	11–61.3 cm
Number of cells in radius	6	–
Maximum drift distance	5.3 cm	
Sense wire staggering	0.2 mm	
Sense wire separation	8 mm	
Angular interval/cell	–	10°
Number of sense wires/cell	8	16
Number of delay lines/cell	1	0
Number of sense wires/end	384	576
Number of delayline readouts/end	96	–
Type of gas	$Ar(93\%)-CH_4(4\%)-CO_2(3\%)$	
Pressure of gas	1 atm	
Drift field	1.0 kV/cm	
Average drift velocity	37 μm/ns	40 μm/ns
Gas gain at sense wire	$2.3, 5.3\times10^4$	3.6×10^4
Sense wire potential	+1.5 kV	
Sense wire construction	30 μm NiCoTin	
Guard wire construction	163 μm Au–plated Al	

Table 3.3 Forward Drift Chamber Parameters

line of identical construction to the CDC in order to give measurement of the orthogonal coordinate. The upstream and downstream Θ modules in a package are rotated 45° in ϕ with respect to each other.

The FDC's are operated with the same gas as the CDC, resulting in similar values of drift field and gas gain. The single delay line resolution is near 4 mm and drift resolutions of about 200 μm are obtained. Parameters of the FDC's are listed in Table 3.3.

3.4 Calorimetry

The calorimeter is the central feature and main emphasis of the DØ detector. The relevant entities to be detected, for the high p_T physics DØ was designed for, are jets, leptons, and neutrinos in the form of missing E_T. Calorimetry is a paramount tool for these, especially at the large energies encountered in this experiment, for which calorimetric energy resolution exceeds magnetic resolution. To the extent that jets represent the quanta of interest, calorimetry treats all the fragmentation products (photons, charged and neutral hadrons) on an equal basis. However, the lack of a magnetic field is significant in that the calorimeter must now play a major role in the identification of electrons, photons, jets, and muons. DØ optimizes the design of the calorimeter with respect to electron identification and jet separation (fine segmentation), $\boldsymbol{E}_T$ resolution (hermeticity), and mass resolution (energy resolution). At DØ, calorimetry also plays a vital role in the identification of muons.

3.4.1 Overview: The Liquid Argon-Uranium Calorimeters

The DØ calorimeter [3.10] is shown in a cutaway isometric view in Fig. 3.10. The calorimeter consists of three modules, a central module (CC) and two "end cap" modules (ECs) each encased in its own cryostat. Each module is further broken down into three basic components: an electromagnetic section, a fine hadronic section, and a coarse hadronic section.

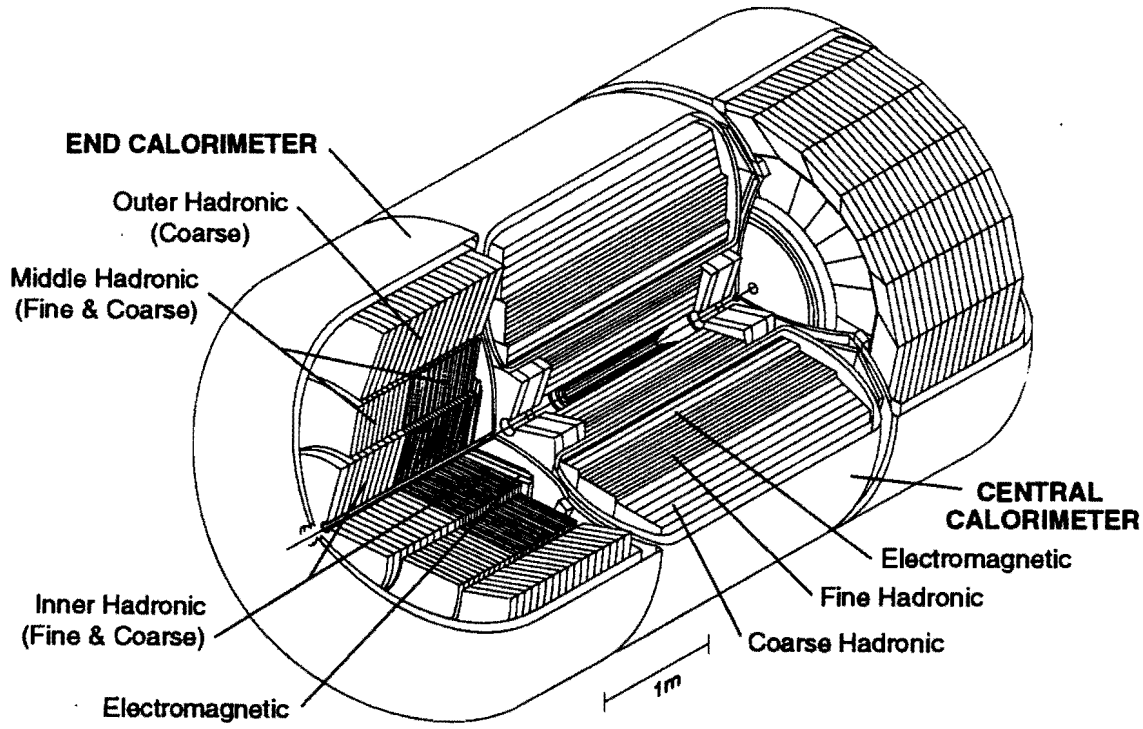

Figure 3.10 The DØ LAr-U Calorimeter.

The DØ calorimeter is a sampling calorimeter, utilizing depleted uranium as the absorber and liquid argon as the active medium. A typical calorimeter unit cell is depicted in Fig. 3.11. Each active layer of the calorimetry consists of a two-layer signal board with pad patterns scribed into the mid plane of the board, and high resistance epoxy coatings on both exterior surfaces which form the high voltage electrodes. The electric field is established by grounding the metal absorber plate and connecting the resistive surfaces of the signal boards to a positive high voltage (typically 2.0 - 2.5 kV). Ionization current from the 2.3 mm liquid argon gaps on either side of the signal board is capacitively coupled to the signal pads and typical drift times are roughly 450 ns. Ganging of pads in depth is accomplished by local jumpers at the edges of modules;

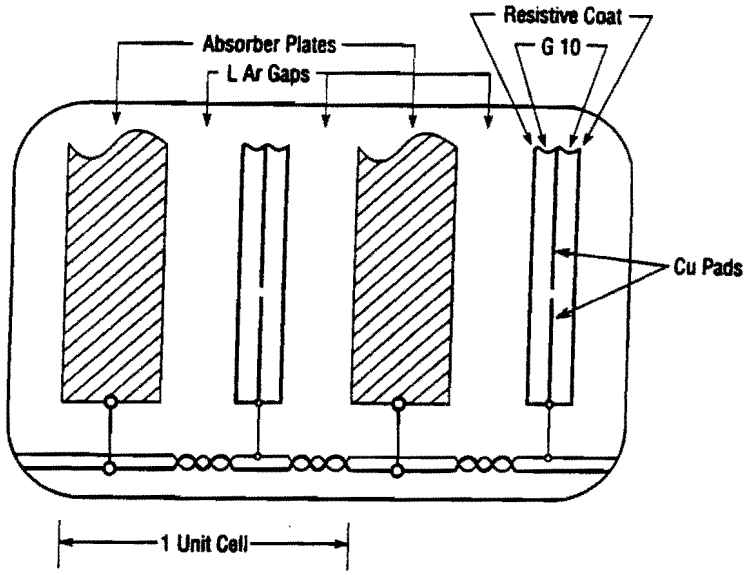

Figure 3.11 Calorimeter unit cell

signals are brought to the module ends between readout layers, and routed to feed-throughs on the cryostat body to preamplifier boxes.

The pattern and size of a readout cell is determined by the shape of the copper pads sandwiched in between the resistive coatings on the G-10 circuit boards. The transverse size of the readout cells was chosen to be comparable with the transverse size of typical showers: approximately 2 cm for electromagnetic and 10 cm for hadronic showers. The overall geometry is configured to have a 'pseudo-projective' set of readout towers, with each tower consisting of layers of ganged pad readouts. The term pseudo-projective refers to the fact that the centers of readout cells of increasing shower depth lie on rays projecting from the center of the interaction region, but the cell boundaries are aligned perpendicular to the absorber plates. Fig. 3.12 depicts this segmentation pattern of the calorimeter, in which the typical transverse tower size is $\Delta\eta \times \Delta\phi \approx 0.1 \times 0.1$.

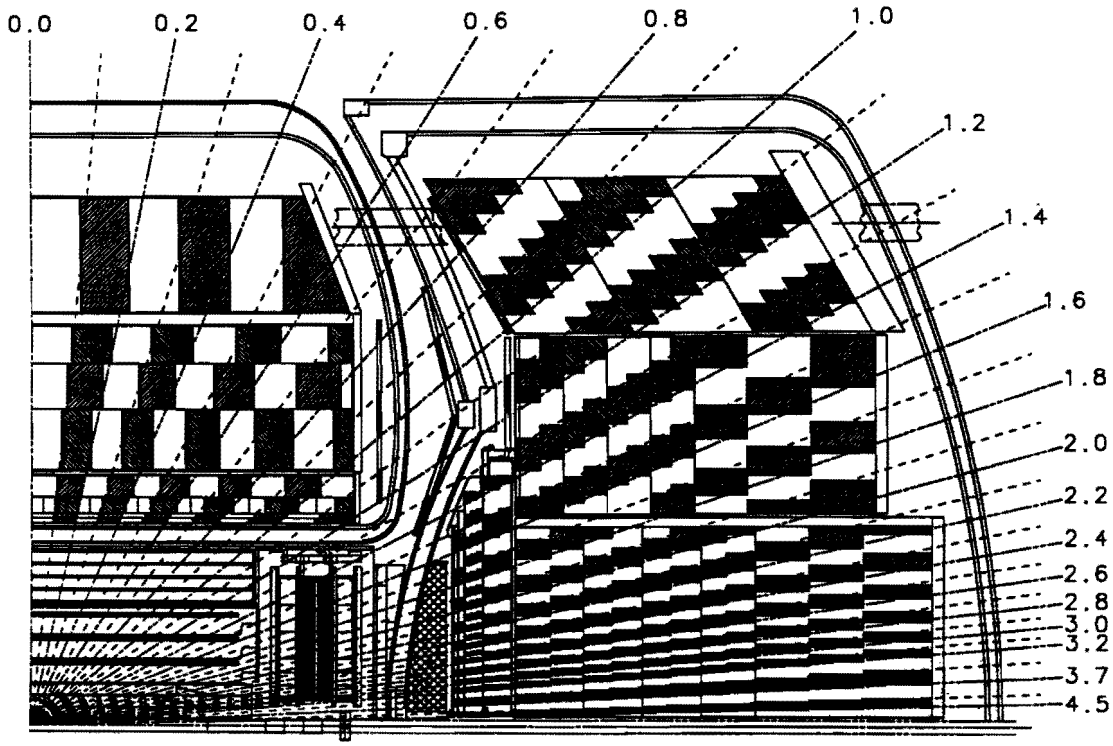

Figure 3.12 Quadrant of Calorimeter showing radiative tower geometry

3.4.2 The Central Calorimeter

The central calorimeter (CC) consists of three concentric shells oriented parallel to the beam pipe. The 32 inner electromagnetic (EM) modules use 3 mm thick uranium as the absorber and contain four separate readout layers. The first two layers, each 2 radiation lengths (X_0) thick, are incremented to measure the longitudinal shower development near the beginning of the showers where photons and π^0's differ statistically. The third layer spans the region of maximum EM shower energy deposition and the forth layer completes the EM coverage to 20 X_0. At the EM shower maximum, the third layer is twice as finely segmented in both η and ϕ to allow more precise location of shower centroids. The 16 fine hadronic modules use 6 mm uranium

	EM	FH	CH
Rapidity coverage	±1.2	±1.0	±0.6
Number of modules	32	16	16
Absorber	Uranium	Uranium	Copper
Absorber thickness	3 mm	6 mm	46.5 mm
Argon gap	2.3 mm	2.3 mm	2.3 mm
Number of cells/module	21	50	9
Number of readout layers	4	3	1
Cells/readout layer	2,2,7,10	20,16,14	9
Total radiation lengths	20.5	96.0	32.9
Total absorption lengths	0.76	3.2	3.2
Sampling fraction	11.79 %	6.79 %	1.45 %
Total number of readout cells	10,368	3000	1224

Table 3.4 Central Calorimeter Parameters

absorbers and are divided into three separate readout layers (1.3, 1.0 and 0.9 absorption lengths). Sixteen coarse hadronic modules form the outer ring of central calorimetry and have 46.5 mm thick copper absorbers formed into one readout layer in depth which has the standard transverse $\Delta\eta \times \Delta\phi = 0.1$ tower size. Parameters of the Central Calorimeter are listed in Table 3.4.

3.4.3 The End Cap Calorimeters

The two endcap calorimeters are similar in gap and readout structure to the central calorimeter. They extend the calorimeter coverage out to $|\eta| = 4.5$. Four sets of modules fill each cryostat. A single electromagnetic module, with 3 mm uranium plates, is located within the thin domed front wall. Behind this is a single cylindrical 'inner' hadronic module of many absorption lengths. Both of these modules use multi-layer signal readout boards with interior embedded traces to deliver the signals to the outer

periphery for ganging in depth. Sixteen 'middle' hadron calorimeter modules surround the inner module in a ring. Both inner and middle hadronic modules use 6 mm uranium absorber for the first half of their depth and 46.5 mm stainless steel thereafter. The inner modules are in turn surrounded by a ring of 16 'outer' modules that are constructed solely from 46.5 mm stainless steel plates. The depth and transverse segmentation in the endcaps are similar to the central module, except for rapidities above 2.6 where the tower size doubles since the transverse linear dimensions have shrunk to less than typical shower size. Parameters of interest of the End Calorimeters are found in Table 3.5.

3.4.4 The Intercryostat Detectors

The use of liquid argon as the sampling medium requires the calorimeter elements be contained in cryostats. For practicality of design, the calorimeter is divided

	EM	IFH	ICH	MFH	MCH	OH
Rapidity coverage	1.3–3.7	1.6–4.5	2.0–4.5	1.0–1.7	1.3–1.9	0.7–1.4
Number of modules	1	1	1	16	16	16
Absorber	Uranium	Uranium	Stainless Steel	Uranium	Stainless Steel	Stainless Steel
Absorber thickness	3 mm	6 mm	6 mm	6 mm	46.5 mm	46.5 mm
Argon gap	2.3 mm	2.1 mm	2.1 mm	2.2 mm	2.2 mm	2.2 mm
No. cells/module	18	64	12	60	14	24
No. readout layers	4	4	1	4	1	3
Cells/readout layer	2,2,6,8	16	14	15	12	8
Tot. radiation lengths	20.5	121.8	32.8	115.5	37.9	65.1
Tot. absorb. lengths	0.95	4.9	3.6	4.0	4.1	7.0
Sampling fraction	11.9%	5.7%	1.5%	6.7%	1.6%	1.6%
No. readout channels	7488	4288	928	1472	448	960

Table 3.5 End Calorimeter Parameters

into three separate cryostat vessels. The area between these cryostats, roughly given by $0.8 \leq |\eta| \leq 1.4$, is instrumented with scintillation counter arrays called intercryostat detectors (ICD) that are mounted on the front surfaces of the EC's. Each ICD (one on each side of the CC) consists of scintillator tiles, $\Delta\eta \times \Delta\phi = 0.1$ in size, matching the pseudo-projective structure of the CC and EC's and totaling to 192 channels for each detector array. The plastic scintillating tiles are read out by phototubes and their response is calibrated using optical fibers which distribute light from a UV laser to each tile.

The shower development near the regions of the cryostat boundaries is further sampled by an additional subsystem called the Massless Gap (MG) detectors. These are single readout boards within the cryostats placed between the calorimeter elements and the cryostat wall; they are not sandwiched within absorber plates but instead use the stainless steel of the cryostat walls as the absorbing medium. The ICD together with the MG provide a good approximation to the standard DØ sampling of electromagnetic showers, and to a lesser degree, hadronic showers.

3.4.5 Calorimeter Performance

Extensive studies of the performance of calorimeter modules in beam tests [3.11][3.12] were made using pions and electrons with energies between 10 and 150 GeV. The resolution is parameterized as

$$\left(\frac{\sigma}{E}\right)^2 = C^2 + \frac{S^2}{E} + \frac{N^2}{E^2},$$

where C is the constant term that represents the calibration errors, S is the sampling fluctuations term, and N is the noise term which includes electronic and uranium noise. From test beam it is found that for electrons

$$C = 0.003 \pm 0.002, \quad S = 0.157 \pm 0.005 (\mathrm{GeV})^{\frac{1}{2}}, \quad N \approx 0.140 \text{ GeV}$$

and for pions

$$C = 0.032 \pm 0.004, \quad S = 0.41 \pm 0.04 (\mathrm{GeV})^{\frac{1}{2}}, \quad N \approx 1.28 \text{ GeV}.$$

The position resolution is 0.8–1.2 mm over the full range of impact positions. The

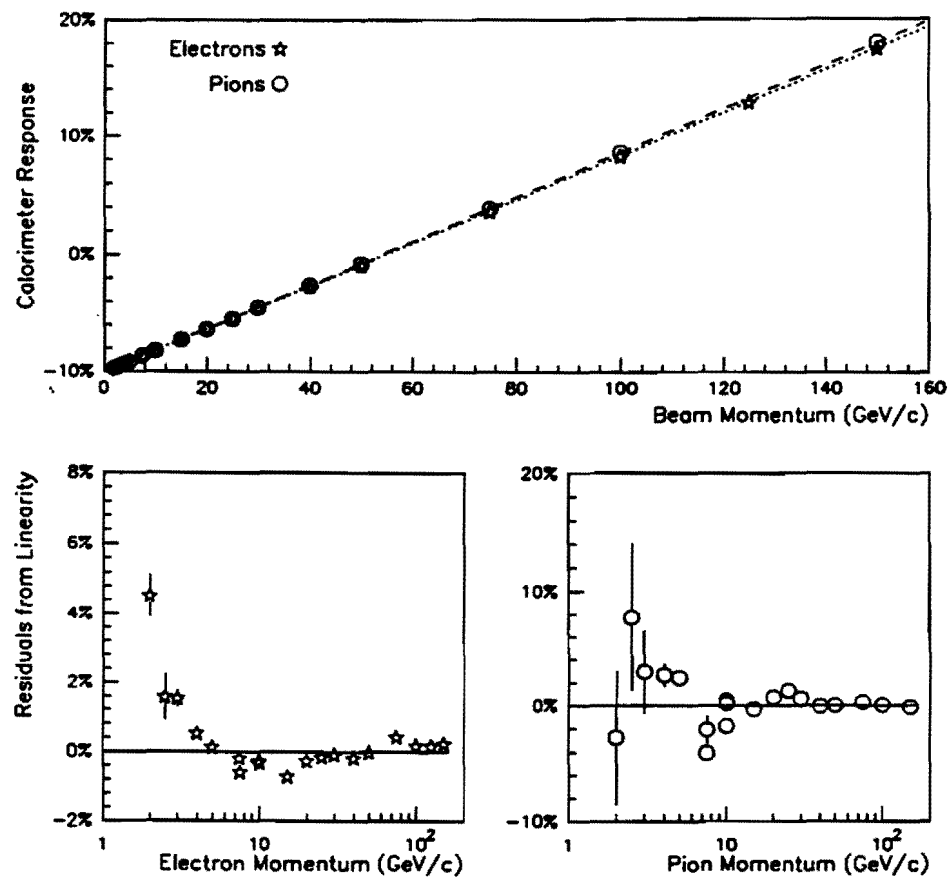

Figure 3.13 Calorimeter response vs. test beam momentum (top), Residuals from linearity vs. momentum of beam: electrons (bottom left) and pions (bottom right).

resolution has an energy dependence which varies approximately as $1/\sqrt{E}$. The resolution and linearity obtainable in the calorimeter is closely related to the ratio of response of electrons and pions. The e/π ratio falls from about 1.11 at 10 GeV/c^2 to about 1.04 at 150 GeV/c^2. The calorimeter response and residuals from linearity for test beam electrons and pions is shown in Fig. 3.13 (taken from Ref. [3.13]).

The calorimeter plays an important role in the identification of muons and rejection of cosmic rays. To illustrate the sensitivity of the calorimeter, Fig. 3.14 shows the energy seen in the CC Fine Hadronic Layer 1 in a tower centered on cosmic ray tracks.

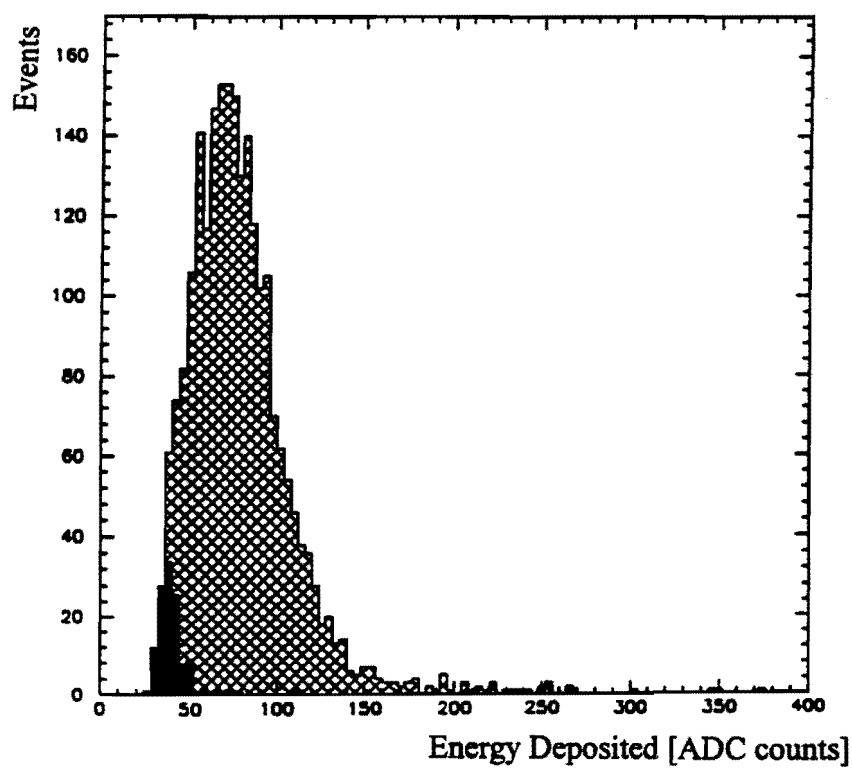

Figure 3.14 Energy deposition by cosmic ray muons in the CCFH Layer 1. Noise contributions (dark shading) deduced from signals observed far from cosmic ray track. Data is plotted with a 3-σ suppression.

3.5 Muon Spectrometer

Muon detection in DØ is made by measurements of muon track coordinates before and after magnetized iron toroids. The muon spectrometer consists of five distinct solid iron toroidal magnets together with a set of proportional drift tube chambers (PDT's) which measure tracks down to 3° relative to the beam.

A closely spaced set of measurements of the muon track prior to the toroid provides the entry point; two sets of measurements separated by 1 to 3 meters after the toroid yield the exit direction. Fig. 3.3 illustrates this configuration. The incident trajectory is determined from a combination of the primary interaction point, the track

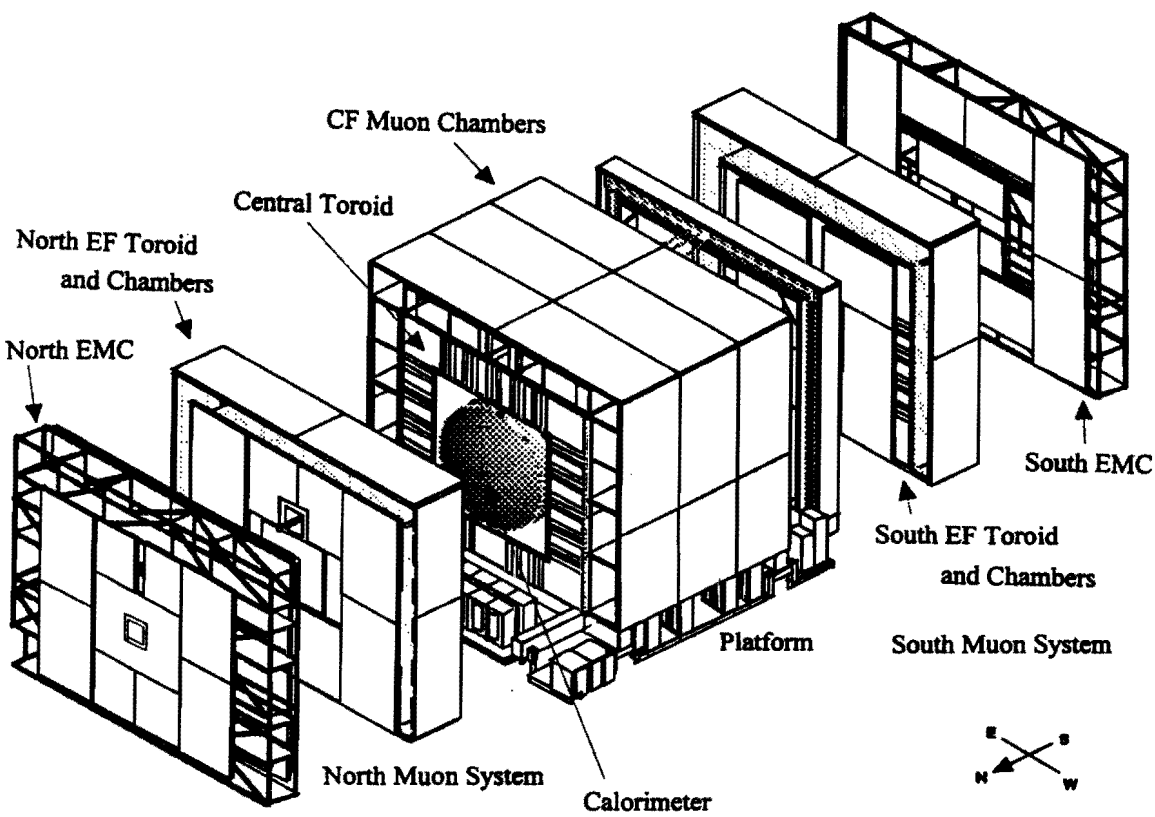

Figure 3.15 Expanded view of the DØ muon system

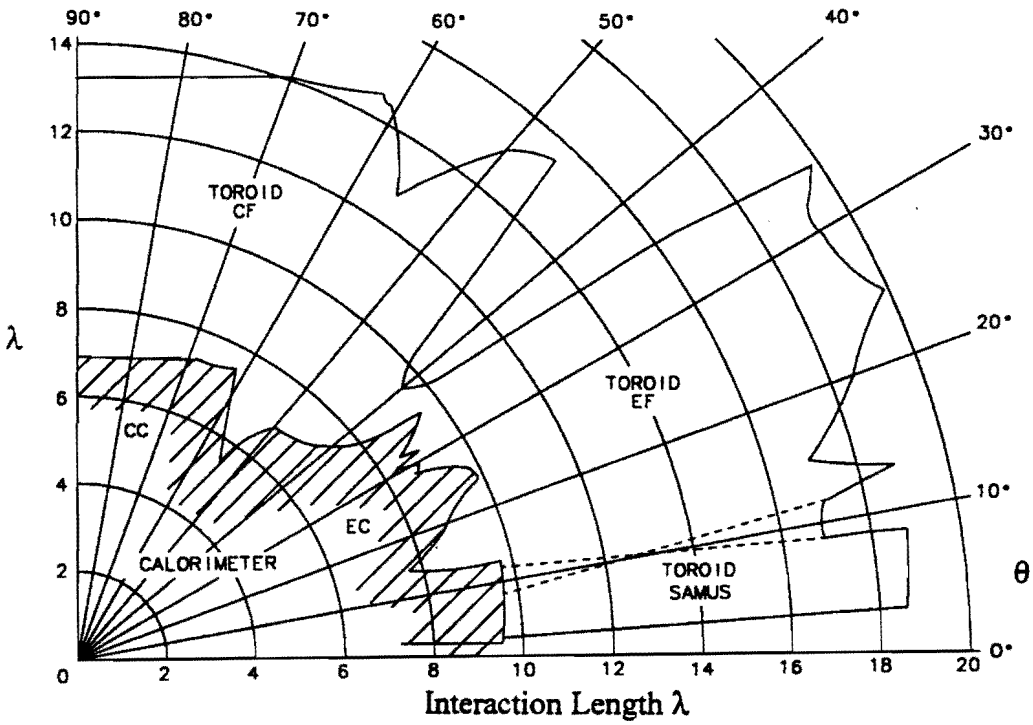

Figure 3.16 DØ muon system: absorption lengths (λ) vs. angle from the beam (θ)

seen in the central tracking and the track segment in the first muon chamber . A minimum ionizing trace in the calorimeter is used as a confirmation for isolated muon tracks. A comparison of incident and exit muon directions provide the bend angle through the 2 Tesla field in the iron, and hence the momentum. Multiple Coulomb scattering in the iron toroids limits the relative momentum resolution to ≥ 18 % up to the limit imposed by the bend coordinate resolution in the PDT's. With final precise alignment of the muon chambers, three standard deviation determination of sign is expected for $p_T \leq 200$ GeV/c at $\eta = 0$, and $p_T \leq 30$ GeV/c at $|\eta| = 3.3$.

The muon spectrometer is divided into two subsystems: the Wide Angle Muon Spectrometer (WAMUS), which includes the PDT's surrounding the CF toroid ($|\eta| \leq 1$) and two EF toroids ($1 < |\eta| \leq 2.5$); and the Small Angle Muon Spectrometer (SAMUS),

which utilizes PDTs of different construction around the SAMUS toroids ($2.5 \leq |\eta| \leq 3.6$). These are embedded in the central holes of the EF's (see Fig. 3.15). Each toroid is a square annulus centered on the Tevatron beamline and magnetized with water cooled copper coils. The field within the toroids is modeled to produce a map for input into the reconstruction software, necessitated by the variation in field strength across the square cross sections. Peak field strength within the iron is about 2 Tesla.

The combined depth of material in the calorimeter and toroids varies from about 13 absorption lengths at $\eta = 0$, to 18 absorption lengths at small angles (Fig. 3.16), giving effective confinement of hadronic showers with minimal track leakage. This feature has the important benefit of enabling measurements of muons within the core of jets. Some important parameters of the muon system are listed in Table 3.6.

3.5.1 Wide Angle Muon System

WAMUS provides measurements for muons traversing the CF and most of those which cross the EF toroids. The system [3.14] consists of 164 distinct proportional drift tube chambers with sizes up to $2.5 \times 5.8\,\mathrm{m}^2$. The chambers are deployed in three layers: the "A" layer before the iron toroids and the "B" and "C" layers after the magnets (see Fig. 3.19). The distance between the B and C layers is ≥ 1 m, to provide sufficient lever arm for an accurate measurement of the muon direction after it exits the magnet.

Each chamber consists of PDT's in the form of a rectangular cell 10.1 cm wide by 5.5 cm high. The cell structure is the same for all of the WAMUS chambers and they differ mainly in the number of cells in depth (3 or 4), and in cell length (191 to 579 cm). The cells are formed from extruded aluminum with the cells at different radii staggered

to permit resolution of the left – right drift ambiguities (Fig. 3.17a). The "A" layer has four planes of drift tubes, while the "B" and "C" layers have three planes each. Cathode pad strips are attached to the top and bottom of each cell and a single anode wire is mounted at the center of the cell (see Fig. 3.17b). A drift field is then formed by holding the aluminum extrusion at ground and the cathode pads and anode wires at +2.3 kV and +4.6 kV respectively. The chambers are operated using a gas mixture of $Ar(90\%)CF_4(5\%)CO_2(5\%)$ for which the above potential gives a drift velocity of about 6.5 cm/μm. The wires are oriented along the primary $\vec{B}$-field direction ($\vec{B} \approx B\hat{\varphi}$) such that accurate measurement of the bend coordinate (η) is provided by drift time measurement. The drift resolution is approximately 0.2 mm.

The "A" layer with its four planes of PDT's is 17 cm from the innermost to the outermost sense wire. For the drift resolution of 0.2 mm, the accuracy in the bend view is ±0.6 mrad for the angle of the incident particle into the toroid and $\pm 0.2/\sqrt{4} = 0.1$ mm for the entrance position. The distance between the center of the "B" and "C" layers is

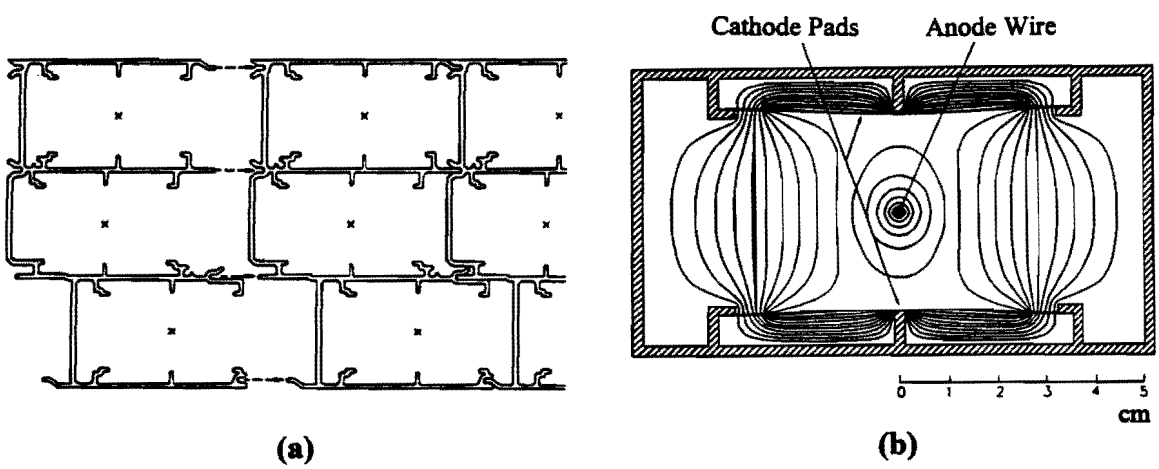

Figure 3.17 Cross sections of: (**a**) WAMUS muon chamber assembly (3 deck shown), and (**b**) WAMUS cell showing anode wire and cathode pads with associated equipotential lines.

136 cm. The position and angle of the outgoing particle are determined to ±0.17 mm and ±0.2 mrad respectively.

The measurement along the wire direction is made using the cathode pad strips. Each strip contains two pads separated by a repeating diamond insulating pattern. For charges induced at the cathode strips, the ratio of inner and outer pads provides a measurement of the longitudinal coordinate, to within half the length of the diamond pattern (Fig 3.18). The measurement ambiguity is resolved by using the difference in time of signal arrival at the two ends of the wire. This method yields a resolution in the non–bend (φ-coordinate) view of about 2.0 mm.

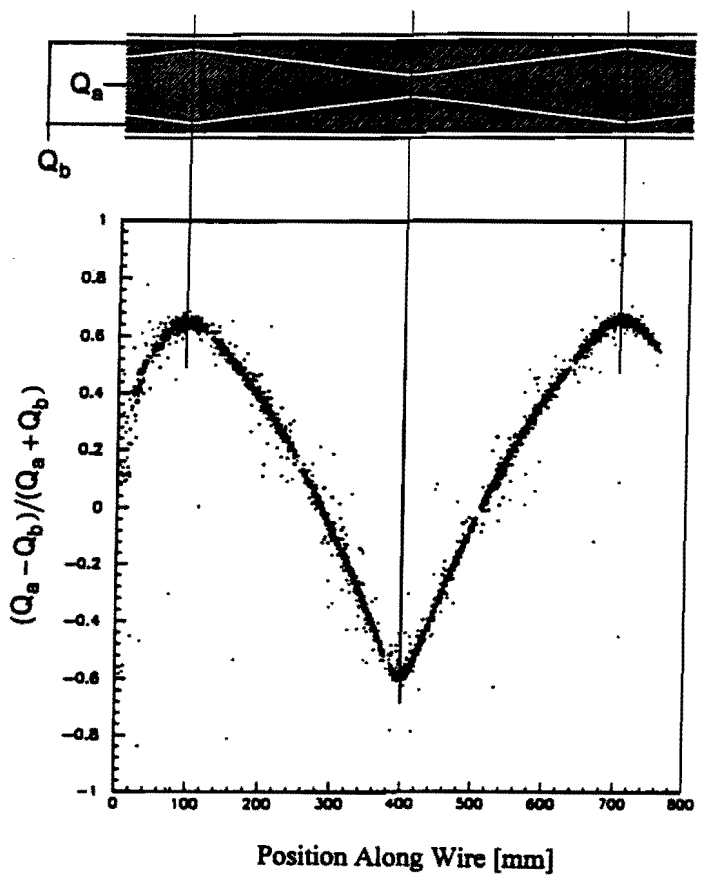

Figure 3.18 Cathode pad strip and associated charge ratio vs. distance plot.

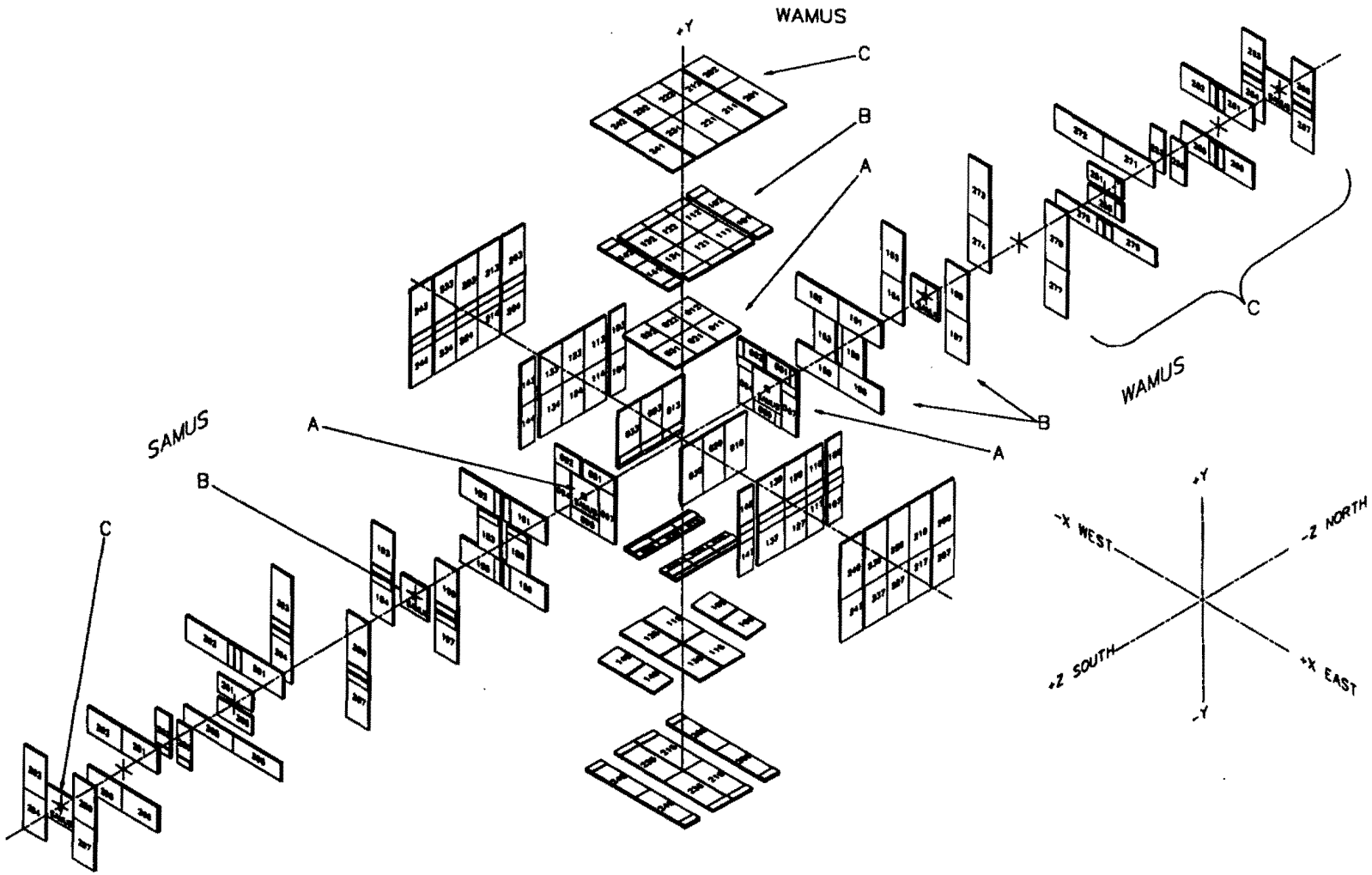

Figure 3.19 Exploded view of the DØ Muon system

	WAMUS	SAMUS
Rapidity coverage	$\lvert\eta\rvert \leq 1.7$	$1.7 \leq \lvert\eta\rvert \leq 3.6$
Magnetic field	2 T	2 T
Number of chambers	164	6
Interaction lengths	~ 13	~ 18
Bend-view resolution	± 0.53 mm	± 0.35 mm
Non-bend resolution	± 3 mm	± 0.35 mm
Gas	$ArCF_4CO_2$ 90:5:5	CF_4CH_4 90:10
Average drift velocity	6.5 cm/μs	9.7 cm/μs
Anode wire voltage	+4.56 kV	+4.0 kV
Cathode pad voltage	+2.30 kV	–
Number of cells	11,386	5308

Table 3.6 Muon system parameters

3.5.2 Small Angle Muon System

Each SAMUS station [3.10] covers a 312×312 cm^2 square area perpendicular to the exit beams (Figs. 3.15 and 3.19). The system is also arranged in 3 layers, one preceding the toroid and two after. Each layer is constructed out of 29 mm internal diameter cylindrical proportional drift tube chambers arranged into three planes. The PDT's in such a plane are two tubes deep and are overlapping in a closely packed array with adjacent tubes offset by one half of a tube diameter. Each layer has a plane of PDT's oriented in each the x, y and u directions (u is at 45° with respect to x and y). The u chambers are used for multi-track correlations to enable tracking of individual particles in this high multiplicity region of the detector.

The SAMUS PDT's are constructed from 3 cm external diameter stainless steel tubes with individual end plugs for provision of gas and electrical connections. The

system is operated with $CF_4(90\%)CH_4(10\%)$ gas with average drift velocity of 9.7 cm/μs resulting in a maximum drift time of 150 ns. The average resolution perpendicular to the sense wire is about 0.4 mm using one tube and 0.3 mm using one plane of tubes.

3.6 Data Acquisition and Trigger

Typical luminosities during DØ's first run (1A) were 5×10^{30} $cm^{-2}s^{-1}$. At a center of mass energy of 1.8 TeV the minimum bias cross section is approximately 43 mb. The rate of hard scatterings is dependent on luminosity (*e.g.,* 210 kHz for $\mathcal{L}=5\times10^{30}$ $cm^{-2}s^{-1}$), and has as an upper limit the beam crossing rate of 280 kHz. Only a very small portion of this rate contains events of interest, therefore DØ has a multilevel trigger system which is divided into four levels of increasingly sophisticated event characterization. The Level 0 scintillator based trigger indicates the occurrence of an inelastic scatter, and has an output rate close to that of the rate of hard scatterings. Levels 1 and 1.5 are a collection of hardware trigger elements arranged in a flexible software driven architecture. Whereas the Level 1 operates within the 3.5 μs time interval between beam crossings and thus contributes no deadtime, the Level 1.5 trigger elements require multiple bunch crossings to complete more restrictive decisions. The rate of successful Level 1 triggers is about 200 Hz; after action by the Level 1.5 triggers, the rate is reduced to below 100 Hz. Candidates from the Level 1 (and 1.5) are passed on the standard DØ data acquisition pathways to a farm of microprocessors which serve as event builders as well as the Level 2 trigger system. Sophisticated algorithms involving event reconstruction reside in the Level 2 processors which reduce the rate to

about 2 Hz. The events can then be passed on to the host computer for event monitoring and recording to permanent storage media. The DØ data acquisition and trigger system are discussed in great detail in [3.4] and [3.15].

3.6.1 Level 0 Trigger

The Level 0 trigger[3.16] registers the presence of inelastic collisions and serves as the luminosity monitor for the experiment. The device consists of two hodoscopes of scintillation counters mounted on the front surfaces of the end calorimeters. These hodoscopes have a checker board like pattern of square and rectangular scintillation elements inscribed in a radius of 45 cm which surround and are perpendicular to the beam. The hodoscopes have partial coverage in the rapidity range $1.9 < \eta < 4.3$ and almost full coverage in the range $2.3 < \eta < 3.9$. This rapidity coverage is set by the requirement that a coincidence of both Level 0 detectors be ≥99% efficient in detecting non–diffractive inelastic collisions.

In addition to identifying inelastic collisions the Level 0 trigger provides information on the *z*-coordinate of the primary collision vertex. The *z*-coordinate is determined by the difference in arrival time from the two ends. For single interactions (one hard scatter per beam crossing) the resolution on this measurement is ±3.5 cm, for multiple interactions the resolution is ±6.0 cm.

3.6.2 Level 1 and 1.5 Triggers

The Level 1 trigger is an assembly of hardware trigger elements in a flexible software controlled framework. The Level 1 framework processes the digital signals from Level 0, the calorimeter hardware trigger element, the muon hardware trigger element, and timing signals from the accelerator and host computers. The selection of triggers is performed with a two-dimensional AND–OR network. An event is passed if it passes one or more of the 32 available *trigger bits*. Each of these bits is a logical combination of 256 programmable AND–OR *input terms*. Typical input terms include: number of muon candidates, amount of energy in a section of the calorimeter, Level 0 vertex position, and so forth. The Level 1 trigger incorporates no deadtime by making the decision within the 3.5 μs between beam crossings.

Calorimeter

The calorimeter hardware trigger element supplies digital information, based on analog information from the first stage of the calorimeter electronics, to the framework within the allotted 3.5 μs. These analog signals are read out in terms of *trigger towers* with flash ADC's. A trigger tower is the energy in the cells in a region given by $\Delta\eta \times \Delta\varphi = 0.2 \times 0.2$ for all EM depths, or all hadronic depths. These towers, associated with an energy threshold, can be used as an input term. The towers are also summed to make input terms of global quantities such as $\not{E}_T$, or global sum E_T.

Muon

The muon system has a Level 1 and a Level 1.5 component [3.15]. Digital information based on one latch bit for each of the 16,700 drift cells is supplied to both. These latch bits correspond to the bend coordinate of hit drift cells. Using the latch bits, a search in 60 cm wide roads is used to find candidate muons.

Level 1 muon information consists of the number of muon candidates found and the region they were located in; CF, EF-north, EF-south, SAMUS-north or SAMUS-south. For WAMUS muons, the trigger requires at least two hit drift cells in all three layers of chambers, except near the CF–EF boundary (roughly $0.8 \leq |\eta| \leq 1.0$) where some 2 layer combinations are allowed to increase muon acceptance in this region of two chamber coverage. A minimum of two hits is required within each layer and additionally the minimum two hits must be from different decks within each layer. Note

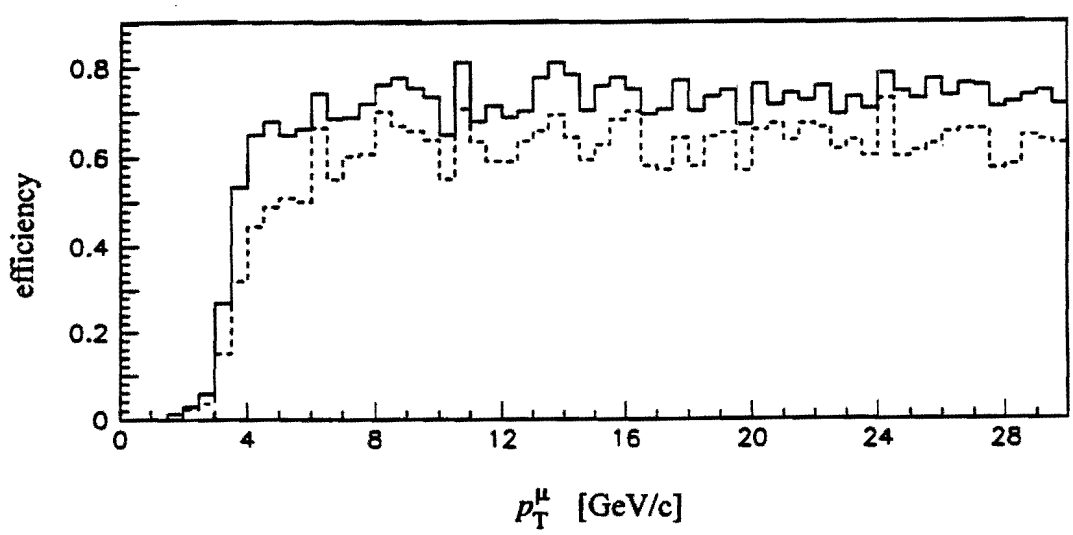

Figure 3.20 Muon Level 1 acceptance and efficiency vs. muon p_T for the CF region. Geometrical acceptance (solid line), geometrical acceptance + efficiency (dashed line).

that there is no p_T cut available at muon Level 1, however, the requirement that there be hits in all three layers imposes an implicit momentum cut of ~3–5 GeV/c associated with the muons ability to penetrate the calorimeters and muon toroids. Single muon efficiency in the CF has no significant η dependence and is roughly 65% for muons with p_T above 8 GeV/c (see Fig. 3.20) [3.17].

The Level 1.5 provides a more precise location of the muon and an estimate of the muon p_T, from localizing the track in a chamber to 5 cm granularity. Use of the Level 1.5 does incur some deadtime as well as loss in acceptance. It is primarily used in triggering on W decays to muons and is not used for this analysis.

3.6.3 Level 2 Filter and Event Builder

The Level 2 filter is a 50 node microprocessor farm (VAX 4000–60's for the 1992–93 collider run). If at least one Level 1 trigger is satisfied, the full detector is read out for which all the data for the specific event is sent over parallel paths to memory modules in a selected node (one of the 50). The event data is then collected and formatted in final form in the node, and the Level 2 filter algorithms are applied.

At this point certain aspects of the event are reconstructed with code that is a simplified subset of that used offline. With the reconstructed quantities available the event is subjected to the Level 2 filter algorithms. These algorithms are composed of filter tools, where each tool has a specific function related to the identification of a type of particle or event characteristic. Among the tools are those for jets, muons, calorimeter EM clusters, track association with calorimeter clusters, ΣE_T and $\not{E}_T$. Other tools recognize specific noise or background conditions. The tools are organized in particular

combinations in the form of *scripts*; a specific script is associated with each of the 32 Level 1 trigger bits. The script spawns Level 2 filter tools from the satisfied Level 1 bits; for example, a single muon trigger from Level 1 might be given to different Level 2 bits (comprised of one or more tools) depending upon the p_T threshold or other features of the event (*e.g.*, requiring a jet or the presence of $\not{E}_T$). The Level 2 filter will support up to a total of 128 configurations for a total of 128 different Level 2 triggers.

CHAPTER 4

TRIGGER, EVENT RECONSTRUCTION, AND PARTICLE IDENTIFICATION

4.1 Criteria and Method

Selection criteria are imposed on the data in three stages; data collection, event reconstruction and final event selection. The following sections discuss each of these steps and the criteria leading to the final event selection.

The initial set of selection cuts are made during online triggering. This is optimized to obtain the greatest acceptance for the signal sought, in parallel with limiting the event rate from background processes to the extent that the total data-taking rate is acceptable. At this point the selection criteria are rather crude, and only the loosest possible requirements applied.

Next, the raw data are reconstructed to identify physics objects such as charged particle tracks and showers of energy in the calorimeter. Reconstruction uses a detailed description of the detector geometry and calibration constants, in combination with specific reconstruction algorithms to obtain a list of particles produced in the collision together with their momenta and directions. The reconstruction algorithms have built in quality requirements and thresholds. They emphasize high efficiency and make initial assignments of particle identification based on loose cuts.

Lastly the reconstructed data are processed through a specific analysis selection algorithm which searches for the particle types and topologies of interest. At this stage,

tighter and more specific definitions of the physics objects are applied and a final data sample is obtained. Since the final result of searching for $t\bar{t} \rightarrow \mu\mu$ is critically sensitive to the criteria used for selecting muons, jets and $\not{E}_T$, these definitions must be chosen with great care. This same selection criteria is applied to both data and Monte Carlo to determine optimal signal efficiency and signal to background ratio.

The criteria and algorithms used for the $t\bar{t} \rightarrow \mu\mu$ analysis at each of the three selection stages are described in the following sections.

4.2 Triggering

A description of the trigger system is given in section 3.6. Here we focus on the specific trigger requirements used for this analysis. The top search in the dimuon channel required one trigger at Level 1, no Level 1.5 trigger, and one set of trigger conditions at Level 2. These trigger cuts are listed in Table 4.1. The following

Level 1		
	≥ 1 muon:	$\lvert\eta_\mu\rvert \leq 1.7$
	≥ 1 trigger tower:	$E_T^{jet} \geq 5$ GeV
Level 2		
	≥ 1 muon:	$\lvert\eta_\mu\rvert \leq 1.7$
		$P_T^\mu \geq 14$ GeV
		Cosmic Ray rejection
	≥ 1 jet:	$E_T^{jet} \geq 15$ GeV
		Cone size: $\Delta R = 0.7$

Table 4.1 Level 1 and Level 2 triggers for $t\bar{t} \rightarrow \mu\mu + X$

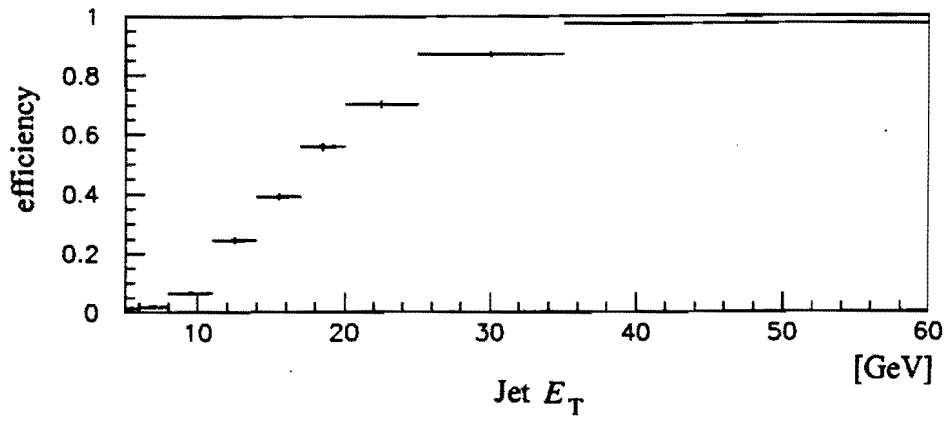

Figure 4.1 Jet trigger efficiency vs. jet E_T for a 5 GeV trigger tower threshold.

requirements are based on studies of signal efficiencies using Monte Carlo events, and data taken during special runs dedicated to the study of trigger efficiency.

4.2.1 Level 1

At Level 1 the requirements were at least one muon with rapidity, $|\eta_\mu| \leq 1.7$ (i.e., within WAMUS coverage) and at least one trigger tower with transverse energy, $E_T^{jet} \geq 5$ GeV, where a trigger tower is a region of the calorimeter given by $\Delta\eta \times \Delta\varphi = 0.2 \times 0.2$ (see section 4.3.2). The cross section for events passing this Level 1 trigger is approximately 1.1 μb out of the total minimum bias cross section of ~42 mb.

The Z^0 dimuon trigger is not used for this analysis, it would be very inefficient for $t\bar{t} \rightarrow \mu\mu$, since this trigger uses the muon Level 1.5 which has less acceptance than muon Level 1. In addition, the muon Level 1 trigger has acceptance of roughly 65% for

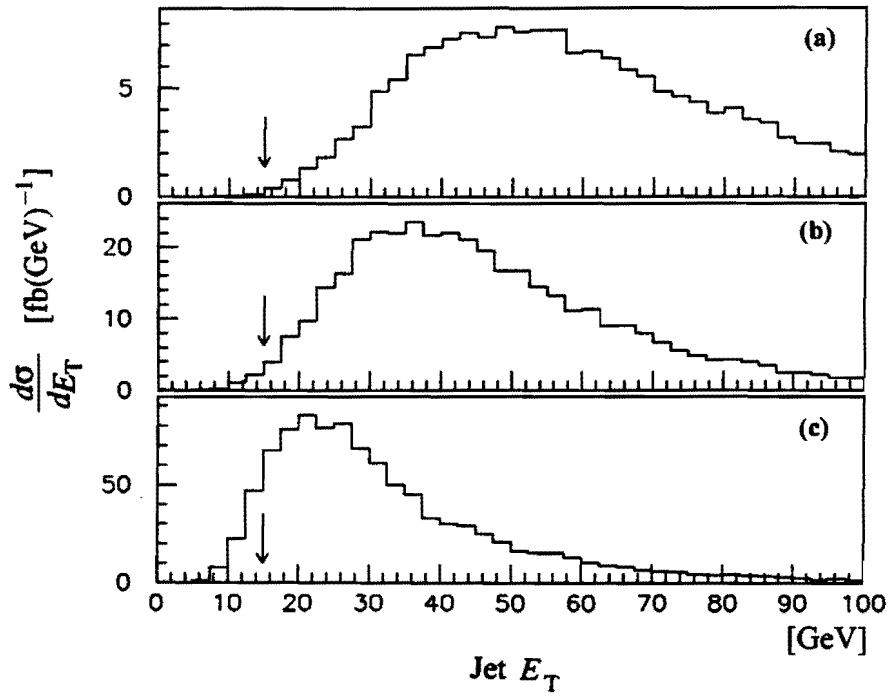

Figure 4.2 Highest E_T jet in ISAJET $t\bar{t} \rightarrow \mu\mu$ for top masses of: **(a)** 140, **(b)** 120 and **(c)** 100 GeV/c^2. Arrows indicate threshold set in Level 2. Note that the Level 1 trigger is only fully efficient for jets with E_T above 30 GeV (Fig. 4.1).

muons with p_T above 8 GeV/c (see Sec 3.6.2), and would be inefficient for $t\bar{t} \rightarrow \mu\mu$ if two muons were required at Level 1.

To bring the bandwidth to acceptable level while retaining acceptance, a jet is required in the event to mark the presence of one of the b quark jets expected in the $t\bar{t}$ decay. However the jet trigger requirement of one trigger tower above 5 GeV only becomes fully efficient for jets with E_T greater then 30 GeV (Fig. 4.1) and is a source of inefficiency. The efficiency curve in Fig. 4.1 was obtained by taking the ratio of muon triggers to that of muon + jet triggers in the DØ b-physics single muon data sample. The efficiency for this trigger increases with increasing top mass as the b quark jets become harder in E_T (see Fig 4.2) and is optimized for top masses above 140 GeV/c^2.

Further constraints are imposed at Level 1 to remove some of the backgrounds associated with parallel collider and Main Ring operation. These included a short veto of ±0.8 μs (centered on the $\bar{p}p$ crossing time) when Main Ring proton bunches are passing the DØ collision point (which incurs ~8 % deadtime), and a longer veto of ~0.1–0.5 s during Main Ring injection and transition when proton losses are largest (giving roughly 17 % deadtime). At these times main ring activity causes noise in the upper portion of the muon system and calorimeters and renders them inefficient for triggering [4.1]. The dead time produced by this veto mostly effects analyses involving muons, and the veto's effect on the integrated luminosity used in this analysis is considered in Sec. 6.1.

4.2.2 Level 2

In Level 2, the trigger requirements are in the form of software algorithms, which are a simplified subset of those used in the off-line reconstruction. For this analysis the Level 2 trigger required at least one muon in the region $|\eta_\mu| \leq 1.7$ with transverse momentum $P_T^\mu \geq 14$ GeV and one or more jets with transverse energy $E_T^{jet} \geq 15$ GeV. At Level 2, jets are defined using a cone algorithm with $\Delta R = 0.7$, and the muons are required to pass the cosmic ray cuts described in Sec. 4.3.3. The momentum of the muon is calculated from the muon system and Level 1 vertex information only, so that the trigger threshold is not a sharp cut in p_T^μ. With this in mind Figures 4.2 and 4.3 show the placement of thresholds on jet E_T and muon p_T respectively on $t\bar{t} \rightarrow \mu\mu$ Monte Carlo distributions for three values of top mass.

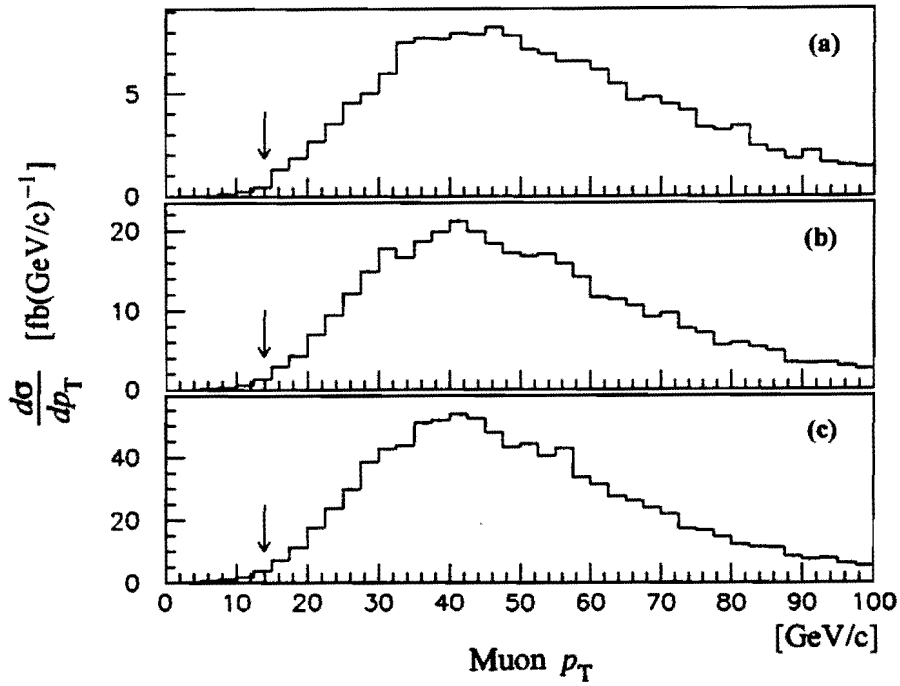

Figure 4.3 Highest p_T muon in ISAJET $t\bar{t} \rightarrow \mu\mu$ for top masses of: **(a)** 140, **(b)** 120 and **(c)** 100 GeV/c^2. Arrows indicate threshold set in Level 2. Note that the Level 1 muon trigger has an acceptance of roughly 65% for p_T above 8 GeV/c (see Fig 3.20).

The cross section for events passing this Level 2 filter was measured to be roughly 5 nb out of the 1.1 μb from the Level 1 muon + jet trigger. All events passing these Level 2 filter requirements were written to tape.

4.3 Event Reconstruction

The raw data from the detector is in the form of digitized quantities such as pulse heights, integrated time signals, scalar counts and flag bits. The reconstruction program interprets these using *a priori* information about the detector (*e.g.*, surveys and calibrations) to build a representation of the event in terms of kinematic quantities of

physical objects (*e.g.*, particles and jets). The task of performing the reconstruction is done offline using a 'farm' of processors in parallel. The algorithms used are contained in the software package DØRECO [4.2] which is composed of ~ 150,000 lines of FORTRAN code (less utility libraries), and has been developed over the course of several years by the DØ collaboration.

The output of DØRECO is in two forms: STA and DST files. STA files contain the raw data plus the output from the reconstruction. These files typically contain more than 800 kbytes per event and thus are impractical to use as the primary means of access to the data. The STA files are needed for displaying events and for reprocessing the data through alternate or newer versions of DØRECO. DST files contain a condensed version of the information in an STA, and are typically 20 kbytes per event. They contain descriptions of all reconstructed objects and their associated kinematic quantities.

The output of DØRECO is the starting point for all analyses done using DØ data. Thus initial particle assignments and calculations of kinematic quantities are based on relatively loose criteria to accommodate analyses with differing concerns. To permit standardization of particle identification algorithms used among the different analysis groups, DØRECO provides many quality flags pertaining to the options used during the reconstruction and conditions encountered in the raw data.

4.3.1 Vertex Reconstruction

The point of collision of the p and $\overline{p}$, referred to as the primary vertex, is important in the reconstruction of the four-vectors of the particles produced. Its position

in the r–ϕ plane is approximately constant during data taking and is reconstructed offline using the VTX chamber.

Because of the finite length of the proton and antiproton bunches in the Tevatron, collisions occur over an extended z–interval. The resulting primary interaction region has an approximately Gaussian distribution in z, with a width of about 30 cm centered on $z = -7$ cm. The z position is found for each event separately by performing a three dimensional tracking reconstruction in the CDC or FDC. A Gaussian fit is then applied to the intersection of these tracks with beam position in r–ϕ (as determined above) to find the collision vertex in z. The mean is taken as the z–position, and the width of the distribution is taken as the error. This defines the vertex position to an accuracy of approximately $\pm$ 700 μm in z, and 180 μm in r–ϕ.

4.3.2 Jet Reconstruction

A jet is the resulting collection of particles produced in the fragmentation of a final state parton produced in a hard interaction. This shower of collimated particles deposits energy in various cells of the calorimeter, and it is the challenge to the ingenuity of the calorimeter reconstruction software to infer the momentum of the parton from the pattern of deposited energy.

DØRECO uses several jet finding algorithms based on various cone sizes. For this analysis, a $\Delta R = 0.7$ cone algorithm was used. This looks for energy deposited in regions of η–ϕ space defined by $\Delta R = \sqrt{\Delta\eta^2 + \Delta\phi^2} = 0.7$. The algorithm uses information from the calorimeter in the form of *jet towers* which are considered in order of decreasing E_T. Here a jet tower is defined as an energy sum over all calorimeter layers in a solid angle 0.1×0.1 in η and ϕ (a stack of single cells), pointing at the

nominal vertex with a minimum threshold requirement of $E_T > 1$ GeV. Jet towers are grouped into *preclusters* of contiguous cells in a cone of $\Delta R = 0.3$. The center in η–ϕ space of the preclusters serves as the starting point of the jets. The center axis of the jet is then recalculated as the E_T weighted centroid of all towers within $\Delta R = 0.7$. Starting with this new center the process is repeated several times until the jet is stable. Once a jet is found, DØRECO imposes as a final restriction a threshold of 8 GeV on the sum E_T within the $\Delta R = 0.7$ cone. The identification of objects in the calorimeter as jets becomes more difficult at lower jet E_T. Furthermore, the number of object identified as jets increases exponentially as the minimum E_T threshold is lowered. Thus the jet E_T cut off of 8 GeV is a chosen to limit the amount of CPU time in the reconstruction farm, and yet maximize the information given about the jets in the event [4.3].

Information about the jet is then calculated from the jet tower energies comprising the cone, such as the total energy, transverse energy, and the Cartesian components of the hit cells. Also calculated are various quality indicators useful in determining any problems for a given jet such as leakage out of the calorimeter and anomalous energy fluctuations in a cell. Examples of such quality indicators include the fraction of energy deposited in the electromagnetic calorimeter, the fraction of energy deposited in the last layer of the hadronic calorimeter, the fraction of energy deposited in the ICD if any, and the ratio of the highest energy cell in the jet to the next highest energy cell.

4.3.3 Muon Reconstruction

The muon reconstruction proceeds via three steps: hit sorting, track finding, and global fitting. The global fit, as its name implies, includes information from the full DØ detector, whereas the first two steps use only information from the muon system. Described below are the three steps of muon reconstruction, with an emphasis on the calculation of quality flags used later in the analysis.

Hit Sorting

This part of the reconstruction first performs integrity checks on the data, requiring as a minimum that a hit in the muon system have a pad-latch (*i.e.,* a bit set when the charge on the pads of a WAMUS PDT is above a set threshold, as used in the Level 1 trigger) and a physical drift time associated with it. The raw data is then used together with survey and electronic calibration constants to create space points in the DØ global coordinate system. Note that due to a left–right ambiguity in the drift cell there are two space points associated with each hit.

Track Finding

The next step is pattern recognition, in which a set of muon hits are assigned to a track. The left–right ambiguity is resolved at this stage as hits are fit to line segments, one segment in the A layer, and another segment from the combined B and C layer hits. The B–C segments require space points from a minimum of 4 planes out of 6, while A layer segments require a minimum of 2 planes out of 4.

A least squares fit is then performed to determine which points within a road constitute a final track and can be used to determine the muon momentum. This is done separately in the bend (rz plane, drift measured) and non-bend ($r\phi$ plane) views. In the non-bend view, a straight line is fit through the magnet and the track is constrained to originate from the vertex. In the bend view, the B–C layer hits are fit first and the resulting track segment is extrapolated into the midplane of the magnet. This establishes a pseudo-point in the middle of the magnet which is fit with the rest of the hits in the A layer. This gives the bend angle between the in going (A layer) segment and outgoing (B–C layer) segment and hence a preliminary estimate of the track momentum.

Track quality is expressed in terms of quality of fit in the bend and non-bend views, number of hits used on the track, the integral of $B \cdot dl$ (which gives an indication of how much magnetic field was traversed, and hence a statement on the accuracy of the momentum calculation) and the number of chambers on the track. Also at this point the muon track is extrapolated into the calorimeter, and the energy in the cells on its path and that in their nearest neighbors is summed. This quantity should be consistent with the minimum ionizing energy expected for a muon and is an important tool in the confirmation of muon identification.

Special cases arise when there are hits in only two layers, and the algorithm used is specific to the permutation of hit chambers; A with only a B or C layer, or a B–C segment with no A layer hits.

Global Muon Fit

The final momentum calculation supplements the information of the muon system with that of the vertex chamber and the central or forward drift chambers,

provided that a candidate for a matching track is found. The global fit is a 7 parameter least squares fit. Two parameters describe the position of the muon track before the calorimeter in each the bend view and non–bend view. Two parameters describe the bending angles of the muons in the calorimeter due to multiple scattering. The final parameter is the reciprocal of the muon momentum. Deflection of the muon in the calorimeter due to multiple scattering is accounted for in the calculation by considering two mean bend angles of zero with errors derived from a detailed Monte Carlo simulation. The errors in the central and forward drift chambers include errors from the track fitting as well as the inherent resolution of these detectors.

Cosmic Ray Rejection

Subroutines in DØRECO flag cosmic ray candidates in two ways at the track finding level. The muon system has a geometry of eight wedge shaped sections in ϕ. If a track crosses from one of the sections to another, it cannot be consistent with originating from the vertex and is flagged as a cosmic ray. The second method searches in a road opposite a found track in η and ϕ. The road size is chosen to match the expected deflection angle of the muon by multiple Coulomb scattering as the cosmic ray passes through the material of the detector. If a track or an A or B–C layer segment is found in this road, the track is then flagged as a possible cosmic ray.

Muon Momentum Resolution

Apart from chamber inefficiencies and effects of geometry from design constraints, the resolution of the muon momentum is limited by two main components, the resolution of the measured space points and the multiple Coulomb scattering

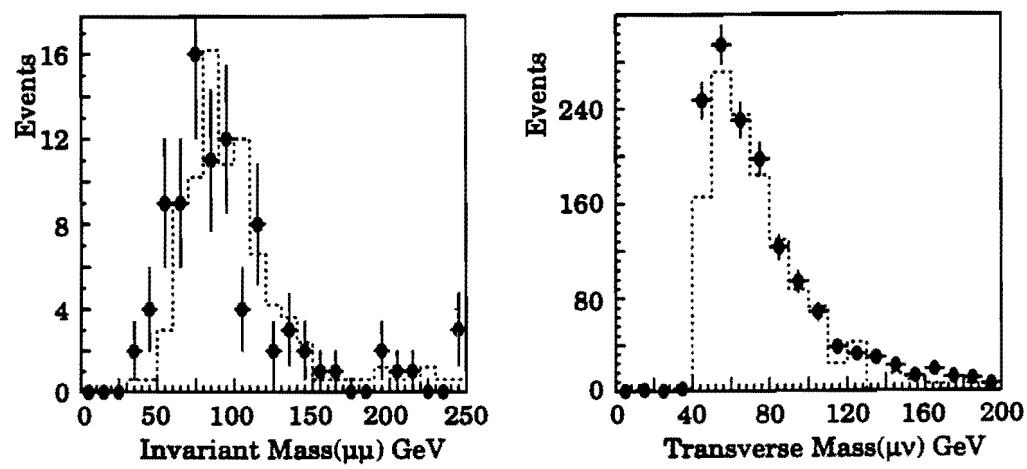

Figure 4.4 Comparison of tuned Monte Carlo(dashed line) to muon data(points).

produced by the iron toroid. At low momentum the resolution error is dominated by multiple Coulomb scattering, whereas at high momentum the main source is the resolution of the measured space points as the deflection angle in the magnetic field decreases and becomes harder to measure.

The resolution of the muon system is parametrized as

$$\left(\frac{\delta p}{p}\right)^2 = (0.18)^2 + (0.01p)^2.$$

Multiple Coulomb scattering in the iron toroids limits the relative momentum resolution to a minimum of 18 % and the drift resolution is approximately 0.2 mm. However, the current resolution on the chamber alignment is ~3 mm, giving rise to the less than optimum coefficient (1 %) in the second term of the parametrization. The resolution

quoted above is the result of comparing the Z^0 dimuon data with Monte Carlo, where the simulated events are tuned until the width and tails of the Z^0 mass peak are satisfactorily reproduced [4.4] . Fig. 4.4 shows a comparison of the tuned Monte Carlo to that of the muon Z^0 and W mass peaks and Fig. 4. 5 shows the same comparison for the transverse momentum and psuedorapidity distributions of muons from W decay. For typical tracks this leads to a momentum resolution of $\delta p/p = 0.21$ at 10 GeV/c, rising to 0.31 at 25 GeV/c.

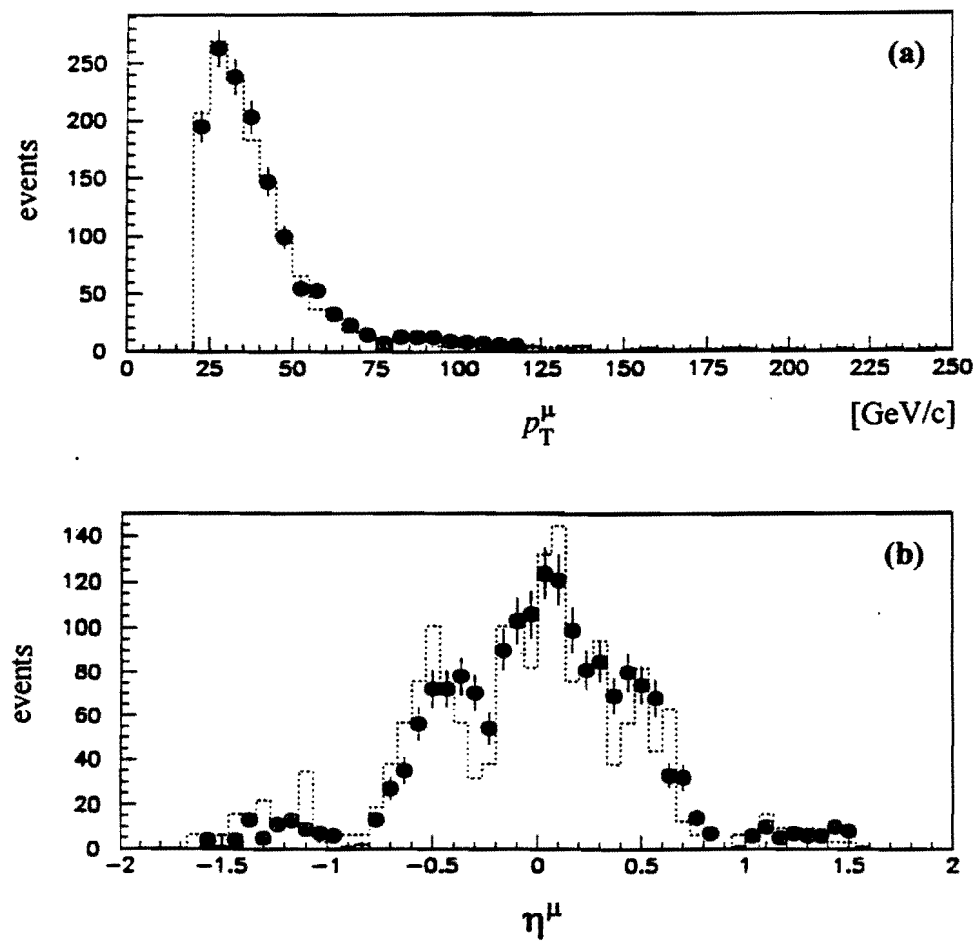

Figure 4.5 Comparison of tuned Monte Carlo (dashed line) to muon data (points) for **(a)** muon transverse momentum and **(b)** pseudorapidity for $W \rightarrow \mu\nu$.

4.3.4 Missing Transverse Energy Measurement

Neutrinos are not directly detectable at DØ. However, their presence can be inferred by the presence of energy imbalance when summing the momentum of all objects. Conservation of momentum implies that any deviation of this sum from zero can be interpreted as the consequence of one or more particles escaping the detector unmeasured. Since the longitudinal momenta of the initial partons is not known, and the forward components of the final state cannot be accurately measured (due to particles escaping down the beam pipe), one can reliably apply conservation of momentum only in the plane transverse to the beam.

Since calorimeters measure energy and not momentum, it is customary to refer to the nearly equivalent quantity, missing transverse energy ($\not{E}_T$). DØRECO calculates this in three ways; using the calorimeters only ($\not{E}_T^{cal-raw}$), using the calorimeters with corrections from the ICD and massless gap detectors ($\not{E}_T^{cal}$), and lastly to use $\not{E}_T^{cal}$ and correct it for the momentum of any muons observed in the event ($\not{E}_T$). The first two quantities are similarly defined as:

$$\not{E}_x^{cal} = -\sum_{i=1}^{n} E_i \sin\theta_i \cos\phi_i$$

$$\not{E}_y^{cal} = -\sum_{i=1}^{n} E_i \sin\theta_i \sin\phi_i$$

$$\not{E}_T^{cal} = \sqrt{(\not{E}_x^{cal})^2 + (\not{E}_y^{cal})^2}$$

where i runs over all cells in the calorimeter, E_i is the energy deposited in cell i, and θ_i and ϕ_i are the polar and azimuthal angles of the center of cell i. In this case $\not{E}_T^{cal}$ is calculated, thus the cells of the ICD and massless gap detectors are included in the summed cells.

For the muon corrected missing transverse energy, the momenta of all the muons are added vectorially to the above sum, while the expected muon energy deposition (estimated from detector Monte Carlo) in the calorimeter must be subtracted since it is included in the calorimeter sum. Hence the muon corrected $\not{E}_T$ becomes:

$$\not{E}_x = \not{E}_x^{cal} - \sum_{\mu}(p^{\mu} - E^{dep})\sin\theta_{\mu}\cos\phi_{\mu}$$

$$\not{E}_y = \not{E}_y^{cal} - \sum_{\mu}(p^{\mu} - E^{dep})\sin\theta_{\mu}\sin\phi_{\mu}$$

$$\not{E}_T = \sqrt{(\not{E}_x)^2 + (\not{E}_y)^2}$$

where p^{μ}, E^{dep}, θ_{μ}, and ϕ_{μ} are the muon momentum, expected muon calorimeter deposition, and muon polar and azimuthal angles, respectively.

The $\not{E}_T$ resolution of the DØ calorimeter has been parametrized (Fig. 4.6) as:

$$\sigma_{\not{E}_T} = a + b \cdot S_T + c \cdot S_T^2$$

with $a = (1.89 \pm 0.05)$ GeV, $b = (6.7 \pm 0.7) \times 10^{-3}$, $c = (9.9 \pm 2.1) \times 10^{-6}$ GeV^{-1}, and where S_T is the scalar sum of the transverse energy in the calorimeter. This parametrization is based on QCD dijet data [4.5] .

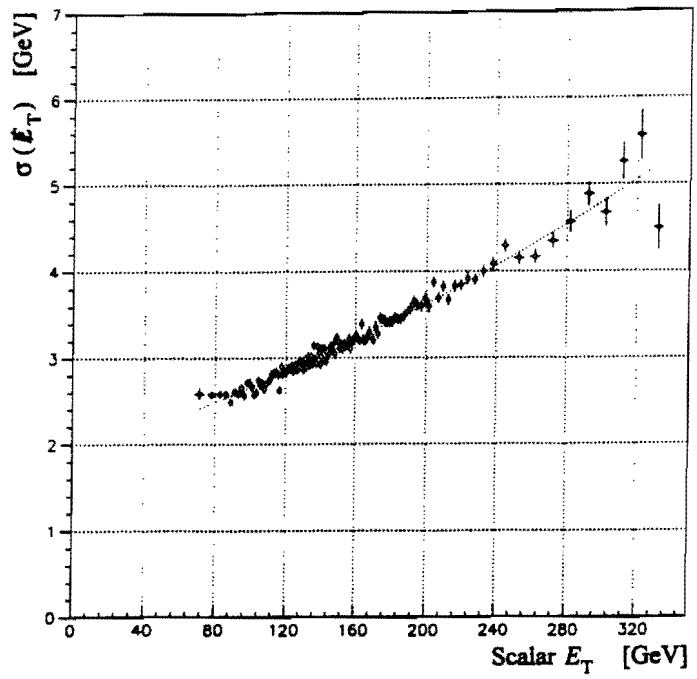

Figure 4.6 Resolution of $\not{E}_T^{cal}$ as a function of sum scalar E_T.

4.4 Event Selection

Event selection and studies of background processes are performed using a DØ package called TOP–LEPTONS. This can read DST or STA files and operates on both data and Monte Carlo events. The controls and selection cut settings for TOP–LEPTONS are in the form of ASCII files known as RCP (Run Control Parameter) files. Such files are common in the DØ software environment, and have the advantage that a program need not be recompiled or relinked each time a switch or threshold is changed.

TOP–LEPTONS does more than just filter the reconstructed data. It also controls routines which augment the object definitions from DØRECO, applies corrections to those objects based on studies of the data, and provides means of viewing

the data using histograms, and text in the form of event dumps. The following sections outline the method of deriving the final objects of interest; muons, jets and $\not{E}_T$, and the final selection criteria applied to them.

4.4.1 Muon Selection

The first step in the final analysis of muon tracks is to apply further rejection criteria to any remaining cosmic rays. TOP–LEPTONS does this using the flag bits set in DØRECO (see Sec. 4.3.3) to reject tracks that cross octant boundaries, and to reject those that have another track or segment on the opposite side (in η and ϕ) of the detector.

The next selection criteria deal with quality of the reconstructed muon track. The first of these requires that the least squares straight line fit for all the track segments have good χ^2. This implies that the tracks are consistent with the reconstructed vertex in both the bend and non-bend views.

Other requirements deal with track verification using the calorimeter and CD. Confirmation from the calorimeter requires associated energy deposition consistent with that of a 1 mip track. Confirmation from the CD consists of matching at least one track from the CDC or FDC to the muon track. Numerically these cuts correspond to:

- For muon tracks with a matching track in the CD:

  calorimeter muon energy deposition ≥ 0.5 GeV

- For muon tracks with no matching CD track:

  calorimeter muon energy deposition ≥ 1.5 GeV

The second of these requirements increases the muon acceptance by including tracks that pass through the transition region between the CDC and FDC, and tracks which do not have a match due to inefficiency in the tracking chambers. For these special cases the energy threshold is increased to reject against residual cosmic ray contamination and combinatoric fake muon tracks.

Lastly, only muons in the fiducial region $|\eta| \leq 1.1$ are included in this analysis. The background from accidental combinations of noise hits producing tracks in the forward regions of the muon detector is formidable, and muon selection quality criteria become more difficult to define, leading to large uncertainties in the trigger and reconstruction efficiencies. The efficiency of the EF muon chambers is currently under study but are excluded from this analysis.

4.4.2 Jet Selection

In the early and only available version of DØRECO used for this analysis, only a preliminary version of the detector energy calibration was included. Subsequent studies have led to calibrations for the absolute jet energy scale and corrections for losses in the jet finding algorithms. These are applied to reconstructed jets by TOP–LEPTONS prior to jet selection. The energy scale corrections have been determined from studies of E_T balance using the preliminary DØ direct photon event sample. In such events a photon is back to back in η–ϕ with a jet. Under the assumption that the $\not{E}_T \approx 0$, and that the electromagnetic energy response is correctly calibrated, the measured $\not{E}_T$ is taken to be due to the incorrect response of the calorimeter to the jet compared with its response to the photon. That is, the difference between the measured energy of the jet (E_T^{jet}) and its

true energy (E_T^{true}) is equal to the component of the $\not{E}_T$ vector in the direction of the jet ($\hat{n}_T^{jet}$),

$$\vec{\not{E}}_T \cdot \hat{n}_T^{jet} = E_T^{true} - E_T^{jet}.$$

The correction factor (f^c) which is used to convert from measured jet energy to corrected jet energy is defined by $E_T^{true} \equiv f^c \cdot E_T^{jet}$. Therefore,

$$f^c = 1 + \frac{\vec{\not{E}}_T \cdot \hat{n}_T^{jet}}{E_T^{jet}} = 1 + \mathrm{MPF}(\eta, E_T^{jet})$$

where MPF is known as the missing E_T projection fraction. These correction factors are a function of pseudorapidity and jet E_T (Fig. 4.7). This technique was first developed by

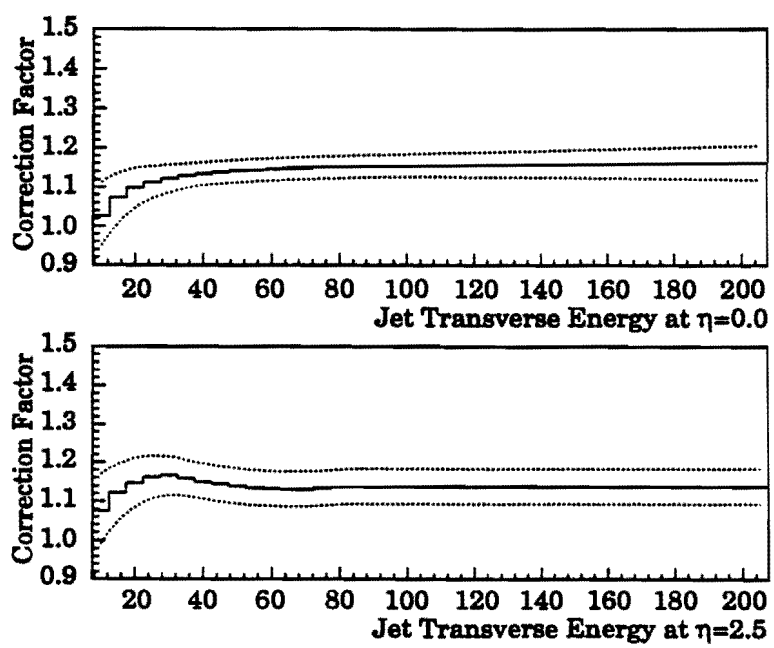

Figure 4.7 Jet energy correction factor for $\Delta R = 0.7$ cone jets at $|\eta| = 0.0$ and $|\eta| = 2.5$. Dashed curves show the upper and lower response from test beam and Monte Carlo calibrations.

the CDF collaboration [4.6] and its application in DØ is discussed in detail elsewhere [4.7].

The electromagnetic energy scale used in DØRECO is also corrected in TOP–LEPTONS. Here the correction was determined by scaling the reconstructed energy of the EM clusters to make the observed Z^0 mass peak in the dielectron data agree with the LEP value [4.8].

Additional (smaller) corrections for zero suppression, jet out of cone leakage, and underlying event effects are also applied in TOP–LEPTONS. Finally, a minimum E_T threshold of 8 GeV is required for all corrected jets.

4.4.3 Missing Transverse Energy Considerations

After jets and EM clusters have been corrected, the calorimeter missing E_T ($\not{E}_T^{cal}$) is recalculated. The muon corrected missing E_T ($\not{E}_T$) is recalculated similarly, using only the muons that pass the TOP–LEPTONS selection criteria.

CHAPTER 5
EVENT SIMULATION

5.1 Monte Carlo Methods

The term Monte Carlo refers to any random number based simulation. In the field of High Energy Physics, Monte Carlo techniques are usually applied in two main areas; simulation of the particle interaction in the collision, and simulating the response of the detector to the resulting particles. The complexity of the physics at 2 TeV (hundreds of particles per event) and the sophistication of the experimental apparatus (over 100k readout channels and 2000 person years) demand a collaborative effort to produce such simulations. The simulation programs are the products of many contributors and have been developed over several years. An outline of how these simulations are structured is given below. Further details may be found in the user guides and published documentation of the code and are cited as references.

5.1.1 Event Generators

In high energy applications, Monte Carlo techniques are usually attempts at direct simulation of physical processes. For a quantity of interest, $\bar{f}$, such as a cross section or decay width, multiple integrations arise due to final phase space and other continuous variables such as momentum fractions of incident partons and fragmentation products. The integrand f will include theoretical cross sections as well as kinematic

and geometric restrictions. Mathematically $\bar{f}$ is an integral of a weight function $f(x_1 \ldots x_n)$ over variables $x_1 \ldots x_n$ that parametrize the possible physical configurations. Monte Carlo methods calculate this integral by generating a random sample of configurations and averaging the integrand [5.1].

For hadron-hadron collisions, the most commonly used event generators are ISAJET[5.2], PYTHIA[5.3] and HERWIG[5.4]. Each generator follows the same four basic steps [5.5]:

Hard Scattering

First the contribution to the $\bar{p}p$ cross section is calculated. This calculation is based on first order (Born) Feynman diagrams for simple two body scattering, $\hat{\sigma}_{ij\to k}$, through the convolution integral

$$\sigma_{ij\to k} = \int dx_1 \int dx_2 f_i^1(x_1, Q^2) f_j^2(x_2, Q^2) \hat{\sigma}_{ij\to k}$$

where $x_i = p_i/p$ is the momentum fraction of parton i, Q^2 is the momentum transfer, and $f_i^1(x_k, Q^2)$ and $f_j^2(x_k, Q^2)$ are the structure functions for the proton and antiproton respectively.

QCD Evolution

The partons which participate in the hard scatter are then evolved through repeated parton branchings. The probability P that a branching $a \to bc$ will take place during a small change in the evolution parameter dt ($t = \ln\left(Q^2/\Lambda^2\right)$) is given by the Altarelli-Parisi equations [5.6]

$$\frac{dP}{dt} = \int dz \frac{\alpha_s(Q^2)}{2\pi} P_{a\to bc}(z)$$

where $P_{a\to bc}(z)$ are known as the splitting functions, z is the energy fraction, and $\alpha_s(Q^2)$ is the strong coupling constant (typically evaluated to first order). The process starts with the maximum allowed mass for parton a and t is then successively degraded until a branching occurs. The products, b and c, are then allowed to branch and so on, until the branching process is stopped when a parton mass has evolved below an applied minimum threshold (*i.e.*, $t < t_{\min} = \ln\left(Q^2_{\min}/\Lambda^2\right)$). This procedure is used to generate both initial and final state radiation.

Hadronization

The quarks and gluons which emerge from the QCD evolution cannot continue in color singlet states. An attribute of QCD known as color confinement allows only colorless states, thus virtual quarks and gluons are pulled from the vacuum (heeding conservation of quantum numbers; color, charge, etc.) to bind with the original partons and form hadrons. This is the process of fragmentation [5.7] or hadronization and is not calculable in pertubative QCD.

Event generators must rely on an empirical scheme to model the transformation of the final state partons into experimentally observed particles. With the exception of the Lund string fragmentation used in PYTHIA, most event generators use the Feynman-Field fragmentation scheme [5.8]. In this scheme the fragmenting quark is combined with an antiquark from a $q\bar{q}$ pair pulled from the vacuum to produce a hadron with energy fraction z. The remaining quark, with energy $(1-z)$, is then fragmented in the same way, and this process is repeated until the energy of the leftover quark falls below some cutoff threshold. This scheme reproduces the limited transverse momenta and approximate scaling of energy fraction distributions found in quark jets. The scaling

arises from the energy independence of the assumed distribution for z, which is known as the fragmentation function $D(z)$. The fragmentation function used by ISAJET for heavy quarks is the Peterson *et. al.* parameterization (discussed in Sec. 2.3) with $\varepsilon_c = 0.30$ for charm, $\varepsilon_b = 0.02$ for bottom, and for top the Peterson variable is scaled according to $1/M_t^2$, leading to a very hard fragmentation function [5.9].

Beam Fragmentation

In collisions of hadrons, the partons that *do not* participate in the hard scattering form a signal in the detector which is collectively known as the underlying event. The mechanism by which these 'spectator' partons are to be evolved and hadronized is a source of some dispute among the various generators. In ISAJET the underlying event is modeled with two components, QCD radiation from the incoming partons and beam-jet fragmentation. The former is included in the branching process of the QCD evolution described above, the latter is simulated using a phenomenological model.

5.1.2 Detector Simulation: DØGEANT

A detailed simulation of detector response is essential in the design and development of sophisticated detectors like DØ. Later, during data analyses, this is critical to understanding detector acceptance, smearing, and other systematic effects which appear in the data. For detector simulation DØ uses a customized version 3.14 of the CERN program GEANT [5.10]. This program, known as DØGEANT, tracks particles through volumes containing user specified materials and performs precise modeling of interaction processes, such as; multiple Coulomb scattering, δ–ray production, decays,

muon and electron bremsstrahlung, and full electromagnetic and hadronic showering [5.11]. The results from all the above processes are then converted into the form of digitized signals which simulate the raw experimental data.

Using the GEANT framework to simulate a detector comes down to accurately coding the geometrical model through which the particles are tracked. DØ has removed the complexities of the geometry from the FORTRAN code (the standard) and placed them instead into ASCII files, known as Run Control Parameter (RCP) files, which permit much easier modification of the detector, and allows a tractable means of comparison and verification of the model description [5.12]. The package simulates the tracking and muon chambers in great detail, down to the level of sense wires, cathode material, support structures, etc. (cables, front-end electronics and their means of attachment are however not specified in detail).

Because of the large amount of CPU time required for a full simulation of showering in the uranium plates and argon gaps of the calorimeters (GEANT tracks the hundreds of secondaries through each specified volume), an approximation of the calorimeter is used. The full structure of the supports and individual modules is preserved but the contents of the calorimeter is modeled as homogenous blocks of uranium-G10-argon mixture (with correct average atomic weight). This greatly reduces the number of volumes and hence speeds up the tracking. Sampling fluctuations are added after showering for each track, and appropriate hadron to electron response, as determined from test beam, is introduced. The $\Delta\eta \times \Delta\phi \times \Delta z$ segmentation of the readout cells is then imposed and the compensated energies are added for each cell. Electromagnetic showers are allowed to evolve until the individual secondaries fall below 200 MeV at which point the energies are determined from simple parametrizations, saving a factor of 3 in computation time.

5.1.3 Further Refinements

The output of DØGEANT is not quite an accurate representation of the data. This is due to variables that could not be anticipated and properly modeled in the initial simulation, or to variables which vary significantly over short periods of time, and it is inefficient use of computer time to reprocess through the full simulator every time a better calibration is made, or each time survey constants are updated. This is especially true for the muon system where alignment plays a critical role in momentum determination, and the muon chamber drift tube efficiency is sensitive to its surrounding environment (*e.g.,* near the Main Ring when there is a flux of halo due to beam loss during the acceleration cycle).

For this analysis the response (efficiencies and resolutions) of the 164 WAMUS chambers is modeled independently of DØGEANT. This is done using a package called MU-SMEAR [5.13] which modifies the simulated muon data output from DØGEANT taking in to account variations due to:

- pad latch efficiency
- drift time signal efficiency
- drift distance resolution
- wire direction signal efficiency
- wire direction distance resolution
- chamber position resolution

using parametrizations derived from studies of cosmic ray and $Z^0 \rightarrow \mu^+\mu^-$ data.

5.1.4 Trigger Simulator

The signal efficiency for the $t\bar{t} \rightarrow \mu\mu$ is studied by using Monte Carlo data. An important part of which is the simulation of the trigger framework. This is done by using packages called L1SIM and L2SIM which simulate the response of the level 1 and level 2 trigger frameworks, respectively. L1SIM operates on either real or simulated data, and models the response of Level 1 trigger elements with an AND-OR network. The Level 2 software trigger simulator, L2SIM, involves only a transfer of code from the compact form used in Level 2 (VAXELN) logic to standard VMS. The input control and configuration files used in L2SIM are identical to those used during data taking [5.14].

5.2 Simulation of $t\bar{t} \rightarrow \mu\mu$+X Signal Events

To estimate the $t\bar{t} \rightarrow \mu\mu$ acceptance, event samples for five different top quark masses were generated using the ISAJET event generator. This was configured to force the decay of the W's produced from the top quark decays into muons. Samples of events each were generated in this way for top masses of 80, 100, 120, 140 and 160 GeV (see Table 5.1). The events were then processed through full detector simulation (DØGEANT), and event reconstruction (DØRECO). The resulting files were used in conjunction with the trigger simulators (L1SIM and L2SIM), and the analysis package (TOP–LEPTONS) to derive signal acceptances and efficiencies.

M_t (GeV/c^2)	Event generator	Detector Simulation	events in sample	Integrated Luminosity $\int \mathcal{L} dt$ (fb^{-1})
160	ISAJET	DØGEANT	2100	20.85
140	ISAJET	DØGEANT	700	3.35
120	ISAJET	DØGEANT	700	1.43
100	ISAJET	DØGEANT	700	0.56
80	ISAJET	DØGEANT	700	0.16

Table 5.1 Principal signal Monte Carlo event samples

In studying signal acceptance the contributions from the τ-decay modes:

$$t\bar{t} \rightarrow W^+bW^-\bar{b} \rightarrow \tau^+\tau^- + X \rightarrow \mu\mu + X \qquad \text{BF} \approx 0.04\%$$

and

$$t\bar{t} \rightarrow W^+bW^-\bar{b} \rightarrow \tau^\pm\mu^\mp + X \rightarrow \mu\mu + X \qquad \text{BF} \approx 0.44\%$$

have been neglected. In principle these processes add another 0.48 % to the total branching fraction into dimuon final states of 1.24+0.48=1.72 %. However, the momentum distribution of muons from the decay $W \rightarrow \tau$ is much broader than that from $W \rightarrow \mu$, and peaks at lower values of momentum. After imposing the trigger and offline p_T thresholds, the contribution from the tau decay modes is significantly decreased and results in a negligible signal. In principle there is also a contribution from the decays of b and lighter quarks. However, studies have shown that this is reduced to a negligible level by the isolation requirement imposed in the data analysis. The efficiencies quoted in later sections coming from these calculations neglect both contributions and so err on the conservative side.

Background process	Event generator	Detector simulation	events in sample	Integrated Luminosity $\int \mathcal{L} dt$ (pb^{-1})
$Z^0 \rightarrow \mu\mu$	ISAJET	DØGEANT	14000	110
$Z^0 \rightarrow \tau\tau \rightarrow \mu\mu$	ISAJET	DØGEANT	2300	513
$W^+W^- \rightarrow \mu\mu$	PYTHIA	DØGEANT	450	3600

Table 5.2 Principle background Monte Carlo event samples

5.3 Background Simulation

Monte Carlo event samples of the primary backgrounds to $t\bar{t} \rightarrow \mu\mu$ were generated using ISAJET and PYTHIA and subjected to full detector simulation and event reconstruction. These event samples (listed in Table 5.2) are used in conjunction with the Monte Carlo signal samples to study analysis cuts with respect to optimizing signal to background.

CHAPTER 6
FINAL EVENT SELECTION

6.1 Integrated Luminosity of the Data Sample

The dimuon search was performed on a sub-sample of the full DØ Run 1A data taken between December 12, 1992, and June 1, 1993. This excludes some of the initial data where the muon system was still undergoing calibration and shakedown, and the triggers were not optimized. In addition, data from any run with unrecoverable trigger or hardware problems has also been excluded, which leaves a net integrated luminosity of approximately 11.7 pb^{-1}.

Since the Main Ring passes through the upper portion of the DØ detector, special considerations are required for muon triggers when the Main Ring is in parallel operation with the Tevatron's colliding beams. The Main Ring is usually run in parallel with the Tevatron in the production of antiprotons for the ensuing collider store. For antiproton production, a single bunch of protons passes through DØ at the Main Ring cycle rate of 53 MHz. Losses from the Main Ring, as the proton bunch passes through the detector, result in a large flux of particles into the muon system. This leads to saturation of these chambers and renders them extremely inefficient. Because of the difficulty in correcting for these effects a veto is placed on events when the Main Ring proton bunch is present during the lifetime of the muon system ($\approx \pm 800$ ns centered on collider beam crossing). A correction factor is then applied to correct the integrated luminosity for the data loss. This is calculated by comparing the integrated luminosity of

a trigger containing this veto to that of a trigger without the veto. The triggers used to calculate this correction are those of the top search via the $e\mu$ channel: the muon-electron trigger which includes the veto, and the electron + jet trigger which does not (see ref. [6.1]). This leads to:

$$\frac{\int \mathcal{L}\,dt \text{ (muon + electron trigger)}}{\int \mathcal{L}\,dt \text{ (electron + jet trigger)}} = 0.940$$

and gives a final corrected integrated luminosity for this analysis of:

$$\int \mathcal{L}dt = 11.0 \pm 1.3 \text{ pb}^{-1},$$

where the standard DØ luminosity error of ±12% is assumed.

6.2 Data Selection

The analysis cuts for the top quark search through the dimuon decay channel are chosen with the particular strengths and weaknesses of the DØ muon system in mind. The very low level of punch-through background to muons (see Sec. 3.5), allows for very efficient muon isolation algorithms. On the other hand, the limit on muon momentum resolution (due to multiple Coulomb scattering in the iron toroids), makes cuts on quantities like dimuon invariant mass very inefficient. In spite of the momentum resolution, the DØ detector is powerful at identifying muons, and has overall excellent acceptance.

The principle background to the top search is the decay of Z^0 bosons to muon pairs. Because of the momentum resolution a simple cut on the invariant mass of the muon pair cannot be used for background rejection (as is done in the $t\bar{t} \rightarrow ee$ analysis [6.2], and in dilepton searches elsewhere [6.3]).

	Events in 11.0 pb^{-1}
1. Trigger + muon ID + 2nd muon 2 μ's: $p_T^{\mu} > 15$ GeV/c $\lvert\eta^{\mu}\rvert < 1.1$ 1 jet: $E_T^{jet} > 15$ GeV	29
2. Invariant mass cut $M_{\mu\mu} > 10$ GeV/c^2	19
3. Muon isolation $p_T^{rel} > 5$ GeV/c	11
4. Cosmic ray rejection $\Delta\phi(\vec{p}_T^{\mu_1}, \vec{p}_T^{\mu_2}) < 165°$ for $\Delta\eta(\vec{p}^{\mu_1}, \vec{p}^{\mu_2}) < 0.3$	11
5. Muon cleanup $\Delta\phi(\vec{\not{E}}_T, \vec{p}_T^{\mu_1})$ $< 165°$ for a 2 layer muon track $< 175°$ for a 3 layer muon track	9
6. $\not{E}_T$ validation $\Delta\phi(\vec{\not{E}}_T^{cal}, \vec{p}_T^{\mu\mu}) > 30°$	3
7. Dimuon opening angle; $\not{E}_T$ correlation cut $\Delta\phi(\vec{p}_T^{\mu_1}, \vec{p}_T^{\mu_2}) < 140°$ for $\not{E}_T < 40$ GeV	1
8. Second jet requirement 2nd jet: $E_T^{jet} > 15$ GeV	0

Table 6.1 Final analysis cuts and cumulative effect on data

The following analysis utilizes alternative methods developed to maximize the strengths of the detector, and the fact that a $Z^0 \rightarrow \mu\mu$ decay gives no intrinsic missing energy. These are summerized in Table 6.1, which also details their effects on the data sample. The following paragraphs discuss these cuts and outline the motivation behind each. Note that the Monte Carlo distributions shown throughout this chapter, unless otherwise stated, are generated with ISAJET, and subject to full detector simulation and event reconstruction (see Sections 5.2 and 5.3).

The initial selection, from the 11.0 pb^{-1} data sample in DST form, paralleled the trigger conditions (objects and thresholds) with the addition of the requirement of a second muon within the same pseudorapidity range. To obtain the greatest acceptance to top decay and allow for studies of trigger efficiency, no cut on trigger bits was required at the initial selection.

For each event thus selected the STA file was obtained, and the event was visually scanned using the DØ event display package. These events were then subjected to a second pass of the reconstruction using a tuned version of DØRECO which used the final detector calibration constants and a full implementation of muon global fitting and reconstruction. The selection bias introduced by this double reconstruction and selection was studied using a sample of electron-muon events from the $e\mu$ top search data sample [6.4]. A sample of $e\mu$ events selected with a muon p_T threshold of 5 GeV/c were re-reconstructed using the tuned version of the reconstruction program. The two data sets were then reselected, requiring a muon p_T threshold of 15 GeV/c for the pseudorapidity range $|\eta^\mu| < 1.1$. By comparing the two samples the bias in the selection efficiency was determined to be 0.98 ±0.05.

Trigger Selection and Initial Cuts

The initial analysis cuts parallel the trigger requirements (Sec. 4.1), using the reconstructed objects in their final form; *i.e.*, muons with full identification cuts and jets with full corrections applied. In addition, a minimum of two muons was required in each event to reflect the topology expected for $t\bar{t} \rightarrow \mu\mu$. Both muons are subject to satisfy the muon ID criteria discussed in Sec. 4.4.1: cosmic ray rejection, a matching track reconstructed in the central detector and/or a matching minimum ionizing trace in the calorimeter. A p_T threshold of 15 GeV/c is required on the two highest p_T muons in the event, and the leading jet in the event is required to have an E_T greater than 15 GeV to match that used in the Level 2 trigger. The choice of a 15 GeV/c threshold on the muon p_T is made primarily to reduce the background coming from b and c quark decays in QCD multijet events. The muons in the signal come from the decay of boosted W bosons for which the p_T spectra are much harder than those from b and c decay. These are compared in Figs. 6.1 and 6.2 which show the $p_T^{\mu_1}$, $p_T^{\mu_2}$ correlations for $b\bar{b}$, $c\bar{c} \rightarrow \mu\mu$ and $t\bar{t} \rightarrow \mu\mu$ for M_t=140 GeV/c^2, respectively. Both were calculated using the ISAJET Monte Carlo generator.

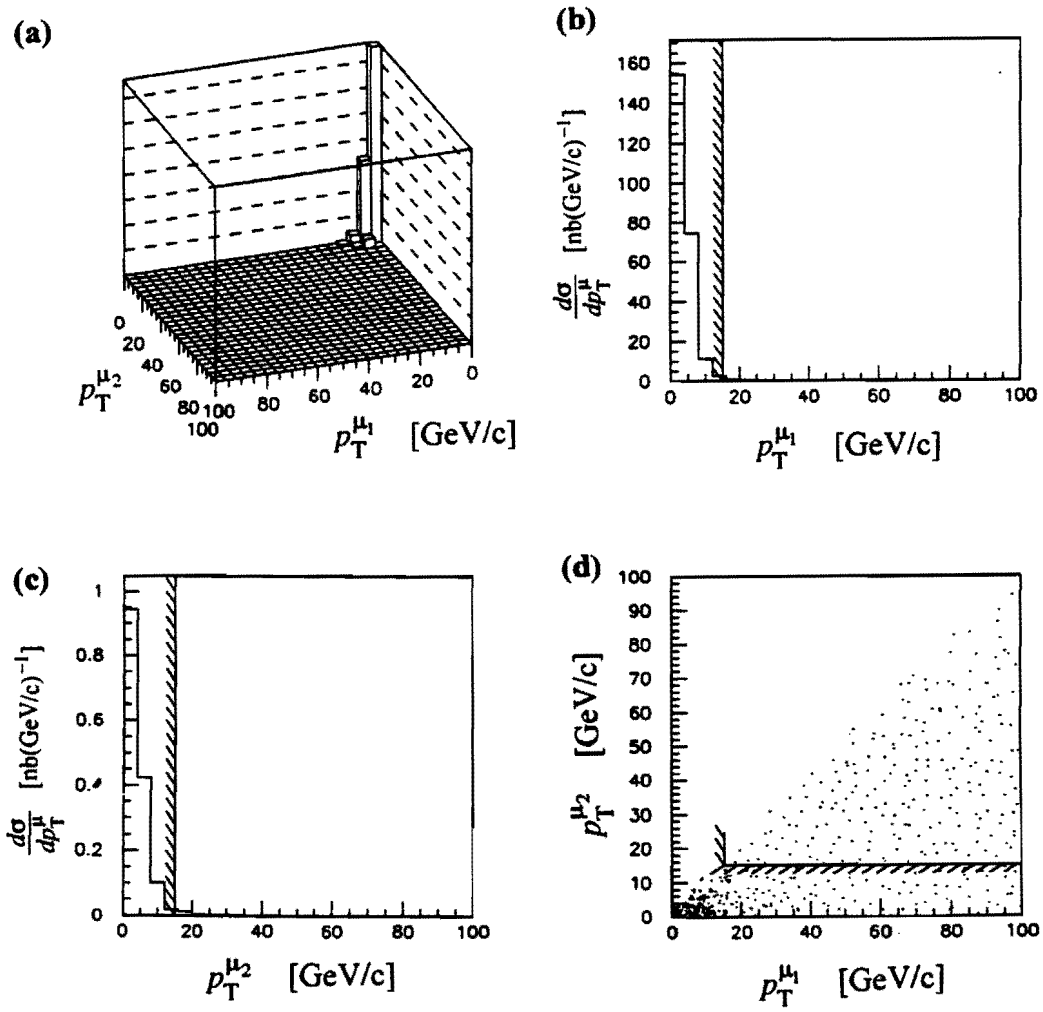

Figure 6.1 ISAJET $b\bar{b}$ and $c\bar{c} \rightarrow \mu\mu$.

(a) lego plot of $p_T^{\mu_1}$ vs. $p_T^{\mu_2}$ **(b)** $p_T^{\mu_1}$

(c) $p_T^{\mu_2}$ after cut: $p_T^{\mu_1}$>15 GeV/c **(d)** scatter plot of $p_T^{\mu_1}$ vs. $p_T^{\mu_2}$

Hatched lines show regions excluded by the muon p_T cuts.

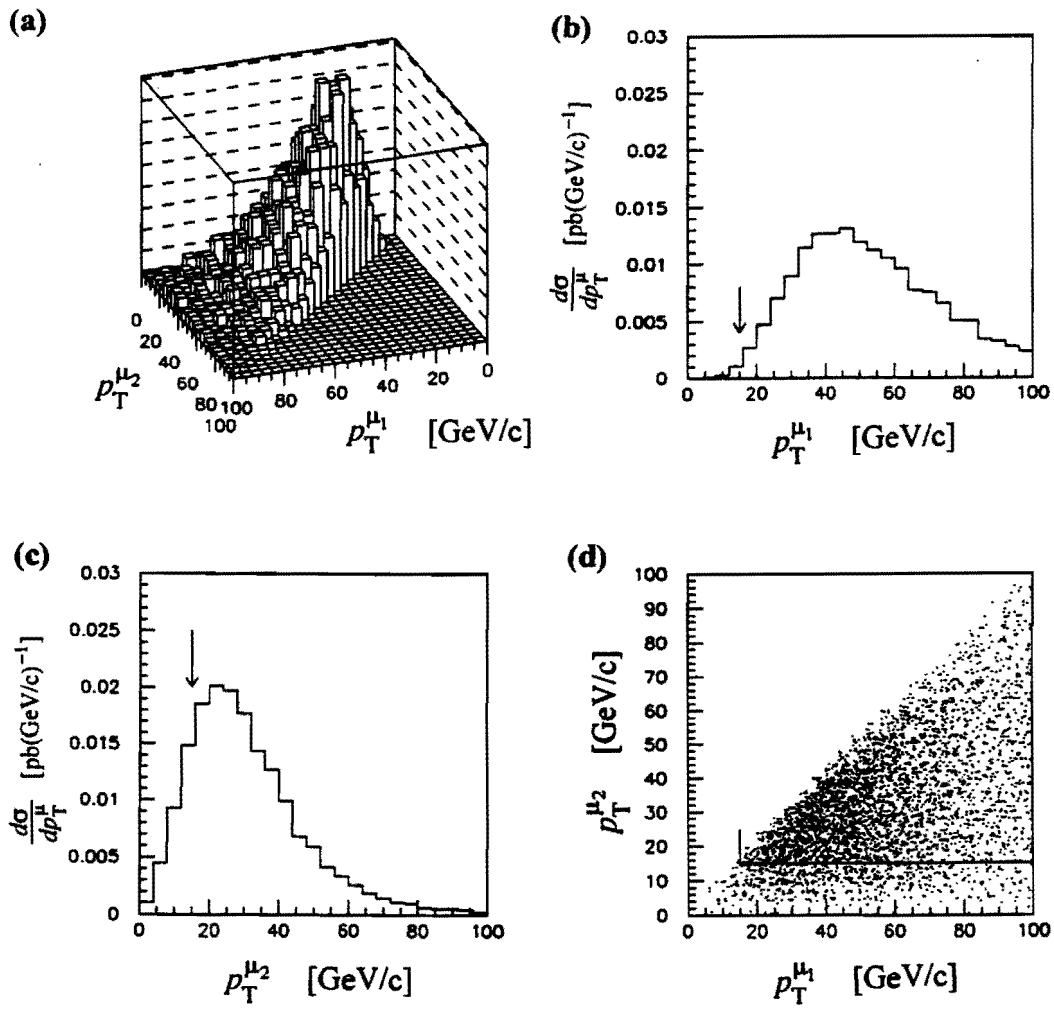

Figure 6.2 ISAJET $t\bar{t} \rightarrow \mu\mu$ (M_t=140 GeV/c^2).

(a) lego plot of $p_T^{\mu_1}$ vs. $p_T^{\mu_2}$ **(b)** $p_T^{\mu_1}$

(c) $p_T^{\mu_2}$ after cut: $p_T^{\mu_1}$ >15 GeV/c **(d)** scatter plot of $p_T^{\mu_1}$ vs. $p_T^{\mu_2}$

Arrows indicate placement of muon p_T cuts.

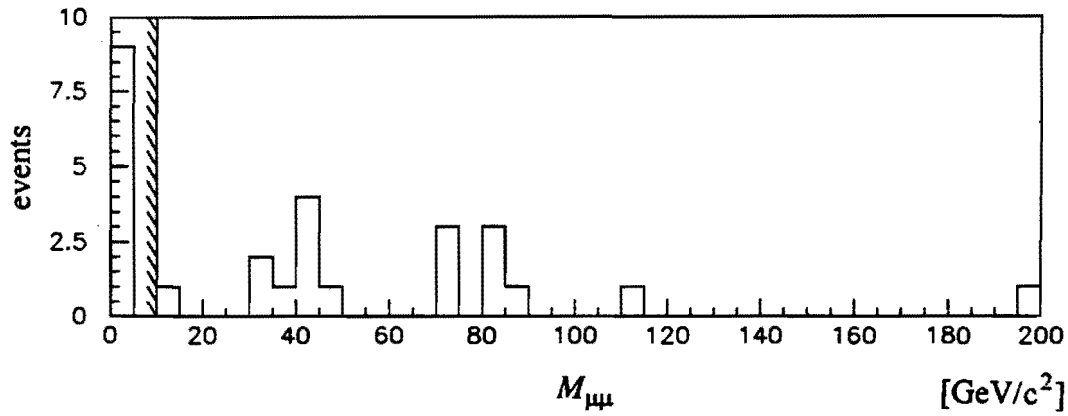

Figure 6.3 Invariant mass of dimuon pair. Data events remaining after initial cuts.

Invariant Mass Cut on Low Mass Pairs

The selection cuts applied up to this point include a number of events that are characterized by a very small opening angle between the muon pair, $\Delta\phi < 10°$ (see Fig. 6.3). These events are consistent with the decay of a high transverse momentum J/Ψ or Ψ' into a muon pair. To exclude these events the invariant mass of the dimuon pair is required to be at least 10 GeV/c^2. This results in a negligible loss in acceptance for the signal because this is an extremely unlikely $t\bar{t} \rightarrow \mu\mu$ topology.

Muon Isolation Requirement

Muons from W decay in a $t\bar{t}$ event are expected to be very isolated, whereas those from a $b\bar{b}$ and $c\bar{c}$ event are typically within or close to a hadronic jet; thus muon isolation is an obvious choice for background rejection. For this analysis isolation is

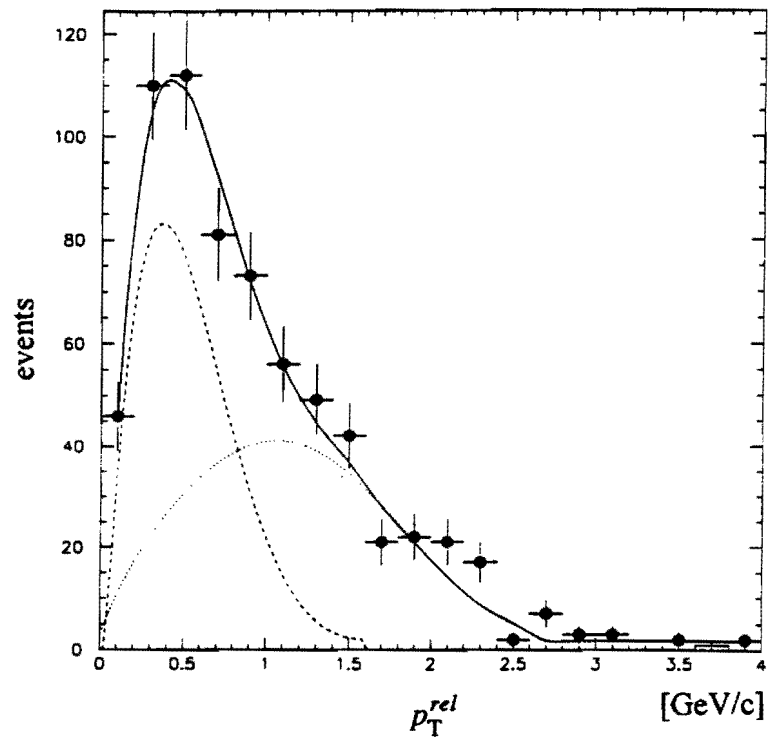

Figure 6.4 p_T^{rel} for single muon plus jet sample (circles with error bars) as compared to full detector Monte Carlo (solid line) which is the sum of the contributions from b quark decays (dotted line) and c quark decays (dashed line) [6.5].

defined in terms of a cut on muon momentum transverse with respect to the axis of the nearest jet (p_T^{rel}) defined as:

$$p_T^{rel} = p^{\mu} \sin \vartheta$$

with

$$\cos \vartheta = \frac{\left(\vec{p}^{\mu} + \vec{E}^{jet}\right) \cdot \vec{p}^{\mu}}{\left|\vec{p}^{\mu} + \vec{E}^{jet}\right| \left|\vec{p}^{\mu}\right|}$$

and $\vec{E}^{jet}$ is defined along the axis of the jet. For this analysis the two highest p_T muons must have p_T^{rel} greater than 5 GeV/c. Figure 6.4 shows p_T^{rel} for a sample of single muon

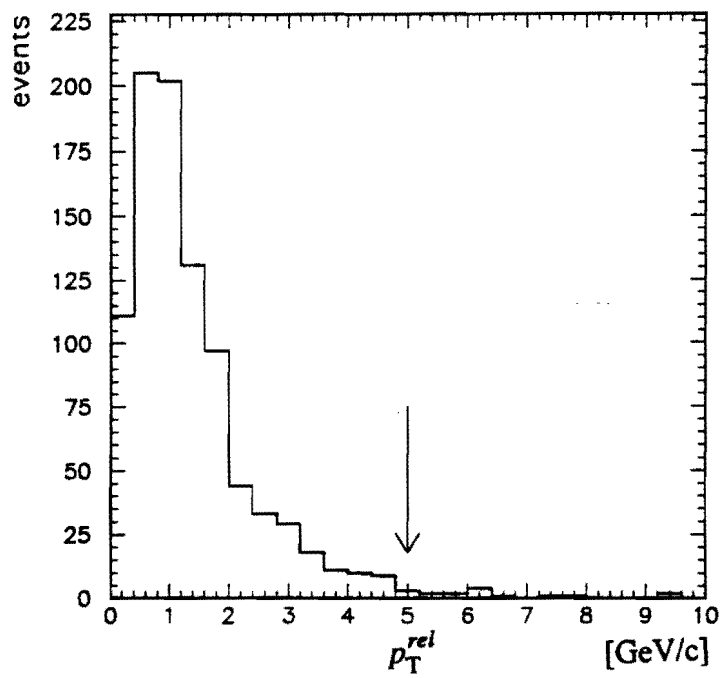

Figure 6.5 p_T^{rel} for single muon ($p_T^{\mu} > 10$ GeV/c) plus jet sample. Arrow indicates cut made in the analysis.

+ jet data for which the events in the tail of the distribution are dominated by b quark decays [6.6]. A cut of 5 GeV/c on p_T^{rel} (Fig. 6.5) gives a rejection of 91.7 ± 1.1 % of the b and c quark decay to muons.

This cut gives strong rejection of $b\bar{b}$ and $c\bar{c}$ background. Furthermore, it rejects background from W+ jets events in which the W decays to a muon and a jet fragments to a non-isolated muon (see Sec. 6.4.2).

Additional Cosmic Ray Rejection

In addition to the cosmic ray rejection included in the muon identification requirements, a further rejection cut is used to reject events in which the two muons are back to back in ϕ and η. Figure 6.6 shows a comparison of $|\Delta\eta^{\mu\mu}|$ and $\Delta\phi^{\mu\mu}$ for cosmic ray data and $t\bar{t} \rightarrow \mu\mu$ Monte Carlo. Events are rejected if $|\Delta\eta^{\mu\mu}| < 0.3$ and $\Delta\phi^{\mu\mu} > 165°$ to protect against 'fake' events in which an in-time cosmic ray is superimposed on a hard scatter.

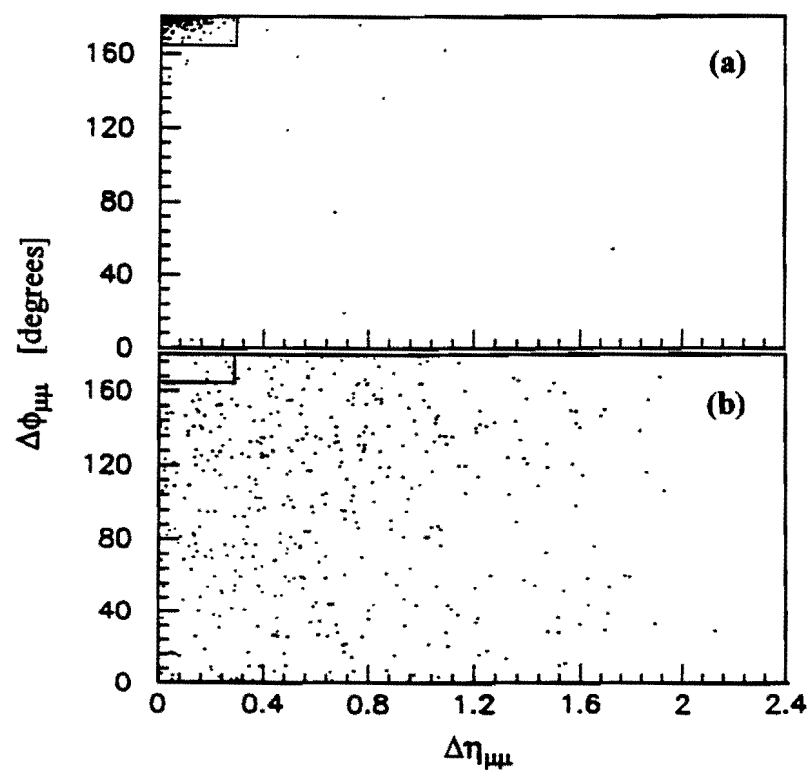

Figure 6.6 $\Delta\phi$ vs. $\Delta\eta$ between muon pair tracks for **(a)** Cosmic ray events and **(b)** $t\bar{t} \rightarrow \mu\mu$ Monte Carlo (M_t=160 GeV/c^2). Solid line indicates excluded region.

Muon Cleanup

Since $Z^0 \rightarrow \mu\mu$ background events contain no real $\not{E}_T$, cuts are applied to reject events where a significant over measurement of the muon momentum gives rise to fallacious $\not{E}_T$. The method employed utilizes the observation that when a muon is mismeasured to be too high the algorithm to calculate the muon corrected $\not{E}_T$ will

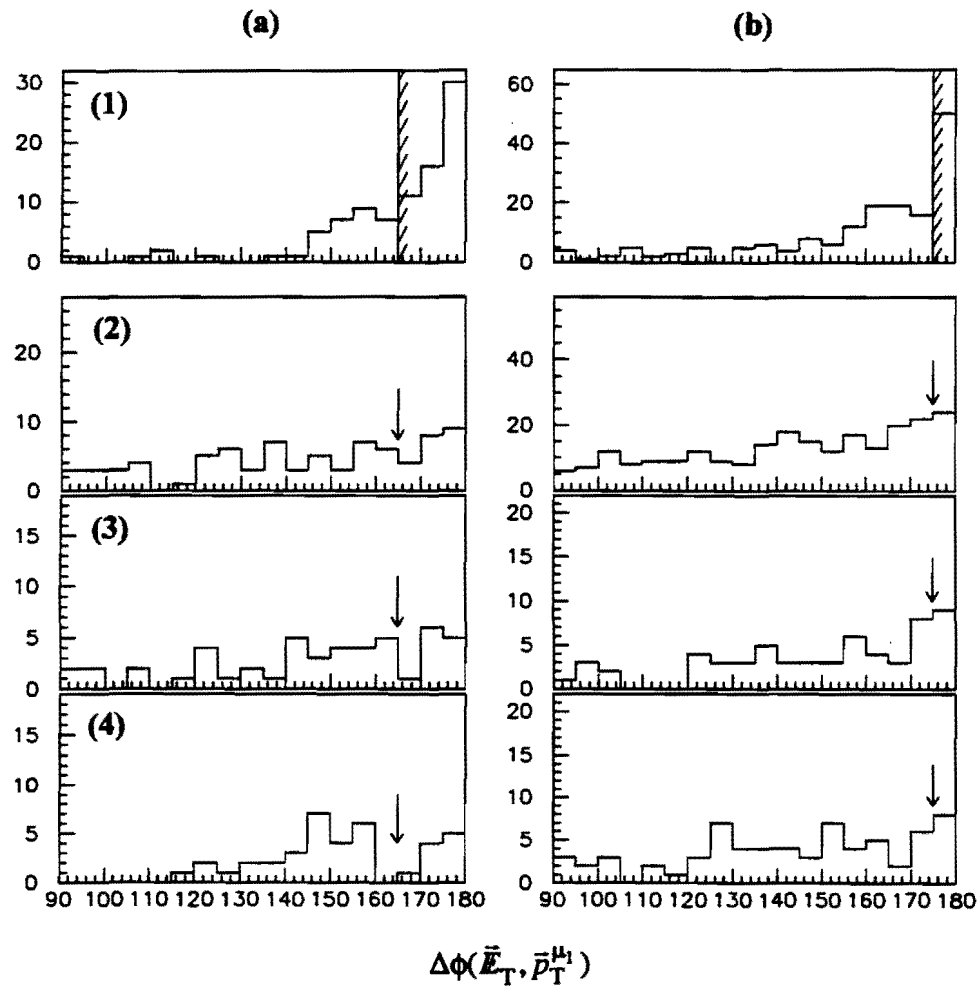

Figure 6.7 Opening angle between leading muon p_T and muon corrected $\not{E}_T$ for: **(a)** two layer tracks and **(b)** three layer tracks, on Monte Carlo samples of: **(1)** $Z^0 \rightarrow \mu\mu$, where hatched lines mark regions excluded and **(2-4)** $t\bar{t} \rightarrow \mu\mu$ (M_t=160, 140, and 120 GeV/c^2), with arrows indicating placement of cut.

balance the transverse energy in the event by adding vectorially this mismeasured amount in the direction opposite to the muon. Thus, in the distribution of the opening angle in $\Delta\phi$ between the leading muon and $\not{E}_T$ vectors this effect leads to a pile up of events at $\Delta\phi \approx 180°$. While the effect is also present for events in which there is real $\not{E}_T$ (*e.g.*, $t\bar{t}$ events) the correlation is much less marked, giving significant discrimination between signal and Z^0 background. Figure 6.7 includes such $\Delta\phi$ distributions for $Z^0 \rightarrow \mu\mu$ and for signal (M_t=120, 140, and 160 GeV/c^2) and also shows that the peak is sharpest for 3-layer muon tracks. To reject against these events the following cut is place on the leading muon:

$$\Delta\phi(\vec{\not{E}}_T, \vec{p}_T^{\mu_1}) < 165° \text{ for 2-layer muon tracks}$$

and

$$\Delta\phi(\vec{\not{E}}_T, \vec{p}_T^{\mu_1}) < 175° \text{ for 3-layer muon tracks.}$$

Missing Transverse Energy Validation

As mentioned, the muon momentum resolution precludes a cut of any efficiency on dimuon invariant mass to eliminate $Z^0 \rightarrow \mu\mu$ events. To further reduce this background a cut is introduced that is relatively insensitive to the momentum resolution and which utilizes the difference in the decay topology between Z^0's and that of $t\bar{t}$ events.

This cut is based on the measurement of the direction in ϕ of the calorimeter missing transverse energy ($\not{E}_T^{cal}$) and its relation to the direction of the vector sum of the two muon p_T vectors (ϕ of $p_T^{\mu\mu}$). The calorimeter sees only minimum ionization energy deposited by the muons (~2 GeV/muon), and thus if there are no neutrinos in the event (as in $Z^0 \rightarrow \mu\mu$) $\not{E}_T^{cal}$ measures the transverse momentum of the dimuon pair (or

Z^0). In the absence of significant mismeasurement of the muon momenta, the direction of the $\not{E}_T^{cal}$ vector is thus aligned with the $p_T^{\mu\mu}$ vector. However, if there are neutrinos with significant p_T produced in the event (as in $t\bar{t}$ decays) then the alignment of these two vectors is coincidental. A cut on the opening angle between the $\not{E}_T^{cal}$ and $p_T^{\mu\mu}$ vectors is relatively insensitive to the resolution on the muon momentum measurement. The directions of the muons are measured with errors insignificant compared to that of

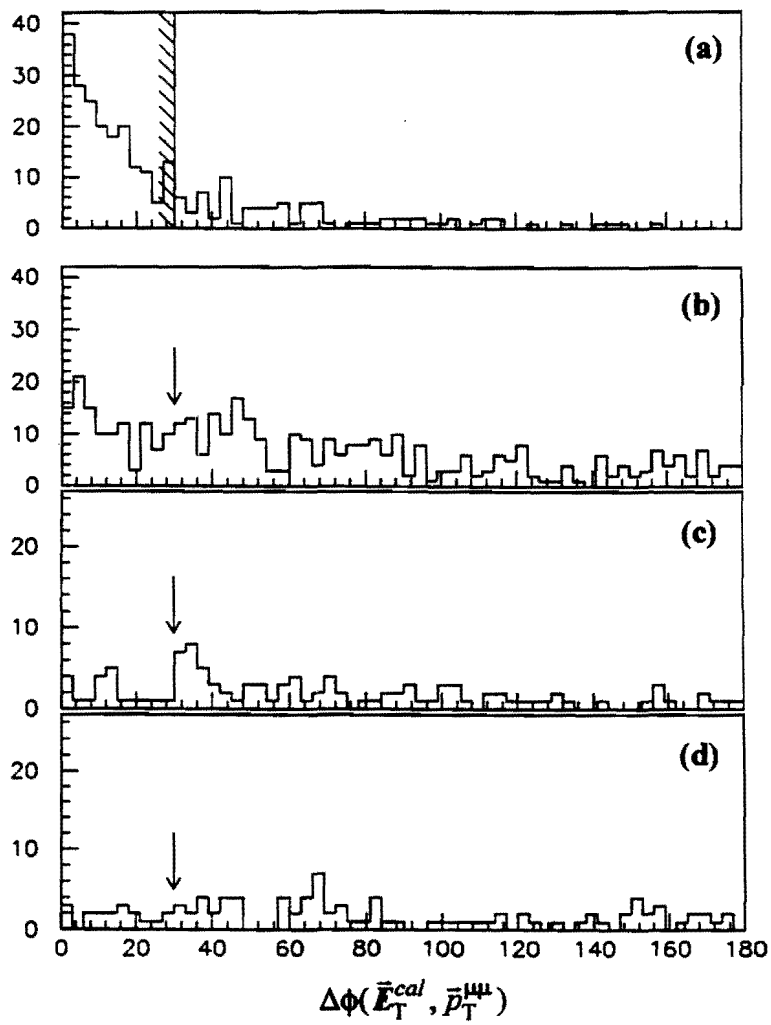

Figure 6.8 Opening angle ($\Delta\phi$) cut on the dimuon p_T vector and the $\not{E}_T^{cal}$ vector for: **(a)** $Z^0 \rightarrow \mu\mu$ Monte Carlo and **(b-d)** $t\bar{t}$ Monte Carlo (M_t=160,140, and 120 GeV/c^2). The cut is placed at 30°, shown by the hatched line for the background and arrows for the signal.

the momentum, and the direction of the $p_T^{\mu\mu}$ will always lie somewhere within the angle $\Delta\phi$ in between the pair of muon p_T vectors. For optimal background rejection the cut is placed at $\Delta\phi(\vec{\not{E}}_T^{cal}, \vec{p}_T^{\mu\mu}) > 30°$ (see Fig. 6.8).

Dimuon Opening Angle – Missing Transverse Energy Correlation Cut

Background events from $Z^0 \to \mu\mu$, $Z^0 \to \tau\tau \to \mu\mu$, and $b\bar{b}$, $c\bar{c} \to \mu\mu$, share the topological characteristic that the muons produced from these processes have a strong tendency to be back to back in ϕ. Further, $Z^0 \to \mu\mu$ and $b\bar{b}$, $c\bar{c} \to \mu\mu$ processes contain very little $\not{E}_T$, and the neutrinos in $Z^0 \to \tau\tau \to \mu\mu$ events tend to cancel, leading to a similar result. However, $t\bar{t} \to \mu\mu$ events have two stiff neutrinos leading to large $\not{E}_T$, and there is no strong correlation between the two muon trajectories. Figure 6.9 show the correlation of these two variables for $Z^0 \to \mu\mu$ background and three values of top mass. To obtain an optimal signal to noise ratio, the requirement is made that for events which $\Delta\phi^{\mu\mu} > 140°$ there must be at least 40 GeV of missing transverse energy. This gives significant rejection against $Z^0 \to \mu\mu$, $Z^0 \to \tau\tau \to \mu\mu$, and residual $b\bar{b}$, $c\bar{c} \to \mu\mu$ events

Two Jet Requirement

A minimum of at least two jets is required in each event, of which the two highest in E_T must be above 15 GeV. These are $\Delta R = 0.7$ fixed cone algorithm jets (Sec 4.3.2) with full energy scale, algorithm and background corrections (Sec. 4.4.2). This cut further suppresses the $Z^0 \to \mu\mu$ background while having little effect on the acceptance for the $t\bar{t} \to \mu\mu$ signal.

No events from data survive these cuts.

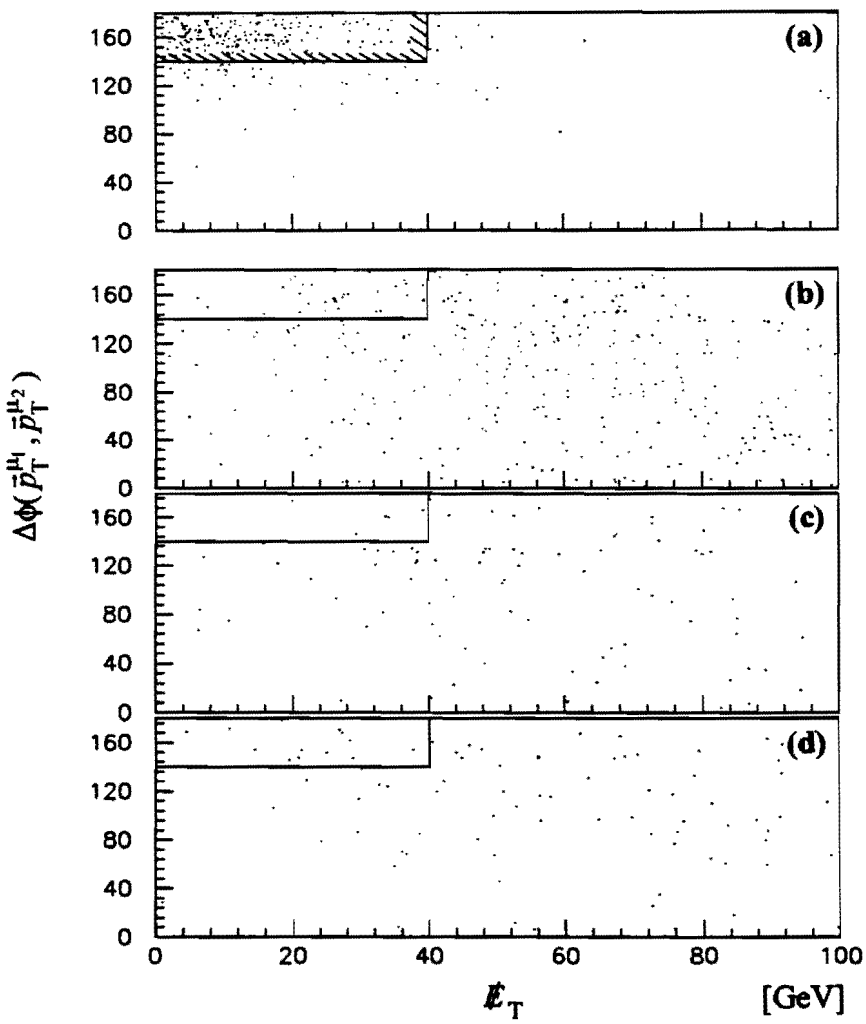

Figure 6.9 Opening angle in ϕ between the p_T vectors of the muon pair vs. the muon corrected missing transverse energy for:

(a) $Z^0 \rightarrow \mu\mu$ Monte Carlo and

(b-d) $t\bar{t}$ Monte Carlo (M_t=160, 140, and 120 GeV/c^2).

M_t (GeV/c^2)	$\sigma \cdot BF_{\mu\mu}$ (pb)	efficiency[total](%)	events in 11.0 pb^{-1}
80	4.14	1.04 ±0.01 ±0.19	0.47 ±0.01 ±0.09 ±0.06
100	1.27	3.67 ±0.02 ±0.66	0.51 ±0.01 ±0.09 ±0.06
120	0.48	8.57 ±0.04 ±1.55	0.45 ±0.01 ±0.08 ±0.05
140	0.21	10.30 ±0.04 ±1.86	0.24 ±0.01 ±0.04 ±0.03
160	0.10	10.51 ±0.01 ±1.89	0.12 ±0.01 ±0.02 ±0.01

Table 6.2 $t\bar{t} \rightarrow \mu\mu$ efficiency (errors: stat,sys) and expected event yield (errors: stat,sys,lum)

6.3 Expected Number of Signal Events

Samples of $t\bar{t} \rightarrow \mu\mu$ Monte Carlo events were generated using the ISAJET Monte Carlo and then processed through full detector and trigger simulation. The resulting event sets for top masses of 80, 100, 120, 140 and 160 GeV were then passed through the same reconstruction and selection code as was used for the data.

Table 6.2 summarizes the resulting values for the selection efficiencies and associated event yields for 11 pb^{-1} of data based on the central NNLO QCD calculations of $t\bar{t}$ cross section by Leanen *et.al.*, [6.7]. The errors quoted are statistical, total systematic and luminosity, of which the 18 % systematic error is dominant. A summary of the principal contributions is given below. The luminosity error is taken as the 12 % uncertainty inherent in the DØ luminosity measurement.

The total systematic error was obtained by calculating the sum in quadrature of the contributions due to the following:

- uncertainties in physics simulation (ISAJET) 10 %
- uncertainties in the modeling of detector response (GEANT) 10 %
- uncertainties in event reconstruction (DØRECO) 10 %
- uncertainties in the modeling of the trigger system 5 %

Each of these is an estimated upper bound derived by varying the different components of the modeling within their errors. More specifically, the 10 % physics simulation uncertainty is derived from comparisons of the ISAJET, PYTHIA, and HERWIG event generators and varying the ISAJET fragmentation functions within reasonable bounds. The 10 % reconstruction uncertainty comes from the combination of the event selection bias [6.4] and studies of the jet reconstruction efficiency [6.8]. Further uncertainties coming from the detailed modeling of the efficiency and resolution of the muon system result in the 10 % GEANT term and the 5 % trigger system uncertainties.

6.4 Background to $t\bar{t} \rightarrow \mu\mu + X$

The processes which mimic the event topology of a $t\bar{t} \rightarrow \mu\mu + X$ event can be divided into two categories; rare processes which have cross sections of the same order as top production and events from the tails of distributions of common processes ($\sigma > 100 \times \sigma_{t\bar{t}}$). Monte Carlo calculations are relied upon for rare processes (such as W boson pair production) which have not yet been experimentally verified and studied. For the more common backgrounds, Monte Carlo calculations are also used but are verified using experimental data. The treatment of the dominant background, $Z^0 \rightarrow \mu\mu$, falls into the latter category and has already been discussed in Section 6.2. The results are summarized below with a discussion of the other background contributions.

6.4.1 Backgrounds Involving Z^0 Decays

$Z^0 \rightarrow \mu\mu$

This is the primary background to the top search in the dimuon channel. Two samples of $Z^0 \rightarrow \mu\mu$ events were generated using the ISAJET, and processed through the full detector simulation and reconstruction program. The first sample is a set of 12,000 events, with the Z^0 forced to decay exclusively to dimuons. The second set of 2000 events was generated similarly with the exception that a Z^0 transverse momentum of at least 15 GeV was required in ISAJET. The latter sample has an enhanced fraction of events with one or more jets (due to the recoil associated with the Z^0's high transverse momentum), and is more representative of the Z^0 decays which mimic the $t\bar{t}$ signal. The set of 12,000 events corresponds to an integrated luminosity of ≈ 61 pb^{-1} and the set of 2000 high p_T Z^0's is equivalent to ≈ 49 pb^{-1}. Table 6.3 shows the cumulative effect of the final analysis cuts on the full 12,000 event $Z^0 \rightarrow \mu\mu$ sample compared to that on the data. As should be expected after the isolation requirement the event yields are in agreement for the rest of the cuts (within the quoted errors).

Applying trigger requirements and full selection cuts leave 4 events remaining out of the total integrated luminosity of 110 pb^{-1}. This corresponds to an expected event yield of

$$0.32 \pm 0.01(\text{stat.}) \pm 0.05(\text{sys.}) \pm 0.04(\text{lum.}) \text{ events}$$

$Z^0 \rightarrow \tau\tau \rightarrow \mu\mu$

To estimate the background from $Z^0 \rightarrow \tau\tau$ with subsequent $\tau \rightarrow \mu$ decays, a set of 2,400 $Z^0 \rightarrow \tau\tau \rightarrow \mu\mu$ events was generated using ISAJET. This was treated in the same way as the $Z^0 \rightarrow \mu\mu$ data set and corresponds to an integrated luminosity of

	Expected $Z^0 \rightarrow \mu\mu$ events in 11.0 pb^{-1}	**Data Events in 11.0 pb^{-1}**
1. Trigger + muon ID + 2nd muon 2 μ's: $p_T^{\mu} > 15$ GeV/c $\lvert\eta^{\mu}\rvert < 1.1$ 1 jet: $E_T^{jet} > 15$ GeV	14.7	29
2. Invariant mass cut $M_{\mu\mu} > 10$ GeV/c^2	14.4	19
3. Muon isolation $p_T^{rel} > 5$ GeV/c	11.5	11
4. Cosmic ray rejection $\Delta\phi(\vec{p}_T^{\mu_1}, \vec{p}_T^{\mu_2}) < 165°$ for $\Delta\eta(\vec{p}^{\mu_1}, \vec{p}^{\mu_2}) < 0.3$	11.5	11
5. Muon cleanup $\Delta\phi(\vec{\not{E}}_T, \vec{p}_T^{\mu_1})$ $< 165°$ for a 2 layer muon track $< 175°$ for a 3 layer muon track	8.2	9
6. $\not{E}_T$ validation $\Delta\phi(\vec{\not{E}}_T^{cal}, \vec{p}_T^{\mu\mu}) > 30°$	3.2	3
7. Dimuon opening angle; $\not{E}_T$ correlation cut $\Delta\phi(\vec{p}_T^{\mu_1}, \vec{p}_T^{\mu_2}) < 140°$ for $\not{E}_T < 40$ GeV	1.7	1
8. Second jet requirement 2nd jet: $E_T^{jet} > 15$ GeV	0.32	0

Table 6.3 Comparison of the cumulative effect of the final analysis cuts on data versus $Z^0 \rightarrow \mu\mu$ full detector simulation Monte Carlo events. Errors on Monte Carlo event yields are 0.04% (stat.), 18% (sys.) and 12% (luminosity).

$\approx 513\ \mathrm{pb}^{-1}$. After trigger requirements and all selection cuts no events survive. Using the binomial one sigma error of 1.148 events for a mean signal of zero, yields an upper limit of:

$$0.000 \pm 0.020(\mathrm{stat.}) \pm 0.004(\mathrm{sys.}) \pm 0.002(\mathrm{lum.})\ \mathrm{events}$$

at a one sigma confidence level.

$Z^0 \to b\bar{b}, c\bar{c} \to \mu\mu$

Since the topology of these events is very similar to that of $Z^0 \to \mu\mu$, an estimate of event yield is obtained by convoluting the rejection factor of p_{T}^{rel} on the non-isolated muons with the estimated event yield from the $Z^0 \to \mu\mu$ background. The isolation requirement $p_{\mathrm{T}}^{rel} > 5$ GeV rejects 91.7 ±1.7(stat.) % of non-isolated muons from b and c quark decays, giving the probability of 8.3 ±1.1 % that a muon will survive this cut. Since both muons in the event must satisfy the p_{T}^{rel} cut the selection efficiency becomes 0.69 ±0.13 %. The combined cross section for Z^0 decays into $b\bar{b}$ and $c\bar{c}$ is approximately 36 pb of which 17.2 % is in the dilepton mode. Combining these effects and an additional loss due to the softer p_{T} spectra of $b \to \mu$ and $c \to \mu$ decays yields an upper limit of

$$0.0004 \pm 0.0001(\mathrm{stat.}) \pm 0.0002(\mathrm{sys.}) \pm 0.0002(\mathrm{lum.})\ \mathrm{events}$$

which is less than 1% of that from $Z^0 \to \mu\mu$.

Drell-Yan Continuum

The processes of dimuon production through the Drell-Yan continuum are topologically very similar to those of $Z^0 \to \mu\mu$ events. ISAJET studies of Drell-Yan $\mu\mu$

and $\tau\tau$ events convoluted with the appropriate muon selection efficiencies from the study of $Z^0 \rightarrow \mu\mu$ gives a combined upper limit of

$$0.0079 \pm 0.0003(\text{stat.}) \pm 0.0014(\text{sys.}) \pm 0.0009(\text{lum.}) \text{ events}$$

for Drell-Yan $\mu\mu$ and Drell-Yan $\tau\tau \rightarrow \mu\mu$ events.

6.4.2 Heavy Quark Decays

The decays of b and c quarks into muons with large transverse momentum typically result in the production of non-isolated muons where the muon track is either in or close to a hadronic jet. As discussed earlier (Sec. 6.2) this analysis takes advantage of this topology and uses a cut on the transverse momentum of the muon with respect to the axis of the nearest hadronic jet (see Fig. 6.10), $p_T^{rel} > 5$ GeV/c, to suppress these events.

The effectiveness of this cut, coupled to the effects of muon identification, trigger selection, and p_T cuts, has been studied using data taken with a multi-jet trigger. This required 5 or more jets (using the $\Delta R = 0.3$ cone algorithm) with $E_T > 10$ GeV at trigger level. A sample of 5380 events ($\int \mathcal{L} dt \approx 540$ nb^{-1}) satisfying this trigger was then subjected to the following cuts:

- ≥ 1 muon with full ID requirements and $|\eta_\mu| < 1.1$
- $p_T^\mu > 15$ GeV
- $p_T^{rel} > 5$ GeV

Four events survive, each containing only one muon. Assuming 5 jets per event, this gives a measure of the probability ($\mathcal{P}_{jet \rightarrow \mu}$) that a jet will contain a muon which satisfies the dimuon analysis cuts. This gives

$$\mathcal{P}_{jet\to\mu} = \frac{4 \text{ muons}}{5\times 5380 \text{ jets}} = 0.00015 \pm 0.00007(\text{stat})$$

Since the sample used did not explicitly exclude events with muons from Z^0 or W boson decay, this gives an upper limit on the rejection of muons from heavy quark decays. Implicit in this calculation is also the contribution from in-flight π and K decays.

W + jets

W boson production becomes a possible background when there are three or more jets in the event and one of the jets contains a muon. For $W\to\mu\nu$ decays of this type, each event will contain; two muons, some jets, and real $\not{E}_T$(from the muon neutrino). This results in a topology close to that of top decay. Discrimination against these events comes primarily from the muon isolation requirement described above.

This has been studied using the event sample used for the top quark search through the decay channel $t\bar{t} \to \mu + jets$ [6.9] which uses the same trigger requirements as this analysis. Consequently the effects of trigger bias are automatically accounted for. Offline these events were selected by requiring the following criteria:

- ≥ 1 muon with full ID requirements and $|\eta_\mu| < 1.1$
- $p_T^\mu > 10$ GeV/c
- ≥ 1 jet with $E_T^{jet} > 10$ GeV using $\Delta R = 0.5$ cone algorithm.

Next the final dimuon selection criteria (see Sec. 6.2) are applied to this event sample, with the following exceptions:

- ≥ 1 muon (instead of ≥ 2 muons) with $p_T^\mu > 15$ GeV/c
- ≥ 3 jets (instead of ≥ 2 jets) with $E_T^{jet} > 15$ GeV
- no requirement involving dimuon quantities ($p_T^{\mu\mu}$, $M_{\mu\mu}$, etc.)

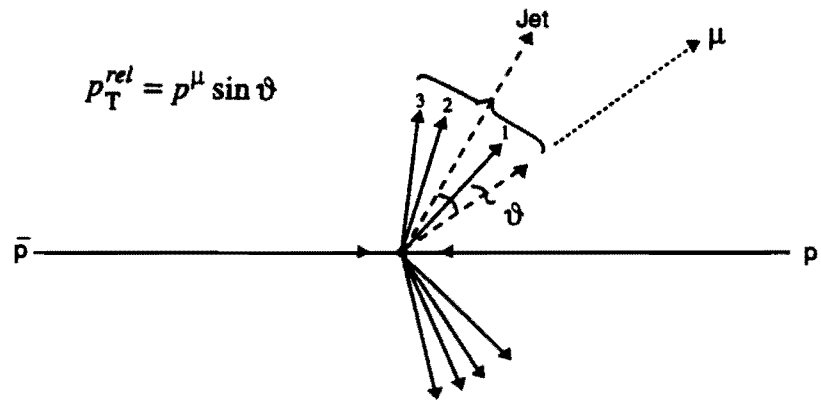

Figure 6.10 Definition of p_T^{rel}.

This leaves 50 events surviving out of 11.0 pb^{-1} of data, for an observed cross section of approximately 4.5 pb.

In this scheme one of the three jets is taken to represent the second muon by convoluting this event yield with the jet-muon probability calculated above. The number of $W+ \geq 3$jet events actually containing a second muon which will pass the dimuon analysis criteria is then estimated by

$$50\,(W \rightarrow \mu + jets \text{ events}) \times 3 \cdot \mathcal{P}_{jet \rightarrow \mu} \cdot$$

$$= 0.023 \pm 0.007(\text{stat.}) \pm 0.004(\text{sys.}) \pm 0.003(\text{lum.}) \text{ events.}$$

Because of the way in which this quantity was evaluated the contributions of multi-jet events with 4 or more jets, where two b or c quarks fragment to muons which pass the dimuon analysis cuts, is included in the above numbers.

6.4.3 Rare Processes

Kinematically the decays of pairs of intermediate vector bosons have a similar signature to $t\bar{t}$ decays. However, since these are very rare processes which have not yet been experimentally measured it is necessary to rely on theoretical predictions for the production cross sections. Here we consider the background due to

- $W^+W^- \rightarrow \mu\mu$ $\qquad \sigma \approx 0.12$ pb
- $Z^0W^\pm \rightarrow \mu\mu$ $\qquad \sigma \approx 0.08$ pb
- $Z^0Z^0 \rightarrow \mu\mu$ $\qquad \sigma \approx 0.05$ pb

and use the cross section calculations of J. Ohnemus *et. al.* [6.10] convoluted with the appropriate muon branching fractions (see Table A.1).

$W^+W^- \rightarrow \mu\mu$

A sample of 500 $W^+W^- \rightarrow \mu\mu$ events was generated using ISAJET and passed through the full detector simulator and event reconstruction. After applying trigger requirements and all analysis cuts, 3 events survive from this sample, which corresponds to approximately 3500 pb^{-1} of data. Imposing the same treatment of systematics used on the signal and Z^0 background gives a predicted event yield of

$$0.007 \pm 0.001(\text{stat.}) \pm 0.001(\text{sys.}) \pm 0.001(\text{lum.}) \text{ events.}$$

$Z^0W^\pm, Z^0Z^0 \rightarrow \mu\mu$

The yields from $Z^0W^\pm$ and Z^0Z^0 production were studied at the parton level using the ISAJET Monte Carlo. By convoluting these with the trigger and event reconstruction efficiencies an upper limit is obtained for these channels of

$$0.009 \pm 0.001(\text{stat.}) \pm 0.002(\text{sys.}) \pm 0.001(\text{lum.}) \text{ events} \qquad (\text{for } Z^0W^\pm \rightarrow \mu\mu)$$

and

$$0.006 \pm 0.001(\text{stat.}) \pm 0.001(\text{sys.}) \pm 0.001(\text{lum.}) \text{ events} \qquad (\text{for } Z^0Z^0 \rightarrow \mu\mu).$$

6.4.4 Instrumental Background

Cosmic Ray Muons

The contamination for cosmic ray muons in the μ+2jet exclusive subset of the data sample used for the top search through $t\bar{t} \rightarrow \mu + jets$ was calculated to be 30.5 ± 10.4 events [6.9]. The top search through $t\bar{t} \rightarrow \mu + jets$ uses the same trigger and initial data sample as that of $t\bar{t} \rightarrow \mu\mu$ such that for this estimate trigger and selection biases are accounted for. Using this estimate, the cosmic ray contamination in the dimuon data set arising from events where there is one real muon and one cosmic ray track overlapping in time with the event is calculated. The cosmic ray rejection cuts (Sec. 6.2) reduce to a negligible level the contribution where one cosmic ray gives both muon tracks in an event. Thus the background is then cosmic ray tracks in coincident with $W \rightarrow \mu\nu$ + 2jet events, or with multi-jet events where b or $c \rightarrow \mu$. Scaling the μ+2jet exclusive cosmic ray event rate to the production rate of these processes gives an estimate for the cosmic contamination in the dimuon data set of

$$0.0005 \pm 0.0001(\text{stat.}) \text{ events.}$$

Punch-Through

The number of interaction lengths provided by the calorimetry and the iron toroids (see Sec. 3.5) makes for a very small level of fake muons from single hadron or jet leakage sources. The muon identification and isolation requirements in the analysis further reduce this such that the contribution to the background from this source is negligible. This contribution of muons from this source is contained in the muon-jet

probability, $P_{jet \to \mu}$, and the event yield is predicted to be a very small fraction of the 0.023 events calculated for $W \to \mu + jets$ and heavy quark decay processes.

6.4.5 Total Background to $t\bar{t} \to \mu\mu$+X

Table 6.4 summarizes the predicted background event yields discussed in the preceding sections. Total background events expected in 11.0 pb^{-1} is estimated by summing the predicted yields from all sources, resulting in

$$0.37 \pm 0.02(\text{stat.}) \pm 0.05(\text{sys.}) \pm 0.04(\text{lum.}) \text{ events.}$$

	Yield for 11.0 pb^{-1}			
	Events	statistical error	systematic error	minosity error
$Z^0 \to \mu\mu$	0.32	±0.01	±0.05	±0.04
$Z^0 \to \tau\tau \to \mu\mu$	0.00	±0.020	±0.004	±0.002
$Z^0 \to b\bar{b} \to \mu\mu$ and $c\bar{c} \to \mu\mu$	0.0004	±0.0001	±0.0002	±0.0002
DY→μμ	0.008	±0.001	±0.001	±0.001
$W^+W^- \to \mu\mu$	0.007	±0.001	±0.001	±0.001
$Z^0W^\pm \to \mu\mu$	0.009	±0.001	±0.002	±0.001
$Z^0Z^0 \to \mu\mu$	0.006	±0.001	±0.001	±0.001
$W + jets \to \mu\mu$ and $QCD \to \mu\mu$	0.023	±0.007	±0.004	±0.003
Total:	0.37	±0.02	±0.05	±0.04

Table 6.4 Backgrounds to $t\bar{t} \to \mu\mu + X$ and associated event yields for 11.0 pb^{-1}.

CHAPTER 7
CONCLUSION

A search for evidence of $t\bar{t}$ production through the subsequent decay to $\mu\mu+X$ has been performed. The analysis assumes Standard Model couplings and branching ratios and is based on data acquired by the DØ detector during its first collider run, resulting in 11.0 ± 1.3 pb^{-1} of integrated luminosity for this search channel. With an expected background of approximately 0.4 events under a selection which optimized signal efficiency and signal to noise ratio, no candidate events were found.

7.1 Top Quark Mass Limit

The number of events remaining after a given set of cuts leads to a cross section for such selected events through the equation

$$\sigma = \frac{N}{BF\,\varepsilon \int \mathcal{L}\,dt}$$

where σ is the total $t\bar{t}$ cross section, N is the number of events detected, BF is the branching fraction to $\mu\mu$, ε is the efficiency and acceptance for detection, and $\int \mathcal{L}\,dt$ is the integrated luminosity. Using efficiencies and acceptances for the detection of $t\bar{t}$ as determined from Monte Carlo studies in conjunction with the observed number of data events; it is possible to set an upper limit on the $t\bar{t}$ production cross section. For a 95 % confidence level the upper limit is defined

$$\sigma_{UL}^{95\%} = \frac{N^{95\%}}{[(\varepsilon - \delta\varepsilon)\cdot BF](\int \mathcal{L}dt - \delta\int \mathcal{L}dt)}$$

where $N^{95\%}$ in the Poisson upper limit at 95% confidence level of the number of events observed, BF is the branching ratio for the particular decay, and $\delta\varepsilon$ and $\delta\int \mathcal{L}dt$ are the uncertainties on the efficiency and integrated luminosity, respectively. In principle, to get a tighter limit one would subtract the number of predicted background events from the observed events. Currently, DØ chooses the more conservative approach of not subtracting background (i.e., the method which is least sensitive to uncertainties in the background Monte Carlo, although giving a lower value for the limit). For zero events observed $N^{95\%}$= 3.00 [7.1], this together with the calculated signal efficiency as a function of top mass (Table 6.2) sets cross section upper limits as a function of top mass.

A lower limit on the mass of the top quark is obtained by comparison of the experimental cross section limit with the theoretical lower limit for $t\bar{t}$ production. Values of M_t for which the experimental limit is less than the theory lower limit is excluded. It is not possible to set a limit on M_t from this channel alone. However, several searches may be combined to place a limit [7.2], as was done in the first DØ published limit on M_t [7.3] giving

$$M_t > 131 \text{ GeV/c}^2 \qquad \text{at 95\% CL}$$

for the combined analysis of the $e\mu$, ee, e + jets, and μ + jets channels. Fig. 7.1 shows the resulting 95 % CL upper limit on the $t\bar{t}$ cross section as a function of M_t compared to predicted cross section lower bound of Laenen *et. al.*, [7.4] from which the limit was derived.

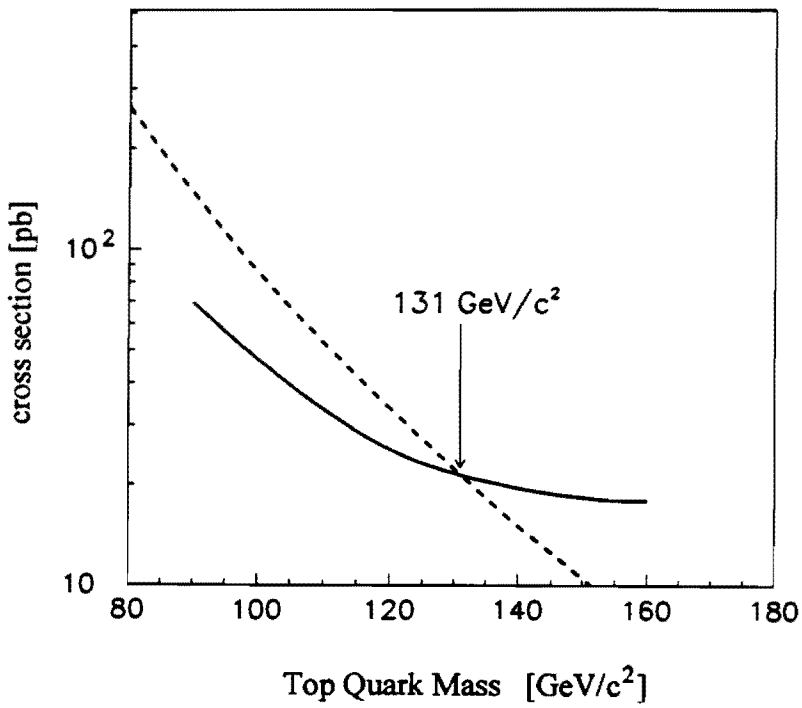

Figure 7.1 The 95% CL limit on $t\bar{t}$ production cross section obtained by DØ using the combined analyses of $e\mu$, ee, e + jets, and μ + jets decay channels. The theory curve (dashed line) is the lower bound from Laenen *et.al.*[7.4].

Due to the small branching fraction and modest acceptance (compared to the $e\mu$ and ee dilepton channels), the dimuon channel adds less than 1 GeV/c^2 to the published limit. However, it demonstrates agreement with the DØ searches in other decay channels, and completes DØ's preliminary search for top in the low background decay channels. Thus the top quark still awaits discovery.

APPENDIX A

Cross Sections and Branching Fractions

Table A.1: Branching Fractions			
Decay process	Combined processes	$(BF)_i$ (%)	Reference
$W \to \mu\nu_\mu$ [(a)]		≈ 11.1 ($\frac{1}{9}$ of total)	[A.1]
	$W^+W^- \to \mu\mu + X$	≈ 1.23 ($\frac{1}{81}$ of total)	
$Z^0 \to ee, \mu\mu, \tau\tau$		≈ 3.34	
$Z^0 \to u\bar{u}, c\bar{c}$		≈ 11.8	[A.1]
$Z^0 \to d\bar{d}, s\bar{s}, b\bar{b}$		≈ 15.2	
$\tau \to \mu\nu_\mu\nu_\tau$		≈ 17.8	[A.2]
	$\tau^+\tau^- \to \mu\mu + X$	≈ 3.1	
$c \to s\mu\nu_\mu$		≈ 8.6	
$b \to c\mu\nu_\mu$		≈ 10.3	
	$c\bar{c} \to \mu\mu + X = [\mathrm{BF}(c \to \mu)]^2$	≈ 0.74	[A.3]
	$b\bar{b} \to \mu\mu + X = [\mathrm{BF}(b \to \mu)]^2$		
	$+2 \cdot [\mathrm{BF}(b \to \mu) \cdot \mathrm{BF}(c \to \mu)]$	≈ 2.83	

(a) Ignoring contribution from $W \to \tau\nu_\tau \to \mu + X$

Table A.2: Total Cross Sections					
Process		σ_{total} for $\sqrt{s}$ = 1.8 TeV			Reference
$p\bar{p} \rightarrow t\bar{t}$	M_t(GeV)	lower(pb)	central(pb)	upper(pb)	
	70	521	680	1102	
	80	265	335	507	
	90	145	180	258	
	100	85.2	103	142	
	110	52.7	61.6	81.4	[A.4]
	120	33.7	38.9	49.7	
	140	15.1	16.9	20.5	
	160	7.41	8.16	9.53	
	180	3.86	4.21	4.78	
	200	2.09	2.26	2.52	
$p\bar{p} \rightarrow Z^o$			6257.5 pb		[A.5]
$p\bar{p} \rightarrow W + X$			20,857 pb		[A.5]
$p\bar{p} \rightarrow W^+W^-$			$\approx$ 10 pb		[A.6]
$p\bar{p} \rightarrow W^{\pm}Z^o$			$\approx$ 2.4 pb		[A.7]
QCD:					
$p\bar{p} \rightarrow b\bar{b}$			$\approx$ 25,000,000 pb		[A.8]
$p\bar{p} \rightarrow c\bar{c}$			$\approx$ 300,000,000 pb		
Drell–Yan:					
$p\bar{p} \rightarrow \gamma \rightarrow \mu\mu$	$M_{\mu\mu} > 25$ GeV		$\approx$ 300 pb		[A.9]
$p\bar{p} \rightarrow \gamma \rightarrow \tau\tau$	$M_{\tau\tau} > 25$ GeV		$\approx$ 300 pb		

Table A.3: Relevant Cross Sections

$\sigma_i = \sigma_{total} \cdot (\mathrm{BF})_i$

Process		$\sigma_{\to\mu\mu}$ for $\sqrt{s}$ = 1.8 TeV		
$p\bar{p} \to t\bar{t}$	M_t(GeV)	lower(pb)	central(pb)	upper(pb)
$\to \mu\mu$	70	6.43	8.40	13.61
	80	3.27	4.14	6.26
	90	1.79	2.22	3.19
	100	1.05	1.27	1.76
	110	0.65	0.76	1.01
	120	0.42	0.48	0.62
	140	0.19	0.21	0.26
	160	0.09	0.10	0.12
	180	0.048	0.052	0.059
	200	0.026	0.028	0.031
QCD:				
$\to \mu\mu\ \sigma_{QCD\to b\bar{b}} \cdot \mathrm{BF}(bb \to \mu\mu) +$ $\sigma_{QCD\to c\bar{c}} \cdot \mathrm{BF}(c\bar{c} \to \mu\mu)$			$\approx$ 930,000 pb	
$p\bar{p} \to Z^0$				
$\to \mu\mu\ \sigma_{Z^0} \cdot \mathrm{BF}(Z^0 \to \mu\mu)$			$\approx$209 pb	
$\to \tau\tau \to \mu\mu\ \sigma_{Z^0} \cdot \mathrm{BF}(Z^0 \to \tau\bar{\tau}) \cdot \mathrm{BF}(\tau\bar{\tau} \to \mu\mu)$			$\approx$6.5 pb	
$\to b\bar{b} \to \mu\mu\ \sigma_{Z^0} \cdot \mathrm{BF}(Z^0 \to b\bar{b}) \cdot \mathrm{BF}(b\bar{b} \to \mu\mu)$			$\approx$26.9 pb	
$\to c\bar{c} \to \mu\mu\ \sigma_{Z^0} \cdot \mathrm{BF}(Z^0 \to c\bar{c}) \cdot \mathrm{BF}(c\bar{c} \to \mu\mu)$			$\approx$5.5 pb	
$p\bar{p} \to W + n\ jets$	$n \geq 0$	1956.00 ±7.27 ±391.00 pb		
$W \to \mu$	$n \geq 1$	566.80 ±3.33 ±113.00 pb		
	$n \geq 2$	168.60 ±1.33 ± 67.44 pb		[A.10]
	$n \geq 3$	45.44 ±0.63 ± 27.26 pb		
Drell-Yan:				
$\to \mu\mu\ \sigma_{\gamma\to\mu\mu}$			$\approx$300 pb	
$\to \tau\tau \to \mu\mu\ \sigma_{\gamma\to\tau\bar{\tau}} \cdot \mathrm{BF}(\tau\bar{\tau} \to \mu\mu)$			$\approx$9.3 pb	
$p\bar{p} \to W^+W^-$				
$\to \mu\mu\ \sigma_{W^+W^-} \cdot [\mathrm{BF}(W \to \mu)]^2$			$\approx$0.12 pb	
$p\bar{p} \to W^\pm Z^0$				
$\to \mu\mu\ \sigma_{WZ^0} \cdot \mathrm{BF}(Z^0 \to \mu\mu)$			$\approx$0.08 pb	

References

[1.1] M.Z. Akrawy *et. al.*, *Phys. Lett.* **B235** 379 (1990).
D. Decamp *et. al.*, *Phys. Lett.* **B235** 399 (1990).
B. Adeva *et. al.*, *Phys. Lett.* **B237** 136 (1990).
D. Aarnio *et. al.*, *Phys. Lett.* **B241** 428 (1990).
O. Adriani *et. al.*, *Phys. Lett.* **B292** 463 (1992).

[1.2] Particle Data Group, "Particle Properties Data Booklet" from *Phys. Rev.* **D45** *Part II,* p.12 (1992).

[1.3] D. Buskulic *et. al.*, *Phys. Lett.* **B313** 299 (1993).

[1.4] S.W. Herb *et. al.*, *Phys. Rev. Lett.* **39** 252 (1977).

[1.5] S. Abachi *et. al.*, *Phys. Rev. Lett.* **72** 2138 (1994).

[1.6] M. Shapiro and J.L. Siegrist, "Hadron Collider Physics" in Ann. Rev. Nuc. Sci. Vol. 41, Annual Reviews Inc., Palo Alto, p. 125 (1991).

[1.7] N. Graf, *Production of W and Z Bosons at DØ,* Proceedings of the 9th Topical Workshop in $\bar{p}p$ Collider Physics, Tsukuba, Japan 1993.

[2.1] G.L. Kane, Top Quark Physics, Univ. of Michigan preprint UM-TH-91-32 1991.

[2.2] S.L. Glashow, J. Illiopoulos, and L. Maiani, *Phys. Rev.* **D2** 1285 (1970).

[2.3] G.L. Kane, and M. Peskin, *Nucl. Phys.* **B195** 29 (1982).

[2.4] C. Albajar *et. al.*, *Phys. Lett.* **262B** 163 (1991).

[2.5] C. Albajar *et. al.*, *Phys. Lett.* **186B** 247 (1987).

[2.6] H. Albrecht *et. al.*, *Phys. Lett.* **192B** 245 (1987).

[2.7] M. Swartz, *High Energy Tests of the Electroweak Standard Model,* Proceedings of the XVI International Symposium on Lepton-Photon Interactions, Cornell University, 1993.

[2.8] W. Marciano and A. Sirlin, *Phys. Rev.* **D29** 945 (1984).

[2.9] The LEP Collaborations ALEPH, DELPHI, L3, OPAL, and The LEP Electroweak Working Group, *Updated Parameters of the Z^0 Resonance from Combined Preliminary Data of the LEP Experiments*, CERN/PPE/93–157, (unpublished) 1993.

[2.10] P. Nason, S. Dawson, and R.K. Ellis, *Nucl. Phys.* **B303** 607 (1988); P. Nason, S. Dawson, and R.K. Ellis, *Nucl. Phys.* **B327** 49 (1989); Errata **B335** 260 (1990).

[2.11] G. Altarelli, M.Diemor, G. Martinelli and P. Nason, *Nucl. Phys.* **B308** 724 (1988).

[2.12] M. Diemor, F. Ferroni, E. Longo and G. Martinelli, *Z. Phys.* **C39** 21 (1988).

[2.13] E. Laenen, J. Smith and W.L. van Neerven, *Phys. Lett.* **B321** 254 (1994); E. Laenen, J. Smith and W.L. van Neerven, *Nucl. Phys.* **B369** 543 (1992).

[2.14] A.D. Martin, R.G. Roberts, W.J. Stirling, *Phys. Lett.* **B306** 145 (1993).

[2.15] R.K. Ellis, *Proceedings of the Seventeenth SLAC Summer Institute on Particle Physics* pp.45–67 (1989).

[2.16] C. Peterson, D. Schlatter, L. Schmitt and P.Z. Zerwas, *Phys. Rev.* **D27** 105 (1983).

[2.17] V. Barger and R. Phillips, *Collider Physics*, Addison-Wesley Publishing Company, New York, pp.177–180 (1987).

[2.18] R. Hollebeek, *Proceeds of the Twentieth SLAC Summer Institute on Partical Physics*, pp.253–290 (1992).

[3.1] *Design Report, Tevatron 1 Project*, Fermi National Accelerator Laboratory internal note, (unpublished) 1984.

[3.2] D.A. Edwards, and M.J. Syphers, *An Introduction to the Physics of High Energy Accelerators,* John Wiley and Sons, New York, 1993.

[3.3] M.D. Church and J.P.Marriner, *Annu. Rev. Nucl. Part. Sci.* **43** 253 (1993).

[3.4] S. Abachi *et. al., Nucl. Inst. Meth.* **A338** 185 (1994).

[3.5] A. R. Clark *et. al., Nucl. Instr. and Meth.* **A279** 243 (1989).

[3.6] A. R. Clark *et. al., Nucl. Instr. and Meth.* **A315** 193 (1992).

[3.7] J.-F. Detoeuf *et. al., Nucl. Instr. and Meth.* **A279** 310 (1989).

[3.8] F. Feinstein, *Etude d'un Detecteura Rayonnement de Transistion pour l'Experience DØ au FNAL,* Ph.D thesis, A l'University de Paris-Sud, Centre d'Orsay, December 1987 (unpublished).

[3.9] A. R. Clark, *et. al., Nucl. Instr. and Meth.* **A279** 243 (1989).

[3.10] S. Abachi *et. al., Nucl. Instr. and Meth.* **A324** 53 (1993).

[3.11] S. Aronson, *et. al., Nucl. Instr. and Meth.* **A269** 492 (1988).

[3.12] S.J. Wimpenny, *et. al., Nucl. Instr. and Meth.* **A279** 107 (1989).

[3.13] R. Hirosky, *The Response of the D-Zero Central Calorimeter to Electrons and Pions from 2 through 150 GeV/c*, DØ internal note # 1499 March 1993 (unpublished).

[3.14] C. Brown, *et. al., Nucl. Instr. and Meth.* **A279** 331 (1989).

[3.15] M. Fortner, *et. al., IEEE Trans. Nucl. Sci.* NS-**38** 480 (1991).

[3.16] J. Bantly, *et. al., The Level 0 Trigger for the DØ Detector*, DØ internal note #1996 November 1993 (summitted to *IEEE Trans. Nucl. Sci.*).

[3.17] K. Bazizi, *Level 1.0 and Level 1.5 Muon trigger Efficiencies for Single Tracks*, DØ internal note # 1618 February 1993 (unpublished).

[4.1] J.M. Butler, *Main Ring Deadtime*, DØ internal note # 1682, February 1993 (unpublished).

[4.2] S. Abachi *et. al.,* Nucl. Inst. Meth. **A338** 185 (1994).

[4.3] R. Astur, private communication.

[4.4] C. Gerber and P. Quintas, *Muon Momentum Resolution from DØRECO V10*, DØ internal note # 1985, November 1993 (unpublished).

[4.5] M. Paterno, *A Study of the DØ Calorimeter $\not{E}_T$ Resolution Using Low E_T Jet Triggers*, DØ internal note #1782, July 1993 (unpublished).

[4.6] F. Abe *et. al.*, (the CDF collaboration), *Dijet Angular Distributions in $p\bar{p}$ collisions at $\sqrt{s}$ = 1.8 TeV*, FERMILAB-Pub-92/182-E, 1992 (submitted to Phys. Rev. Lett.).

[4.8] U. Heintz, *"Standard" EM Energy Scale Correction for RECO V10,* DØ internal note # 1758, June 1993 (unpublished).

[5.1] V. Barger and R. Phillips, Collider Physics, Addison–Wesley Publishing Company pp.397–427 (1987).

[5.2] F.E. Paige and S.D. Protopopescu, *ISAJET 6.49: A Monte Carlo Event Generator for P-P and Pbar-P Reactions*, Fermilab Computing Division, PM0059 (August 1992).

[5.3] H.U. Bengtsson and T. Sjöstrand, *PYTHIA, The Lund Monte Carlo for Hadronic Processes*, Proceedings of Snowmass '86, p.311 (1986).

[5.4] G. Marchesini *et. al.*, *HERWIG: Version 5.1*, CAVENDISH-HEP-91-26, May 1991 (unpublished).

[5.5] S. Protopopescu, *Event simulation for hadron colliders*, University of DØ proceedings, August 8, 1991 (unpublished).

[5.6] G. Altarelli and G. Parisi, *Nucl. Phys.* **B126** 298 (1977).

[5.7] V. Barger and R. Phillips, *Collider Physics*, Addison-Wesley Publishing Company pp.169–192 (1987).

[5.8] R.D. Field and R.P. Feynman, *Nucl. Phys.* **B136** 1 (1978).

[5.9] N. Ellis and A. Kernan, *Physics Reports*, **195**(2&3) pp. 44–46 (1990).

[5.10] R. Brun *et. al.*, GEANT 3.15 program manual, CERN.

[5.11] S. Abachi *et. al.*, Nucl. Inst. Meth. **A338** 185 (1994).

[5.12] J. Womersley, *The DØ Monte Carlo*, DØ internal note # 1520, August 1992 (unpublished).

[5.13] H.T. Diehl, *MU-SMEAR package Documentation,* DØ internal note (in preparation).

[5.14] J.T. Linnmann, *Triggering the DØ Experiment*, in the proceedings of the 7th Meeting of the APS Division of Particles and Fields, Vol. 2, p.1642 (1992).

[6.1] J.H. Cochran, *Search for Truth in the eμ Channel at DØ*, Ph.D. Thesis, State University of New York at Stony Brook, December 1993 (unpublished).

[6.2] S. Abachi *et. al.*, *Phys. Rev. Lett.* **72** 2138 (1994).

[6.3] F. Abe *et. al.*, (CDF Collaboration), *Phys. Rev.* **D45** 3921 (1992).

[6.4] S.J. Wimpenny, private communication.

[6.5] A.K.A. Maciel, private communication.

[6.6] T. Huehn, private communication.

[6.7] E. Laenen, J. Smith and W.L. van Neerven, *Phys. Lett.* **B321** 254 (1994).

[6.8] J. Blazey, private communication.

[6.9] W.J. Thompson, *Search for the Top Quark in the Muon + Jets Channel* at *DØ*, Ph.D Thesis, State University of New York at Stony Brook, February 1994 (unpublished).

[6.10] J. Ohnemus, *Phys. Rev.* **D44** 1403 (1991);
J. Ohnemus, *Phys. Rev.* **D44** 3477 (1991).

[7.1] Particle Data Group, "Particle Properties Data Booklet" from *Phys. Rev.* **D45** *Part II,* p.158 (1992).

[7.2] R. Partrige, *Top Limit Calculation*, DØ Internal note # 1782, 1993 (unpublished).

[7.3] S. Abachi *et. al.*, *Phys. Rev. Lett.* **72** 2138 (1994).

[7.4] E. Laenen, J. Smith and W.L. van Neerven, *Phys. Lett.* **B321** 254 (1994).

[A.1] R.K. Ellis and W.J. Sterling, *QCD and Collider Physics*, Fermilab-Pub-Conf-90/164-T, pp.84–85, 1991 (unpublished).

[A.2] Particle Data Group, "Particle Properties Data Booklet" from *Phys. Rev.* **D45** *Part II,* p.12 (1992).

[A.3] B. Adeva *et. al.*, *Phys. Lett.* **B261** 177 (1991).

[A.4] E. Laenen, J. Smith, and W.L. van Neerven, *Phys. Lett.* **B321** 254 (1994).

[A.5] F. Abe *et. al.*, (CDF Collaboration), *Phys. Rev.* **D44** 30 (1991).

[A.6] J. Ohnemus, *Phys. Rev.* **D44** 1403 (1991).

[A.7] J. Ohnemus, *Phys. Rev.* **D44** 3477 (1991).

[A.8] V. Barger and R. Phillips, *Collider Physics*, Addison-Wesley Publishing Company, New York, p.380 (1987).

[A.9] F. Abe *et. al.*, (CDF Collaboration), *Phys. Rev. Lett.* **67** 2418 (1991).

[A.10] J. Yu, private communication.